Journal of Geophysical Research: Oceans

Mechanisms of surface wave energy dissipation over a high-concentration sediment suspension

Peter Traykovski[1], John Trowbridge[1], and Gail Kineke[2]

[1]Applied Ocean Physics and Engineering Department, Woods Hole Oceanographic Institution, Woods Hole, Massachusetts, USA, [2]Department of Earth and Environmental Sciences, Boston College, Chestnut Hill, Massachusetts, USA

Abstract Field observations from the spring of 2008 on the Louisiana shelf were used to elucidate the mechanisms of wave energy dissipation over a muddy seafloor. After a period of high discharge from the Atchafalaya River, acoustic measurements showed the presence of 20 cm thick mobile fluid-mud layers during and after wave events. While total wave energy dissipation (D) was greatest during the high energy periods, these periods had relatively low normalized attenuation rates (κ = Dissipation/Energy Flux). During declining wave-energy conditions, as the fluid-mud layer settled, the attenuation process became more efficient with high κ and low D. The transition from high D and low κ to high κ and low D was caused by a transition from turbulent to laminar flow in the fluid-mud layer as measured by a Pulse-coherent Doppler profiler. Measurements of the oscillatory boundary layer velocity profile in the fluid-mud layer during laminar flow reveal a very thick wave boundary layer with curvature filling the entire fluid-mud layer, suggesting a kinematic viscosity 2–3 orders of magnitude greater than that of clear water. This high viscosity is also consistent with a high wave-attenuation rates measured by across-shelf energy flux differences. The transition to turbulence was forced by instabilities on the lutocline, with wavelengths consistent with the dispersion relation for this two-layer system. The measurements also provide new insight into the dynamics of wave-supported turbidity flows during the transition from a laminar to turbulent fluid-mud layer.

1. Introduction

Although there have been numerous observations of rapid attenuation of ocean surface gravity wave energy propagating over muddy seafloors in numerous locations including India [*Mathew and Baba*, 1995], Louisiana [*Higgins*, 2002; *Kemp and Wells*, 1987; *Sheremet and Stone*, 2003], South Korea [*Wells*, 1983], and Guyana-Surinam [*Wells and Kemp*, 1986], the mechanisms at the mud-water interface that cause the dissipation have not been directly measured in a field environment. Theoretical analysis has suggested several mechanisms that span a large range of mud rheological characteristics. These range from considering the mud to be a viscous fluid [*Dalrymple and Liu*, 1978; *Gade*, 1958; *Jiang and Mehta*, 1993; *Ng*, 2000] to various combinations of viscous, elastic, plastic [*Macpherson*, 1980; *Mei and Liu*, 1987], and porous media [*Liu*, 1973] with coulomb damping [*Lee et al.*, 2002]. In addition, a number of theories involving nonlinear interactions have been proposed [*Foda*, 1989; *Hill and Foda*, 1998, 1999; *Kaihatu et al.*, 2007; *Yang and Hwung*, 2012]. Recent numerical studies have focused on turbulent and transitional fluid-mud layers [*Hsu et al.*, 2009; *Ozdemir et al.*, 2011]. Due to the complexity of selecting the media properties of the combined process models and combined with the reasoning that a mud layer liquefies quickly at the beginning of storms, the viscous Newtonian fluid models have been compared most extensively to laboratory data [*Winterwerp et al.*, 2007]. These models typically describe the mud-water system using two layers, with a water layer overlying a fluid-mud layer, where the fluid-mud layer thickness, density, and viscosity are specified. Because the fluid-mud viscosity is often orders of magnitude greater than that of clear water, the viscosity in the water layer is often ignored, and the flow is assumed to be laminar in the fluid-mud layer. Thus, viscous dissipation in the fluid-mud layer is the only process included in these approaches. For the purposes of this manuscript, the definition of fluid-mud described by *Ross and Mehta* [1989] is used. Fluid-mud layers are near-bed fine sediment suspensions with strong concentration gradients, referred to as lutoclines, and concentrations above 10 kg/m³.

Studies based on field measurements have either focused on the properties of the surface waves and have indicated increased dissipation when mud is present on the seafloor [*Higgins*, 2002; *Tubman and Suhayda*,

1976; *Wells and Kemp*, 1986], or some have combined analysis of mud samples in the laboratory with the in situ observations [*Jiang and Mehta*, 1993, 1995; *Winterwerp et al.*, 2012]. In recent studies, considerable attention has been paid to the frequency dependence of the dissipation. For instance, *Sheremet and Stone* [2003] have noted the attenuation of both long wavelength and short wavelength waves after periods of strong resuspension. *Elgar and Raubenheimer* [2008] concluded that nonlinear energy transfer to infragravity band and depth-dependent dissipation in the infragravity band was the dominant mechanism. Several studies [*Rogers and Holland*, 2009; *Sheremet et al.*, 2011; *Siadatmousavi et al.*, 2012] infer properties of the mud layer from surface wave-attenuation measurements, but without direct measurements and identification of the mechanisms of dissipation in the mud layers, these inverse approaches contain uncertainty because the forward model may not include the correct processes. A recent series of papers, based on observations at a location near the study site for the measurements described in this paper on Atchafalaya Louisiana Shelf, document the presence of fluid mud and increased attenuation [*Jaramillo et al.*, 2009; *Safak et al.*, 2010; *Sheremet et al.*, 2011]. *Jaramillo et al.* [2009] show one of the few field measurements of velocity structure within a fluid-mud wave boundary layer, and used the difference between the elevation of the acoustic backscatter peak from the top of the lutocline and the level of no motion to estimate the fluid-mud layer thickness. *Safak et al.* [2010] examined turbulence damping due to high sediment concentrations, but the concentrations in that study were less than 5 kg/m^3 unlike the much higher densities present in *Jaramillo et al.* [2009] and *Sheremet et al.* [2011]. On the Amazon continental shelf, *Kineke et al.* [1996] documented the presence of fluid mud in 1–2 m thick tidal boundary layers with concentration in excess of 100 kg/m^3, and *Vinzon and Mehta* [2000] suggest that turbulence was reduced by the high viscosity of the fluid mud based on velocity profile structure. *Trowbridge and Kineke* [1994] used velocity and sediment concentration profiles from the Amazon shelf to examine the role of fluid-mud-induced density stratification in damping the fluid-mud layer turbulence in this environment. However, these velocity profiles did not have sufficient vertical and temporal resolution to resolve turbulent fluctuations.

In order to provide insights on how the various proposed theories relate to observed surface wave attenuation on a muddy continental shelf, this paper describes a set of field measurements conducted to measure both wave attenuation and the near-bed processes that cause the dissipation. Wave attenuation was measured with a cross-shelf array of wave sensors, and instrumentation capable of resolving wave boundary layer velocity profiles and turbulent fluctuations was deployed in the center of the array.

The paper is organized as follows: section 2 presents theoretical background with basic definitions and equations describing an oscillatory flow in a two-layer system consisting of dense viscous mud overlain by nonviscous water. Both complete solutions are based on the work of *Kranenburg et al.* [2011], and approximate solutions for an infinitely thick upper layer are presented. Several examples of velocity profiles and dissipation calculations are presented to illustrate the physics of the boundary layer viscous scaling in controlling the attenuation rates. These equations are also used in an inverse manner to estimate the mud viscosity based on measured velocity profiles in section 4.5. Section 3 presents the field measurement techniques, including descriptions of the various sensors and data processing techniques. This includes descriptions of seafloor frame-based acoustical and optical backscatter measurements, surface wave energy flux measurements, and pulse-coherent Doppler boundary layer profiles. Section 4 presents results from the field measurements. Introductory sections 4.1–4.4 describe the measurement site, the regional wind forcing and surface wave response, and measurements of wave energy flux attenuation. Section 4.5 presents a detailed discussion of the flow in the fluid-mud layer and energy-dissipation mechanisms. This section contains three examples of the measurements during laminar, transitional, and turbulent flow conditions to illustrate the different mechanisms during these regimes. Section 4.6 examines wave-supported downslope turbidity flows in the context of the transition from turbulent to laminar flow in the fluid-mud layer. Section 4.7 examines the formation and generation mechanisms of internal waves on the lutocline. The instabilities resulting from these waves are important in controlling the transition from laminar to turbulent flow in the fluid-mud layer, which subsequently controls the attenuation rate. Conclusions are presented in section 5.

2. Theoretical Background

In order to investigate mechanisms of wave attenuation, the primary quantities of interest are wave energy flux divergence (F_x) and the spatial attenuation rate

$$\kappa = F_x / F, \tag{1}$$

where wave energy flux is defined as $F = E\, C_g$, with E as wave energy density and C_g as group velocity. The sea surface elevation can be written as

$$a_1 = \mathrm{Re}\left\{ \tilde{a}_1 e^{-(\mathrm{Im}(k) + i\mathrm{Re}(k))x + i\omega t} \right\}, \tag{2}$$

where the imaginary (Im) part of the complex wave number (k) describes the wave amplitude attenuation from an initial amplitude $\tilde{a}_1$ and the real (Re) part describes the harmonic oscillation. Since $E = \rho g \tilde{a}^2_{\,1}/2$, the energy flux divergence is $F_x = -2\,\mathrm{Im}(k)\,F$ (throughout the paper the $\sim$ diacritical mark indicates complex amplitudes of oscillatory variables, the subscript 1 refers to the air-water interface, the subscript 0 refers to the fluid mud-water interface, the subscript w refers to the overlying water layer, and the subscript m refers to the fluid-mud layer). In the absence of additional source or sink terms such as wind input or white capping, the wave energy flux divergence is equal to the depth integrated dissipation $D = \rho \int \varepsilon dz$, where ε is the local energy dissipation and can be partitioned in turbulent dissipation (ε_t) and laminar flow viscous dissipation (ε_v), based on the temporal and spatial scales of the dissipation processes. In a similar manner, the total viscosity (v) can be partitioned into a turbulent eddy viscosity (v_t) and fluid-mud viscosity (v_m). The variable v_m includes both molecular viscosity and sediment-induced rheological viscosity and can be much greater than the molecular viscosity of clear water due to the presence of viscous fluid mud. In the turbulent case, the energy cascades from large eddies to smaller eddies where viscous dissipation takes place. In the laminar case, direct viscous dissipation acts on the velocity gradients in the wave boundary layer. A wave energy-dissipation factor ($f_{e,Fx}$) relating the dissipation to wave orbital velocity amplitude just above the fluid-mud layer ($\tilde{u}_{0w}$) is defined by

$$F_x = \frac{2}{3\pi} \rho_w f_{e,Fx} \tilde{u}_{0w}^3. \tag{3}$$

The subscript Fx on f_e indicates this dissipation factor is calculated based on wave energy flux divergence as opposed to local boundary layer estimates of dissipation.

2.1. Two-Layer Laminar Viscous Flow Solutions

In order to examine the relative roles of the internal and external modes in dissipating wave energy, the imaginary part of the wave number can be calculated from the dispersion relation for the two-layer system. The equation of horizontal motion for the fluid-mud layer is

$$\frac{\partial}{\partial t}\left(u_m - \frac{\rho_w}{\rho_m} u_{0w} \right) = \frac{\partial}{\partial z}\left(v \frac{\partial u_m}{\partial z} \right), \tag{4}$$

where u_m is the depth-dependent horizontal velocity in the fluid-mud layer, u_{0w} is the free stream horizontal velocity in the water layer, just above the fluid-mud layer, ρ_w, ρ_m are water and fluid-mud layer densities, and v is the effective mixture viscosity containing both molecular viscosity, mud enhanced viscosity, and turbulent eddy viscosity. In the case of turbulent flow, where the eddy viscosity (v_t) could be much larger than v_m, the eddy viscosity could be used in place of v, likewise for laminar flow v_m could be used. The equation for horizontal wave motions in the water layer is

$$\rho_w \frac{\partial u_w}{\partial t} = -\frac{\partial p_w}{\partial x}, \tag{5}$$

where p_w is the pressure in the water layer due to the waves and the water viscosity is assumed to be negligible. The boundary conditions are no slip at the seafloor, and no shear approaching the lutocline, but shear at the interface is permitted. A solution based on a thin fluid-mud layer ($kh_m \ll 1$) assumption presented by *Kranenburg* et al. [2011] is used to find the real and imaginary parts of the wavenumber (Re (k) and Im (k)) via a numerical root finding technique of a fourth-order dispersion relation [*Kranenburg et al.*, 2011, equation 25]

$$A_1\, \omega^4 + B_1 \omega^3 + B_2 \omega^2 + B_3 \omega + A_2 = 0. \tag{6}$$

The coefficients of the dispersion relation depend on the complex wave number (k), the water layer thickness and density (h_w, ρ_w), fluid-mud layer thickness and density (h_m, ρ_m), oscillatory viscous
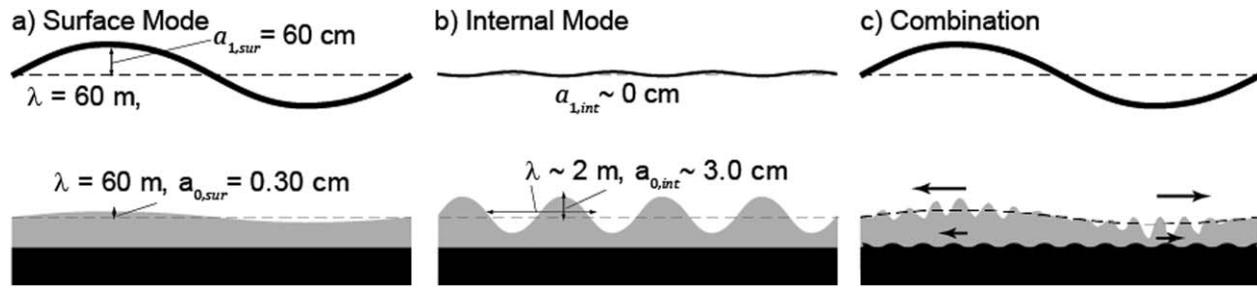
Figure 1. Schematic diagram of the two-layer system showing: (a) the surface wave mode with the same frequency and wavelength for both the air-water and water-mud interface waves; (b) the internal wave mode with the same frequency as the surface mode, but much shorter wavelength for the water-mud interface waves, and (c) the combination of the two. The arrows in Figure 1c indicate shear across the mud-water interface and the bed shows the presence of bedforms.

boundary layer thickness (δ_v), and gravity (g). The Stokes boundary layer thickness $\delta_v = \sqrt{2v_m/\omega}$, which includes the effective mixture viscosity (v_m) due to the sediment laden fluid, can be used to calculate a normalized fluid-mud layer thickness ($\hat{h}_m = h_m/\delta_v$). This two-layer dispersion relation is similar to the thin lower layer solution presented by *Dalrymple and Liu* [1978], except it neglects viscosity in the upper water layer. Because the dispersion relation is fourth order with respect to ω, it has four complex roots that correspond to solutions for the positive and negative direction propagating surface mode waves and positive and negative direction propagating internal mode waves. The lutocline fluctuations of the surface mode have the same frequency and wavelength as the surface waves (Figure 1) and, except for very high viscosities, the internal mode has the same frequency as the surface wave, but a much shorter wavelength [*Dean and Dalrymple*, 1984]. Due to the mismatch in wavelength between the surface waves and the lutocline internal mode waves, the internal mode has not received much attention as a possible source of dissipation.

In the limit of $h_m \to 0$, the dispersion equation reduces to the clear water dispersion relation

$$\omega^2 = gk \tanh kh_w, \tag{7}$$

that only supports surface mode waves due to its quadratic form *Kranenburg et al.* [2011]. In the limit of $h_w \to \infty$ and zero viscosity in the lower layer, this reduces to the internal wave dispersion relation for a finite thickness lower layer

$$\omega^2 = \frac{g'k \tanh(kh_m)}{1+(\rho_m/\rho_w)\tanh(kh_m)}, \tag{8}$$

where $g' = g(\rho_m - \rho_w)/\rho_m$. For small viscosities, equations (7) and (8) are useful expressions for finding the wavelength of surface and internal modes and aid in selecting initial guesses in root finding algorithms. For the external mode, the normalized spatial attenuation rate can be calculated by $k_{sur} = 2\mathrm{Im}(k)$. If the fluid-mud viscosity is known for either surface or internal mode waves the viscous dissipation can be calculated by

$$D_v = \rho_m \, v_m \overline{\int_0^{h_m} \left[2\left(\frac{du_m}{dx}\right)^2 + \left(\frac{dw_m}{dx} + \frac{du_m}{dz}\right)^2 + 2\left(\frac{dw_m}{dz}\right)^2 \right] dz}, \tag{9}$$

where the overbar indicates an average over wave phase. For the surface mode (subscript *sur*), where the wavelengths are much greater than the thickness of the fluid-mud layer, the vertical shear in horizontal velocity in the fluid-mud layer (u_m) is dominant source of dissipation, and equation (9) is approximated by

$$D_{v,sur} = \rho_m \, v_m \overline{\int_0^{h_m} \left(\frac{du_m}{dz}\right)^2 dz}. \tag{10}$$

An approximate analytic solution for the velocity profile can be found by assuming Re(k) is zero, which is equivalent to an infinitely thick upper layer solution of equations (4) and (5), is

$$\tilde{u}_m(z) = \frac{\rho_w}{\rho_m}\tilde{u}_{w0}\left\{1 - \cosh\left[(1+i)\;\frac{z}{\delta_v}\right] + \tanh\left[(1+i)\;\frac{h_m}{\delta_v}\right]\sinh\left[(1+i)\;\frac{z}{\delta_v}\right]\right\}. \tag{11}$$

where $\tilde{u}_m(z)$ represents the complex amplitude of the velocity profile in the fluid-mud layer. The phase of the horizontal orbital velocity amplitude in the fluid-mud layer relative to the water layer is defined as

$$\phi_u = \tan^{-1}(\text{Im}\,(\tilde{u}_m(z))/\text{Re}\,(\tilde{u}_m(z))). \tag{12}$$

The velocity profile calculated by equation (11) can be used in an inverse approach to estimate the unknown parameters v and ρ_m by fitting measured velocity profiles to model solutions. In the inverse solution, the estimate for v is sensitive to the curvature of the velocity profile and the estimate for ρ_m is sensitive to the shear at the lutocline due to ρ_w/ρ_m in (11). Due to the sensitivity of the inverse estimates for ρ_m to the shear in lutocline small errors in the measurements of shear at the lutocline can lead to large errors in the estimates for ρ_m. In the case of turbulent flow in the fluid-mud layer, the two-layer assumption is approximate and the interfacial shear could be smoothed by turbulence. Thus, the inverse estimates for density based on the velocity profile have much greater uncertainty in the turbulent flow conditions. As an alternative to the inverse approach based on a model velocity profile, the complex or time and depth-dependent viscosity can be calculated directly from the horizontal momentum equation

$$v = -\int_z^{h_m}\frac{\partial}{\partial t}\left(u_m - \frac{\rho_w}{\rho_m}u_{0w}\right)dz \Big/ \frac{\partial u_m}{\partial z}. \tag{13}$$

Using the horizontal momentum balance (4) also allows an estimate of dissipation that does not contain v

$$D_{md} = -\rho_w u_{0w}\,\overline{\int_0^{h_m}\frac{\partial u_m}{\partial t}\;dz}, \tag{14}$$

which is useful for data analysis where v is unknown.

The attenuation rate due to viscous dissipation of the internal mode (designated by subscript *int*) oscillations $\kappa_{int} = D_{int}/F_{sur}$ can be calculated by using the internal mode velocity profiles in equation (9). The horizontal and vertical velocity profiles in the fluid mud (u_m, w_m) and water (u_w, w_w) layers are given in *Kranenburg et al.* [2011] (Appendix A). For the surface mode solution, the surface wave amplitude ($\tilde{a}_{1sur}$) is specified and the amplitude of the lutocline oscillations ($\tilde{a}_{0sur}$) are found using equation 41 from *Kranenburg et al.* [2011]. For the internal mode, $\tilde{a}_{0int}$ is specified and $\tilde{a}_{1int}$, which is usually very small due to the rapid decay away from the interface, is calculated using the same equation.

An approximate analytical expression for the surface mode dissipation based on equation (11) is

$$D_{sur} = \frac{\rho_w^2\tilde{u}_{0w}^2\omega h_m}{2\rho_m}\quad\text{Re}\left[\frac{1+i}{2\hat{h}_m}\tanh\left((1+i)\hat{h}_m\right)\right]. \tag{15}$$

This expression shows that the nondimensional dissipation $\hat{D}_{sur} = 2D_{sur}\rho_m\,/\rho_w^2\tilde{u}_{0w}^2\omega h_m$ can be expressed solely as a function of $\hat{h}_m$. To examine the dependency of the parameters κ, k, and ϕ_u on the fluid-mud layer parameters h_m, ρ_m, and v_m, calculations were performed over a range of h_m, ρ_m, and v_m values for both surface and internal modes (Figure 2). The surface mode solutions for Re(k) show the expected behavior of approaching the solution with no fluid-mud layer (7) as $k_{sur}h_m \ll 1$ (Figure 2b). The surface mode solutions for κ_{sur} show the resonant behavior discussed in the literature [*Dalrymple and Liu*, 1978; *Gade*, 1958] with maximum $\hat{D}_{sur} = 0.42$ at $\hat{h}_m = 1.12$ (Figure 2a). The dissipation is linearly dependent on the ratio of ρ_w^2/ρ_m, thus is not highly sensitive to fluid-mud density within the range of relevant values of ρ_m equal to 1050–1300 kg/m³, as compared to the order of magnitude changes relative to $\hat{h}_m$. Near the peak in attenuation, the phase varies from $\phi_u = 0°$ at large values of $\hat{h}_m$ to $\phi_u = -90°$ at small values of $\hat{h}_m$ (Figure 2c). This rapid variation in phase near $\hat{h}_m = 1$ is useful for fitting the model parameters to data as the variations in attenuation are relatively weak near $\hat{h}_m = 1$.
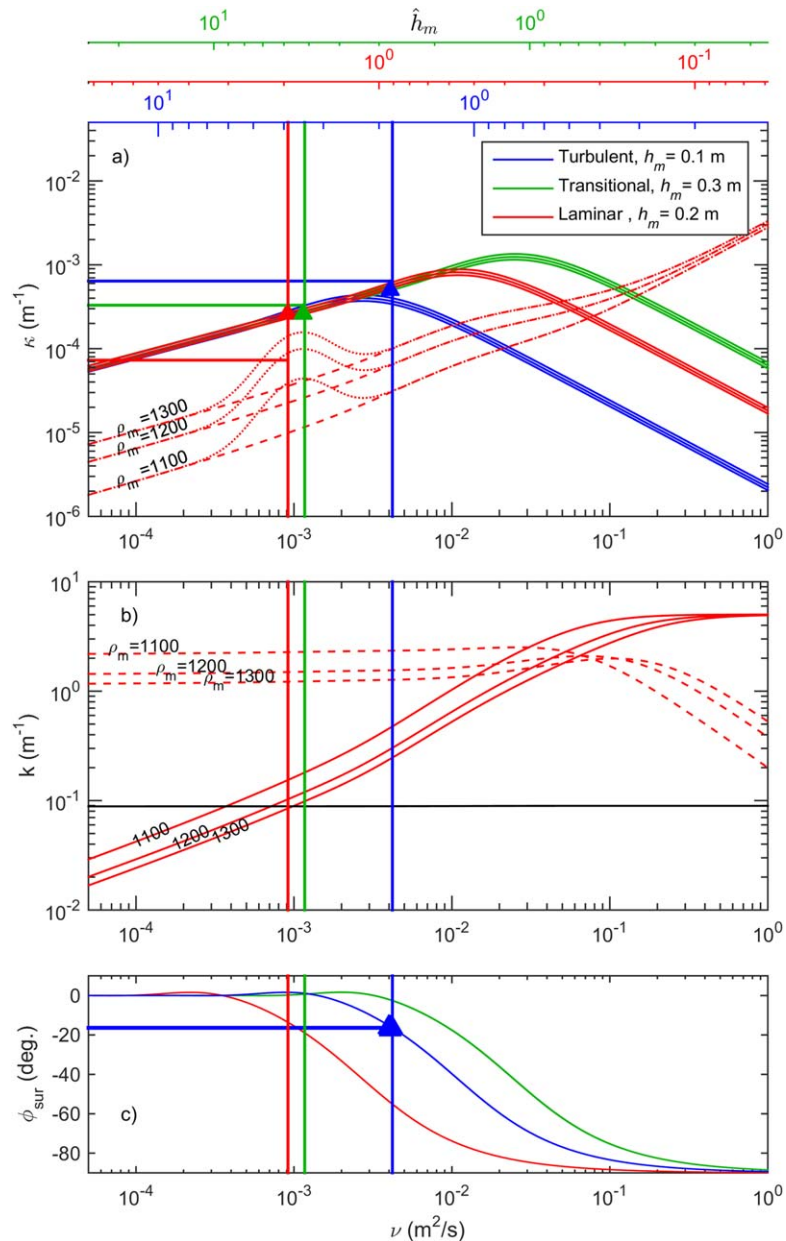
Figure 2. (a) Two-layer model results for spatial attenuation rate for the surface mode κ_{sur} (solid) and internal mode κ_{int} (dashed) for ρ_m = 1100, 1200, and 1300 kg m^{-3} as a function of normalized fluid-mud layer thickness ($\hat{h}_m$, upper x axis) and fluid-mud layer viscosity (ν, lower x axis). The three sets of green, red, and blue lines represent varying values of h_m (0.3, 0.2, and 0.1 m) based on field conditions for transitional, laminar, and turbulent conditions. Horizontal colored lines represent field measurements of $\kappa_{9,5}$ from the surface wave energy flux divergences from the turbulent (blue), transitional (green), and laminar (red) fluid-mud layer flow conditions. Vertical colored lines represent estimates of ν from boundary layer velocity profile measurements with triangles denoting the value of κ estimated from the boundary layer measurements. Intersection of the horizontal line and the vertical lines near the triangles indicates good agreement between the boundary estimates and surface flux estimates. (b) Re(k_{int})—red dashed Im(k_{int})—red solid, and Re (k_{sur})—solid black for the three different densities and h_m = 0.1 m, (c) Phase ($\phi_{u,sur}$) of horizontal orbital velocity in the fluid-mud layer (u_{m0}) relative to the free stream horizontal orbital velocity in the water (u_{w0}) for turbulent, and laminar fluid-mud layer flow conditions. The horizontal red line is vertically averaged phase from boundary layer measurements during the laminar flow period.

While the solutions of *Kranenburg et al.* [2011] and the solutions presented here, (11) and (15), do not explicitly contain an elastic component to the mud constitutive relation, elasticity can be included in these equations by using a complex viscosity, where the imaginary part of the complex viscosity is related to the elastic shear modulus [e.g., *Jiang and Mehta*, 1995]. Regardless of the particular elastic model chosen (e.g., Hookean, Voigt, or Maxwell), the effect of adding an elastic component to the viscosity is to further increase the phase lead beyond that predicted by the purely viscous model. An elastic bed with viscous fluid-mud

layer above it would also result in an increased phase lead. In fact, in purely horizontally uniform viscous flow, the only way to reduce the phase lead of the mud layer from that predicted by the purely viscous model is to use a negative elastic shear modulus, which is less physically intuitive than a positive shear modulus. This dependence of the phase of the velocity on the shear modulus is used to infer that measurements showing a phase lead smaller than predicted by a purely viscous model are not due to an elastic component of the mud constitutive relation (section 4.5.1).

Unlike the surface mode, where the amplitude of the lutocline oscillations ($\tilde{a}_{0sur}$) is directly related to the surface wave amplitude ($\tilde{a}_{1sur}$), the internal mode amplitude ($\tilde{a}_{0int}$) is indirectly related to $\tilde{a}_{1sur}$. Consequently, unlike the surface mode where κ_{sur} is independent of $\tilde{a}_{1sur}$, κ_{int} (defined as $\kappa_{int} = D_{int}/F_{sur}$) depends on the ratio $\tilde{a}_{0int}/\tilde{a}_{1sur}$. In Figure 2a, the ratio of the internal mode amplitude to the external mode amplitude $\tilde{a}_{0int}/\tilde{a}_{1sur}$ was both set to a constant value and allowed to vary. The constant value of 0.075 was based on the observations during and well after the peak of a wave event, (section 4.5). These lines neglect any covariance between $\tilde{a}_{0int}/\tilde{a}_{1sur}$ and $\hat{h}_m$ that may exist. A second set of lines in Figure 2 shows a Gaussian-shaped increase in the ratio of $\tilde{a}_{0int}/\tilde{a}_{1sur}$ from background levels of 0.075 to 0.2 in the vicinity of $\hat{h}_m = 4$ based on observations. Other parameters used in Figure 2 are also set based on the observations of $\tilde{a}_{0sur} = 0.5$ m, $\omega = 0.7$ s^{-1}, $h_m = 0.20$ m, and $h_w = 7$ m.

The real part of the internal mode wave number ranges from 1.4 to 3.6 m^{-1} as the fluid-mud layer density varies from 1100 to 1300 kg/m^3 in the thick normalized fluid-mud layer regime ($\hat{h}_m > 1$). These solutions are fairly sensitive to fluid-mud layer density due to the approximate proportionality of Re(k_{int}) to ($\rho_m + \rho_w$)/($\rho_m - \rho_w$) in the $\hat{h}_m > 1$ regime. For small $\hat{h}_m$, the value of Re(k_{int}) falls off as $\hat{h}^2_m$; thus, the wavelength of the internal mode can become tens of meters with high viscosities, low frequencies, or thin fluid-mud layers.

For $\hat{h}_m > 1$, the imaginary part of k_{int} is considerably smaller than the real part, but increases to values comparable to the real part near $\hat{h}_m = 1$, indicating highly damped oscillations. The attenuation of the surface waves by internal mode dissipation (κ_{int}) calculated with a constant ratio of $\tilde{a}_{0int}/\tilde{a}_{1sur} = 0.075$ is 1–2 orders of magnitude, depending on the fluid-mud layer density, less than κ_{sur} until values of $\hat{h}_m = 1$ (Figure 2b). With this assumption of a constant ratio of $\tilde{a}_{0int}/\tilde{a}_{1sur}$, the value of κ_{int} becomes larger than κ_{ext} at $\hat{h}_m$ less than 0.5. However, these small values of $\hat{h}_m$ below 0.5 are outside the expected parameter space where mud-induced dissipation is expected to be significant; thus based on this analytical analysis, the surface mode appears to be dominant mechanism for viscous damping. While the internal mode oscillations are not expected to dominate the direct viscous damping of surface waves, the internal mode oscillations may play a significant role in the transition from laminar to turbulent flow (section 4.7.3).

2.1.1. Velocity Profiles

The horizontal and vertical velocity profiles for the external and internal modes provide both insights into the mechanisms of viscous dissipation and a useful diagnostic tool for fitting model parameters based on measurements of velocity profiles. For this reason, vertical profiles of surface mode horizontal velocity amplitude ($|\tilde{u}_{sur}|$) and phase for four different values of viscosity ($v = 1.0 \times 10^{-5}$, 1.2×10^{-3}, 4.2×10^{-3}, and 0.1 m^2/s corresponding to $\hat{h}_m = 21$, 3.4, 1.8, and 0.4) are shown in Figure 3a. The upper and lower values of v were chosen as limiting values for demonstration purposes, and the two central values are representative of periods in the data for transitional and laminar flow (section 4.5). The profiles of $\tilde{u}_{sur}$ were calculated using an $\tilde{u}_{0w} = 0.09$ m/s, based on observations during a period of laminar flow. The lowest $\hat{h}_m$ case shows large shear at the lutocline with low velocities within the fluid-mud layer, which results in low dissipation. The large $\hat{h}_m$ case shows weak shear at the mud-water interface and large shear at the bottom of the fluid-mud layer. This case, with a wave boundary layer much thinner than the fluid-mud layer, also does not produce large dissipation rates. The cases with $\hat{h}_m$ close to 1 show a wave boundary layer that is approximately the same thickness as the fluid-mud layer resulting in maximum dissipation. The velocity profiles with $\hat{h}_m = 3.4$ and 1.8 have similar shapes, but the phase shift across the lutocline from 0° to 16° for these two cases. Since Figures 3a and 3b show the magnitude and phase of $\tilde{u}_{sur}$, they do not directly show the instantaneous shear across the lutocline. Due to the 0°–16° phase shift, there is a velocity difference of up to 2.5–5 cm/s across the interface. If the internal mode oscillations are forced by interfacial shear from the surface mode oscillations then these maximum velocity shears could set an upper bound for the amplitude of the internal mode.
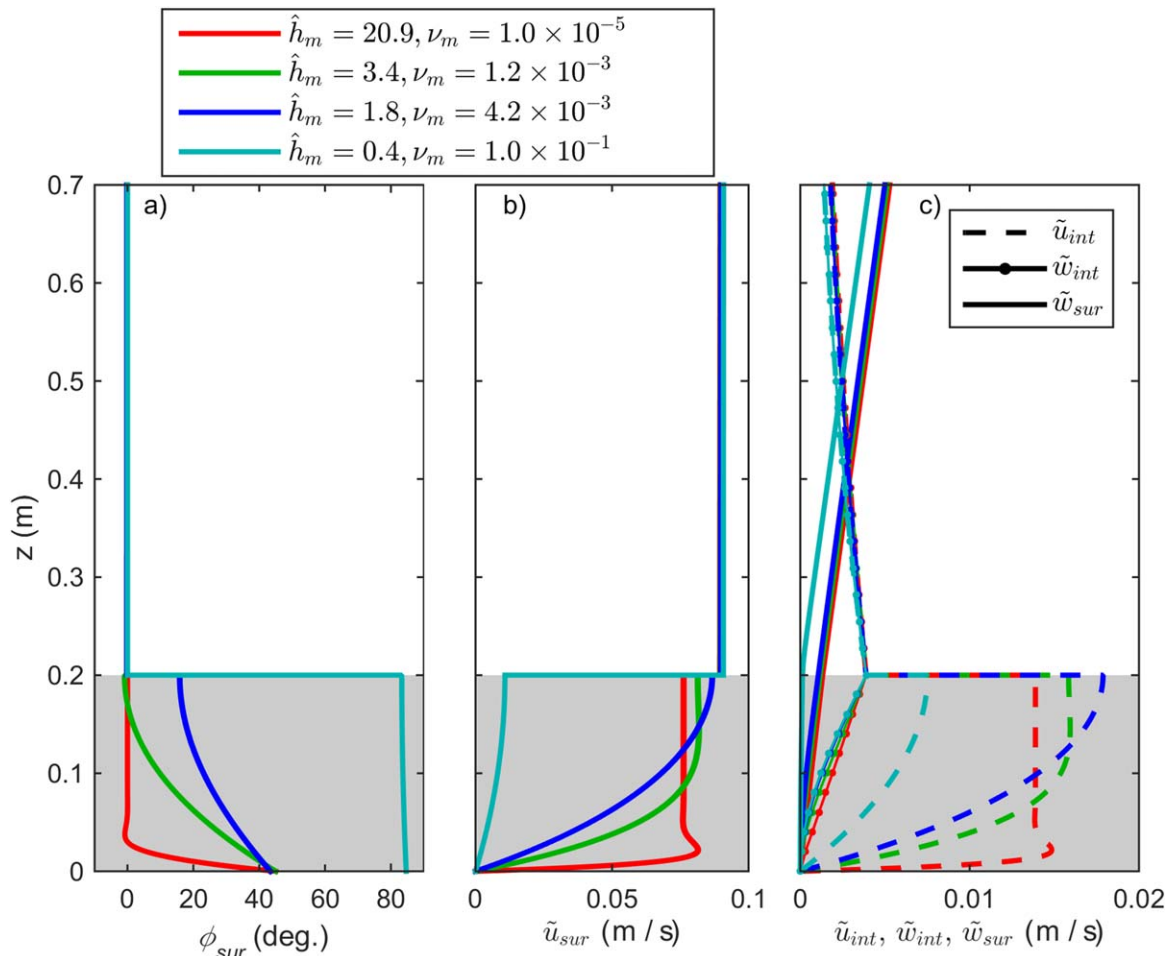
Figure 3. (a) Profiles of surface mode phase ($\phi_{u,sur}$) for four different values of $\hat{h}_m$ (colored lines) set by varying v with a constant $h_m = 0.20$ m. (b) Profiles of $\tilde{u}_{sur}$ for the different values of $\hat{h}_m$. (c) Profiles of $\tilde{u}_{int}$ (dashed lines), $\bar{w}_{int}$, (solid lines with dots), and $\bar{w}_{sur}$ (solid lines) orbital velocity amplitudes.

In Figure 3c, vertical profiles of external mode vertical velocity ($\bar{w}_{sur}$) and both components ($\tilde{u}_{int}$, $\tilde{w}_{int}$) of internal mode velocity are shown. The profiles of $\tilde{u}_{int}$ and $\tilde{w}_{int}$ were calculated using an internal mode amplitude of $\tilde{a}_{0int} = 0.75$ cm based on observations and consistent with the approximately constant ratio of $\tilde{a}_{0int}/\tilde{a}_{1sur} = 0.075$. With this ratio and an assumed density of $\rho_m = 1200$ kg/m³, the internal mode vertical velocity at the mud-water interface ($\tilde{w}_{0int}$) is at least a factor of three greater (typically a factor of 5) than the surface mode vertical velocity at the mud-water interface ($\tilde{w}_{0sur}$) depending on the chosen viscosity. The $\tilde{u}_{int}$ profiles have similar vertical structure as $\tilde{u}_{sur}$ within the fluid-mud layer, but have magnitudes approximately five times smaller. Because the vertical structure is similar to the surface mode, the reduced magnitude causes reduced dissipation due to the internal mode shown in Figure 2b. The $\tilde{u}_{int}$ have an approximately 180° phase shift across the lutocline and decay away from the interface with a decay rate set by Re(k_{int}), thus the shear in $\tilde{u}_{int}$ across the lutocline is comparable to the shear in $\tilde{u}_{sur}$.

2.2. Turbulent Flow
In addition to the viscous laminar mechanisms for dissipation in the absence of turbulence described above, wave energy can also be dissipated by turbulent processes typically described by the balance of shear production against viscous dissipation and losses due to work against density gradients (buoyant destruction of turbulent kinetic energy). To characterize the flow the Reynolds number is calculated by $Re_A = \tilde{u}_{0m}^2/\omega v_m$, where $\tilde{u}_{0m}/\omega$ is a length scale defined by the wave orbital semiexcursion (A) at the top of the fluid-mud layer and v_m is the fluid-mud layer viscosity. Because other studies use a Reynolds number defined by the Stokes viscous wave boundary thickness ($Re_\delta = \tilde{u}_{0m}\delta_v/v_m = \sqrt{2Re_A}$), these values are also

included in Table A1. Also for the purpose of comparison with other studies, a Reynolds number based on clear water $Re_{A,cw}$ and $Re_{\delta,cw}$ are also calculated using values of molecular viscosity of seawater without sediment.

In fully turbulent flow, dimensional analysis results in velocity spectra $S(k)$ proportional to $\varepsilon_t^{2/3}k^{-5/3}$ in the inertial subrange defined by $\eta_k < k^{-1} < l$ [*Tennekes and Lumley*, 1972]. Here l is the size of the largest eddies, which are bounded by the fluid-mud layer thickness, ε is the local dissipation rate, and $\eta_k = (v^3/\varepsilon)^{1/4}$ is the Kolmogorov microscale, defining the maximum spatial scale for viscous dissipation. Typically, the Reynolds number is used to determine if the flow is turbulent or laminar; however, in this situation, with a maximum spatial scale set by the thickness of the fluid-mud layer, the Kolmogorov microscale relative to the thickness of the stokes boundary layer could also provide a reasonable criteria for the transition from turbulent to laminar flow. As suspended sediment concentration and viscosity increase, η_k becomes larger than the fluid-mud layer thickness or the wave boundary layer thickness and turbulent fluctuations are highly suppressed, resulting in dissipation through direct action of viscosity on the velocity gradients in the wave boundary layer. Using Taylor's frozen turbulence hypothesis for oscillatory flows, η_k can be recast as a Kolmogorov frequency $\eta_f = \tilde{u}_{0m}/\eta_k$.

For calculation of η_k and Re, both v and ε are estimated from the vertical structure of the boundary layer profile using equation (10) to calculate ε, and the fit of measured velocity profile to the model solution described by equation (11) to optimize the choice of v. The curvature of the velocity profile and resultant combined viscosity (v) has contributions from turbulent processes via the eddy viscosity (v_t) and laminar processes via the mud-enhanced mixture viscosity (v_m). For laminar flows, this is fairly consistent as the shape of the boundary layer velocity profile is determined by the fluid-mud enhanced viscosity. As the contributions of turbulent dissipation become significant or dominant, the approach of using the total viscosity inferred from the shape of the velocity profile could result in inconsistent Reynolds number calculations, and calculating the Reynolds number based on a clear water value of v is preferable.

An estimate of turbulent dissipation based on vertical velocity fluctuations can be calculated from the inertial dissipation method

$$\varepsilon_{t,IDM} = B_w S_{ww}^{3/2}(f)f^{5/2}/u_{0m}, \tag{16}$$

where the constant B_w ranges from 7 to 14 for flows where the turbulence is advected by both waves and mean flows [*Hay*, 2008; *Trowbridge and Elgar*, 2001]. In a similar manner to the across-shelf wave energy flux divergence dissipation factor ($f_{e,Fx}$, equation (3)), a local turbulent wave dissipation factor based on the inertial dissipation method can be calculated by

$$f_{e,IDM} = \frac{\rho_m \displaystyle\int_0^{h_m} \varepsilon_{t,IDM}\,dz}{\frac{2}{3\pi}\rho_w \tilde{u}_{0w}^3}. \tag{17}$$

While this approach to estimating turbulent dissipation has been widely used, it is highly sensitive to deviations from the conditions that are required for its use due to the cubic dependence on the velocity fluctuations. As the turbulent eddies become anisotropic, due to large-scale shear, stratification, or proximity to a boundary, the mismatch between horizontal and vertical velocity gradients could lead to large errors in the dissipation estimates [*Bluteau et al.*, 2011]. In section 4.5.3, techniques to estimate the anisotropy will be examined.

A simple estimate for turbulent shear velocity suggested by *Nielsen* [1992] and *Smyth and Hay* [2002] uses the square root of the variance of turbulent vertical velocity fluctuations

$$u_* = 2\sigma_{w'}, \tag{18}$$

where $\sigma_{w'} = \left(\overline{w'^2}\right)^{1/2}$. The turbulent fluctuations are defined by a separation of mean ($\bar{u}$), orbital ($\tilde{u}$), and turbulent (u') components, e.g., $u = \bar{u} + \tilde{u} + u'$. To reduce the potential for contamination due to wave motions in this estimate, the fit of $S_{ww}^{3/2}(f)f^{5/2}$ is used to calculate $\varepsilon_{t,IDM}$ in equation (16) in the inertial subrange is integrated through the wave band:

$$\overline{w'^2} = \left(\frac{\varepsilon_{t,IDM}\tilde{u}_{0w}}{B_w}\right)^{2/3}\int_{f_l}^{f_u} f^{-5/3}df.$$

(19)

This results in a friction factor based on $\overline{w'^2}$

$$f_{w,w'} = 2u_*^2/\tilde{u}_{0w}^2.$$

(20)

It is straightforward to compare this wave friction factor estimate $f_{w,w'}$ to estimates based on data in the literature such as the *Nielsen* [1992] formula:

$$f_{w,N} = \exp\left[5.5(r/A)^{0.2} - 6.3\right].$$

(21)

Here A is the near-bed wave orbital motion semiexcursion defined by $A = \tilde{u}_{w0}/2\pi f_{0w}$, and r is the hydraulic roughness. In addition, *Nielsen* [1992] suggests that wave friction factors are roughly similar to wave dissipation factors, thus allowing comparison of these quantities. The similarity of f_w and f_e is expected when using a momentum balance approach to calculate dissipation such as $D = \overline{\tau_0 u_{0w}}$, where τ_0 is the bed stress. In this case, as long as the phase difference between τ_0 and u_{0w} is between $\phi = 0$ and $70°$, the phase average of $\cos(\omega t + \phi)\cos(\omega t)|\cos(\omega t)|$ is between 3 and 1, and f_w and f_e should be within a factor of 3. If the phase difference is greater than about $70°$, τ_0 and u_{0w} approach quadrature, and dissipation will become very small. For calculations of f_e based on turbulent fluctuations such as $f_{e,IDM}$, a similar magnitude to f_w is not necessarily expected since the calculations are very different.

3. Field Measurements and Data Processing

Tripods with upward looking acoustic wave and current meters (Nortek AWACs) were deployed on the 5 and 9 m isobaths to measure the across-shelf dependence of wave energy flux. The across-shelf length of the entire array was 3.0 km from the 9 m site to the 5 m site. The distance between the 9 and 7 site ($\Delta X_{9,7}$) was 1.8 km and the distance between the 7 and 5 m sites ($\Delta X_{7,5}$) was 1.2 km (Figure 4). The tripods were deployed on a line perpendicular to the coastline and isobaths, oriented $17°$ east of true north.

In order to measure processes at or near the lutocline, a variety of sensors were placed within 1 m of the seafloor (Figure 5). Nortek Vector Acoustic Doppler Velocimeter (ADVs) with pressure sensors had velocity sampling volumes located at 30 and 50 cm above the footpads of the frame and were used to measure waves and currents at all three sites. Three frequency (1.0, 2.5, and 5.0 MHz) Aquatec acoustic backscatter profilers (ABS) with centimeter vertical resolution measured the sediment resuspension over the lower 1 m of the water column, thickness of fluid-mud layers, and bed elevation at the 5 and 9 m site. At the 7 m site, in addition to an upward looking RDI Acoustic Doppler Current Profiler (ADCP) and Nortek Vector ADVs, an array of five downward looking single beam pulse-coherent acoustic Doppler profilers (PCADPs) were mounted to measure centimeter vertical resolution profiles of along-beam velocity and backscattered intensity. All sensors were burst sampled with typical schedules of 20 min of data collected every 30 min. Sampling rates within the bursts varied from 2 Hz for the AWACs and ABS sensors to 8 Hz for the ADVs. All burst-averaged scalar time series data were filtered with a 3 h low-pass filter for presentation in Figures 6–9. The velocity profiles shown in color plots were not filtered.

3.1. Acoustic and Optical Backscatter
The acoustic backscatter profiles were processed to remove range-squared spreading and attenuation due to water, but attenuation due to the high sediment concentrations was not removed, due the instability of this procedure at high attenuation levels. The backscatter profiles were also scaled by a single constant to fit the OBS measurements located at 25 cm above the footpads. When fluid-mud layers were present, the 1.0 MHz backscattered intensity profile typically showed a peak at the lutocline, and a second peak at the stationary bed. This second peak was used to detect the stationary bed below the fluid-mud layers as the attenuation of the 1.0 MHz signal through the fluid-mud layer was insufficient to mask this peak. In contrast, in the 2.5 MHz signal, there was a strong return from the lutocline, but the return from the stationary bed was attenuated and not visible above the sensor noise floor when fluid-mud layers were present. A
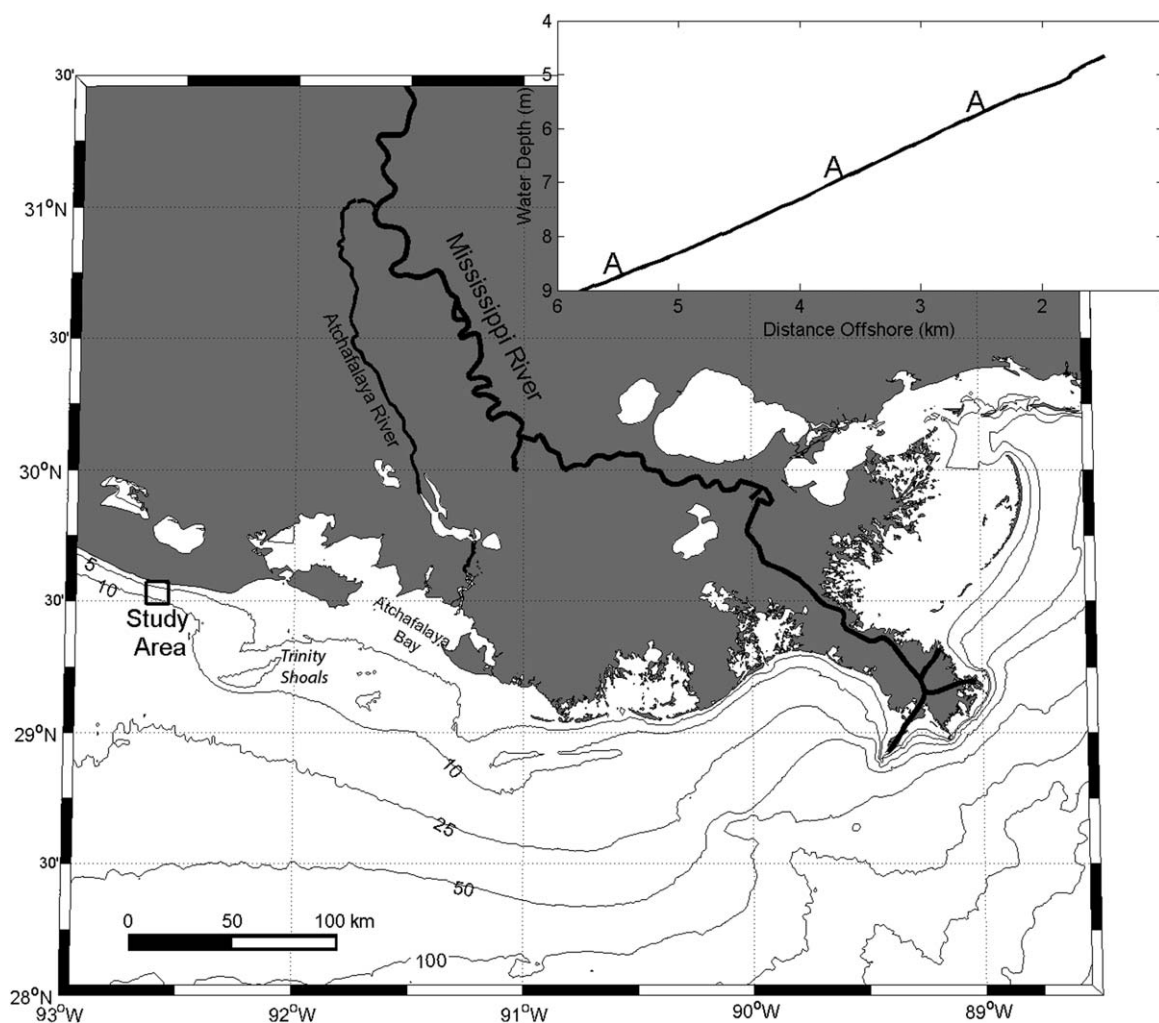
Figure 4. Map of Louisiana coast with the study site to the west of Atchafalaya Bay. Inset: Bathymetry transect and instrumented frame locations at the study site.

threshold detector was used to identify the location of the lutocline (a_0) from the 2 Hz sampled backscatter profiles, as the rapidly sampled data resolved internal mode lutocline fluctuations. The burst-averaged thickness of the fluid-mud layer (h_m) was found by differencing the 1.0 MHz stationary bed return and the median of the lutocline location from the 2 Hz sampled data. The amplitude of the lutocline waves was calculated by $\tilde{a}_0 = \sqrt{2}\sigma_{a_0}$, where σ_{a_0} is the RMS value of a_0. The location of the troughs and crests of the lutocline were also quantified by the 15th and 85th percentile of the lutocline elevation measurements (a_0), as a_0 can be highly skewed. Although surface wave mode vertical fluctuations of the interface would also be included in this estimate, these are typically at least a factor of 5 smaller than the internal mode fluctuations (section 2.1.1), thus $\tilde{a}_{0int}$ is approximately equal to $\tilde{a}_0$.

Optical backscattering sensors (OBS5 from Campbell Scientific) were also deployed on the frames at 25 cm above the footpads to measure suspended sediment concentration. This particular model of optical backscattering sensor has two detectors with different sized sampling volumes to allow calibration up to approximately 60 g/L of fine sediment in contrast to the single detector OBS maximum concentration level of approximately 5–10 g/L [*Campbell Scientific*, 2011].

3.2. Surface Wave Energy

Surface wave parameters at the 9 and 5 m sites were calculated from the AWACs which use an upward aimed acoustic beam data to directly measure the sea surface elevation (η). Swell height is estimated from the elevation spectra by
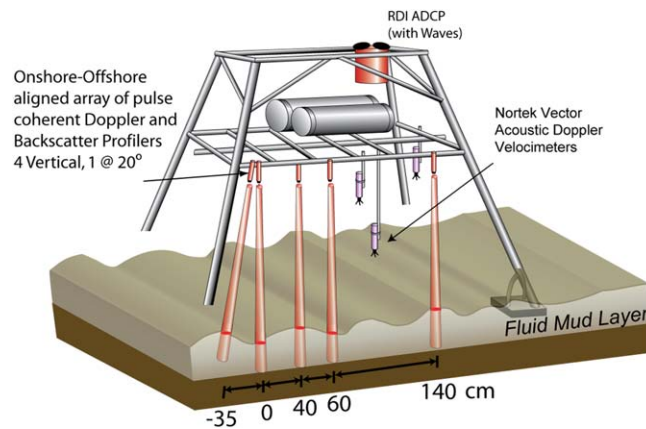
Figure 5. Schematic diagram of instrumented frame at the 7 m Site. The frames at the 5 and 9 site were similar, but without the PCADP array, and with Nortek AWAC wave sensors instead of the RDI ADCP.

$$H_{m0} = 4\sqrt{\int_{f_l}^{f_u} S_{a_1 a_1}\, df}, \qquad (22)$$

and peak period (T_p) is calculated from the peak of $S_{a_1 a_1}(f)$. The notation $H_{m0,9}$ refers to wave height at the 9 m site. Estimates of $S_{a_1 a_1}(f)$ were also calculated from direct measurements of a_1 from the upward-aimed acoustic beam of the AWACs at the 5 and 9 m site and from the ADVs at the 9, 7, and 5 sites using pressure measurement spectra

$$S_{a_1 a_1} = S_{pp}\left[\frac{\cosh(kh_w)}{\rho g \cosh(kz_p)}\right]^2, \qquad (23)$$

where z_p is the height of the pressure sensor above the seabed. The amplitudes of field-measured oscillatory variables are calculated from the *Madsen* [1994] definition of a representative quantity (e.g., $\tilde{a}_1 = H_{m0}/\sqrt{8}$) as this definition has the same variance as the single frequency quantities used in the theoretical derivations. Wave energy flux along the axis of the spatial array defined by the 9, 7, and 5 m sites is calculated by

$$F = \int_{f_l}^{f_u}\left[\frac{1}{2}\rho g S_{a_1 a_1}\right]\left[\frac{c}{2}\left(1 + \frac{2kh}{\sinh 2kh}\right)\right]\cos\theta_a\, df. \qquad (24)$$

Here the wave number (k) and phase speed (c) are calculated from the clear water dispersion relation (7) and θ_a is the frequency-dependent angle between the direction of wave propagation and the axis of the 9–5 m isobath cross-shore array calculated by

$$\theta_a = \tan^{-1}\left(S_{vp}/S_{up}\right), \qquad (25)$$

where S_{vp} and S_{up} are the covariances between pressure and the along (u_w) and across (v_w) array wave velocities. This directional dependence was included so that the analysis only considered the energy flux divergence along the axis of the array. Spectral components associated with waves propagating in the offshore direction $90° < \theta_a(f) < 270°$, were set to have $S_{a_1 a_1} = 0$, in the calculations for F as these components were likely have significant wind input, thus making the analysis of the relative contributions of wind input and mud-induced dissipation difficult.

The flux divergence and κ were calculated using the finite difference approximations: $F_{x9,5} = (F_9 - F_5)/\Delta X_{9,5}$ and $\kappa_{9,5} = 2(F_9 - F_5)/(F_9 + F_5)\Delta X_{9,5}$. For the 9–5 m site estimates, the AWAC acoustic surfacing tracking estimates were used, and for differences involving the 7 m site, where there was only an ADV with a pressure sensor to sense wave parameters, pressure-based estimates of energy flux were used.

The upper (f_u) and lower (f_l) bounds of the integration were chosen as 0.08 and 0.25 Hz to minimize flux divergence contributions from wind input and white capping losses, which occur primarily at high frequencies. In 9–5 m water depth, the nonlinear transfers of energy from the high-frequency bands where wind input and white capping energy source terms dominate is expected to be slow relative to the propagation time for the swell over the 3 km long array. SWAN (simulating waves Nearshore) model runs with large (1.2 m) and small (0.3 m) offshore wave inputs, weak (2 m/s) and strong (8 m/s) winds in both the onshore and offshore direction were conducted to test these spectral limits. As expected, the modeling results show large variability in the high-frequency $(f > 0.3$ Hz) portion of the spectra as wind strength and direction inputs were varied, but the changes to the flux divergence in the swell band defined by f_l and f_u were small (less than 7%) regardless of wind direction or strength.
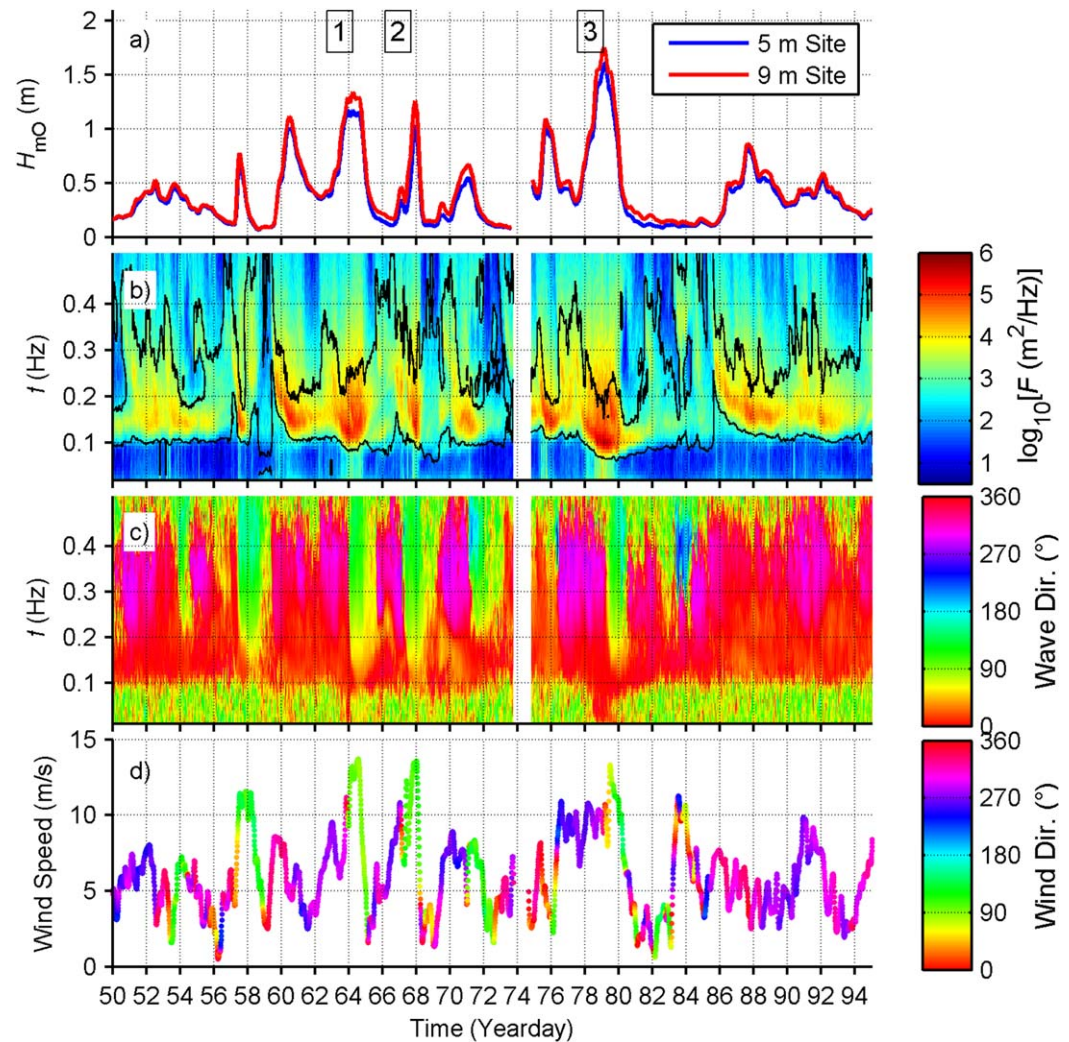
Figure 6. Time series of wave and wind parameters. (a) Wave height for 9 and 5 m sites, (b) Wave Spectra (color) with black contours indicating the portion of the spectra containing 75% of the energy for each time sample. (c) Wave directional spectra. (d) Wind speed and direction. Both wind and wave directions are in the oceanographic convention: 0° represents wind and waves coming from the south and blowing (propagating) to the north.

Representative near-bottom wave velocities were calculated from the ADV data by

$$\tilde{u}_{0w} = \sqrt{2 \int_{f_l}^{f_u} S_{uu} df} \ , \tag{26}$$

where S_{uu} is the spectra of the wave velocity components rotated into the direction along the PCADP array and a representative frequency was calculated by [*Madsen*, 1994]

$$f_{0w} = \frac{2}{\tilde{u}_{0w}^2} \int_{f_l}^{f_u} f S_{uu} df . \tag{27}$$

During periods when the lower ADV sampling volume was within the fluid-mud layer, the data quality became poor due to low correlations, thus the upper ADV was used, as its sampling volume was consistently located above the fluid-mud layer.
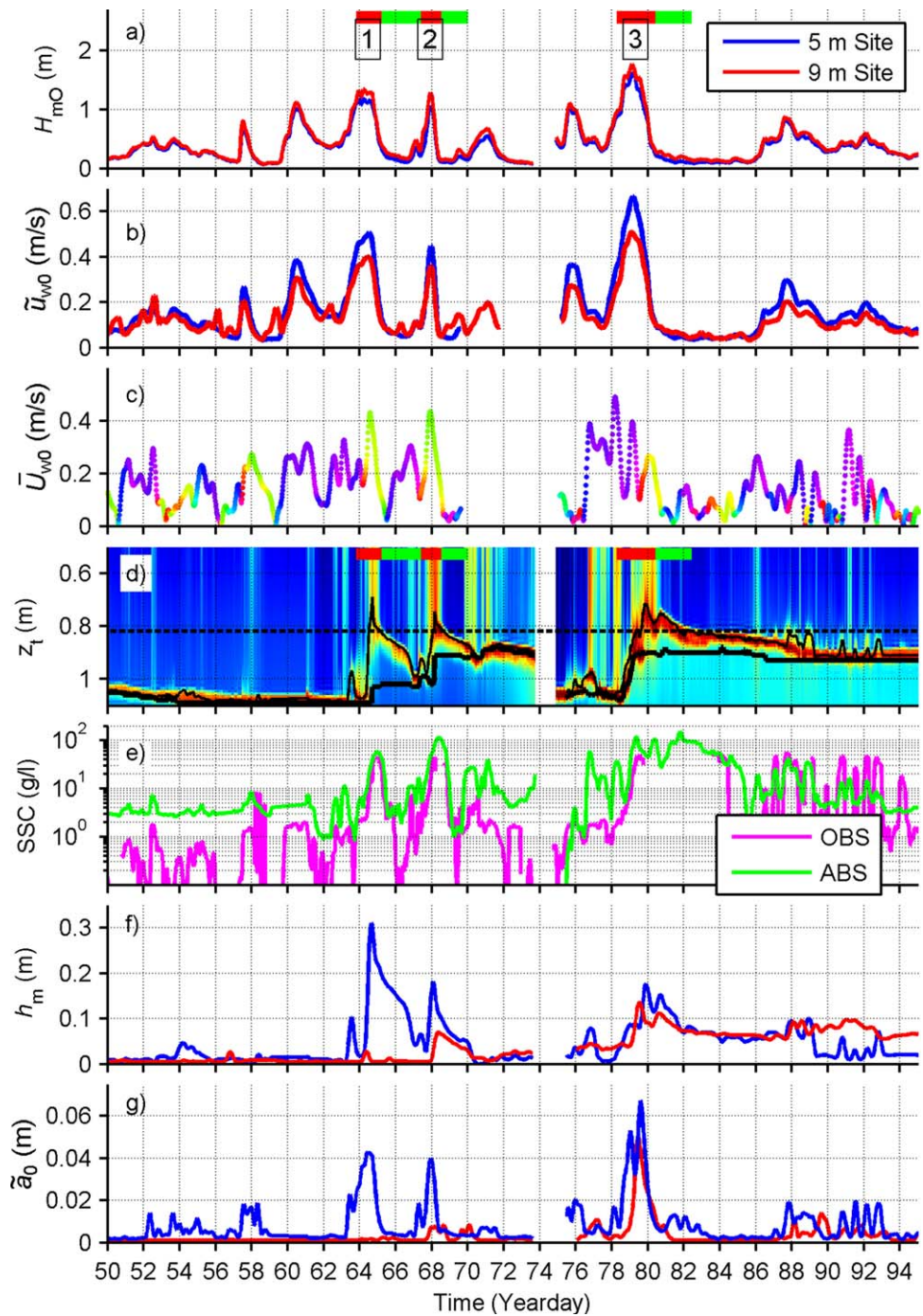
Figure 7. Time series of wave parameters and bed response. (a) Wave height for 9 and 5 m sites with three events labeled with high F and F_x indicated with the red bar and high κ periods after the wave events indicated by the green bar. (b) Wave orbital velocity amplitude from the 5 and 9 m sites just above the fluid-mud layer ($\tilde{u}_{0w}$). (c) Mean current speed just above the fluid-mud layer ($\bar{U}_{0w} = |\bar{u}_{0w} + i\bar{v}_{0w}|$) with color representing direction with the same color key as Figure 6. (d) Vertical profiles of 2.5 MHz ABS backscattered intensity from the 5 m isobath site with the location of the lutocline indicated with a thin black line and the location of the stationary bed indicated by thick black line. The dashed line indicates the elevation of the OBS. (e) OBS suspended sediment concentration and ABS data from the corresponding range bin. (f) fluid-mud layer thickness. (g) Lutocline elevation fluctuation amplitude ($\tilde{a}_0$).

3.3. Pulse-Coherent Doppler Array Boundary Layer Velocity Profiles

An array of single beam pulse-coherent acoustic Doppler profilers (PCADPs) measured vertical velocity and backscattered intensity profiles at four locations with 1 cm vertical resolution. An additional transducer
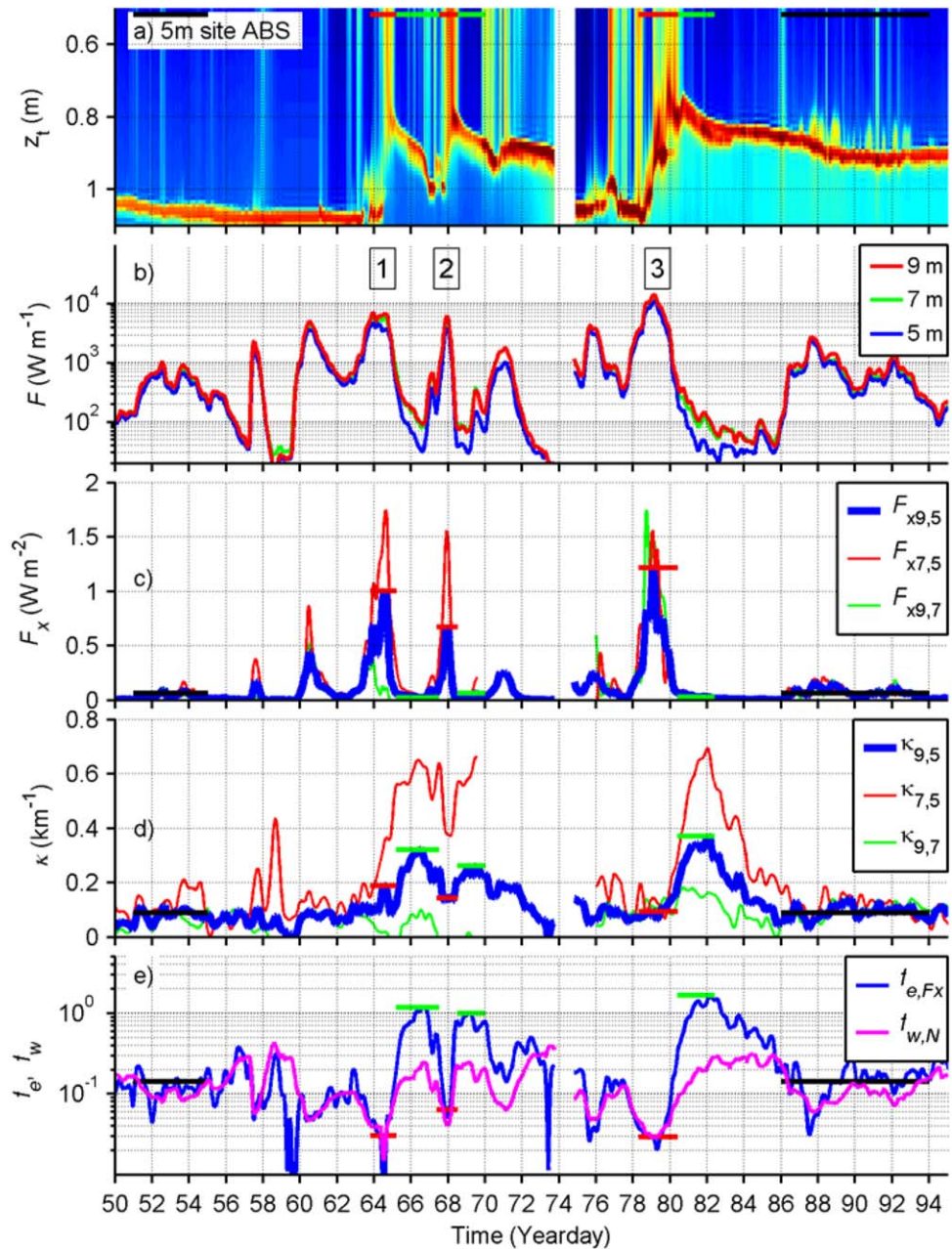
Figure 8. Time series of wave energy flux measurements. (a) The 2.5 MHz ABS backscattered intensity with high F and F_x indicated with the red bar, high κ periods after the wave events indicated by the green bar, and background wave conditions with no or low concentration fluid mud indicated by black bars. (b) Wave energy flux F for 9 (red), 7 (blue), and 5 (green) m sites with three events labeled. (c) Wave energy flux divergence (F_x) for ΔX between 9 and 5 m sites (blue), 7 and 5 m sites (red), and 9 and 7 m sites (green). (d) Wave-attenuation rate (κ) for the same ΔX as Figure 8c. (e) Wave friction factor ($f_{w,N}$) calculated from local wave velocities and wave energy dissipation factor ($f_{e,Fx}$) calculated from flux divergences between 9 and 5 m sites.

(sensor 1) located at $x = -0.35$ m, was aimed 20° off the vertical axis in the direction of the array axis to measure horizontal velocity profiles. The downward transducers (sensors 2 through 5) were located at $x = 0$, 0.4, 0.6, and 1.4 m as shown in Figure 5. The tripod was aligned with this horizontal array oriented along the north-south direction with $+x$ in the north direction, so that it was approximately parallel to the direction of the swell propagation to the north. This system transmits and receives on 40 mm diameter disc-shaped piezoceramic transducers. Signal generation, transmission, reception, and preliminary processing was performed on five high-frequency sonar boards developed at Woods Hole Oceanographic
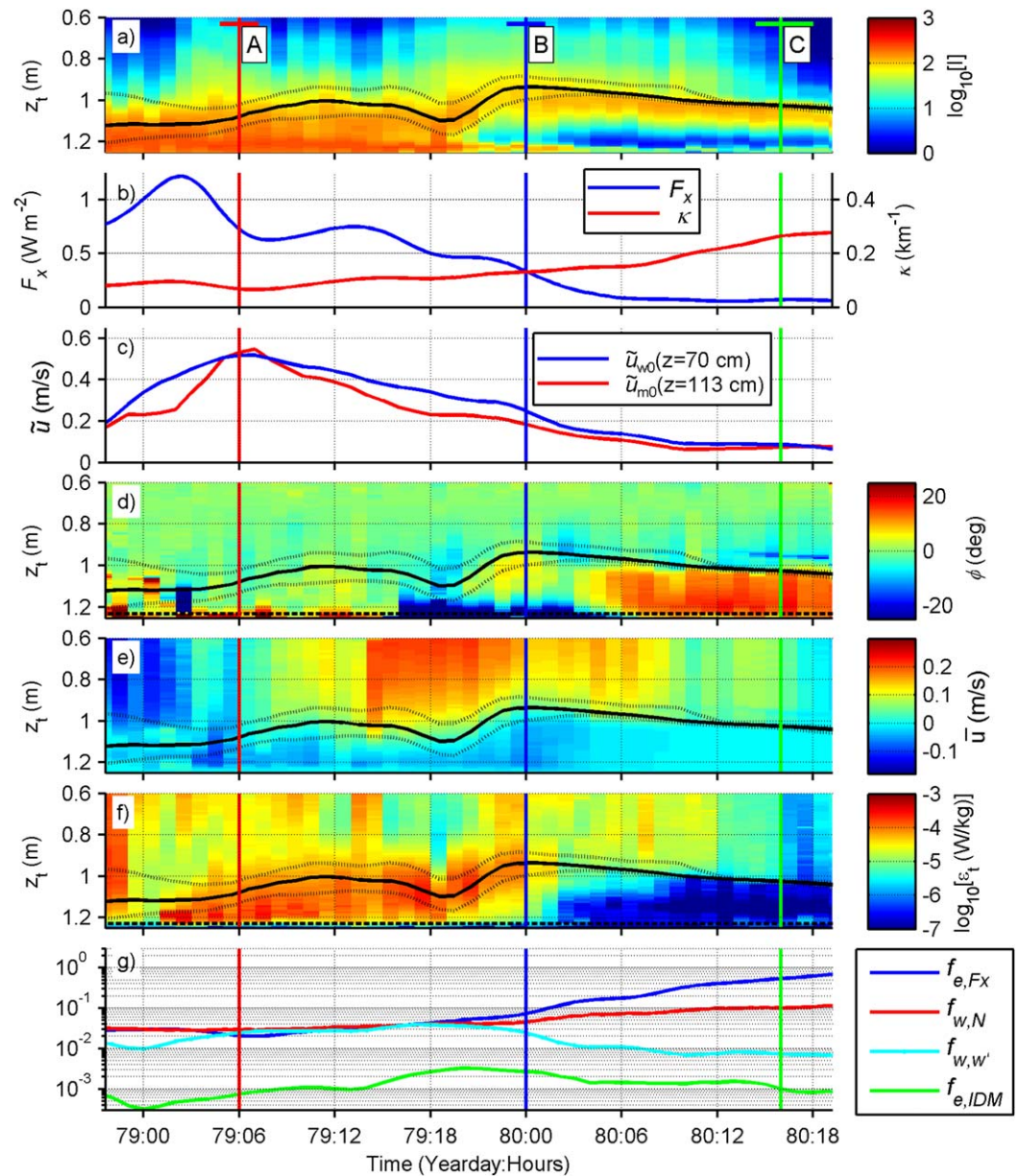
Figure 9. Time series of boundary layer measurement from the PCADP. (a) PCADP backscattered intensity with colored vertical lines in the turbulent (red), transitional (blue), and laminar (green) periods indicating bursts selected for detailed analysis and horizontal colored lines indicating averaging periods for estimates of boundary layer quantities in Table A1. The solid black line indicates the burst median location of the lutocline and the dashed lines indicate the location of the crests and troughs of the internal mode fluctuations. (b) F_x and κ. (c) Wave orbital velocity amplitudes above ($\tilde{u}_{0w}$) and below ($\tilde{u}_{0m}$) the mud-water interface. (d) Phase (ϕ_u). (e) Mean across-shore currents ($\bar{u}_{0w}$). (f) Inertial dissipation method estimates of Turbulent dissipation ($\varepsilon_{t,IDM}$).

Institution [*Jaffré et al.*, 2010]. The transducers transmitted at a frequency of $f_c = 1.0$ MHz were mounted 1.05 m above the bed. This frequency was chosen for good penetration into the fluid-mud layer, and relatively narrow beam spread. The pulse repetition rate of $T_{prf} = 2.2$ µs results in an along-beam ambiguity velocity of $V_{max} = C_a/4\, f_c\, T_{prf} = 0.17$ m/s, where C_a is sound speed. Based on $\alpha_1 = 20°$, the horizontal ambiguity velocity is 0.5 m/s. The system internally averaged real and imaginary parts of 128 sequential pulse-pair correlations and autocorrelations, and standard pulse-pair processing techniques were used to calculate along-beam velocities [*Zedel et al.*, 1996]. This averaging combined with the additional pulse-pair processing time resulted in a time between averaged velocity samples of $\Delta t = 0.29$ s. Time domain dealiasing of velocity ambiguities was performed on selected bursts, with manual intervention if the algorithm produced incorrect results. Pulse-pair averages with ping-to-ping correlations less than 40% were rejected and
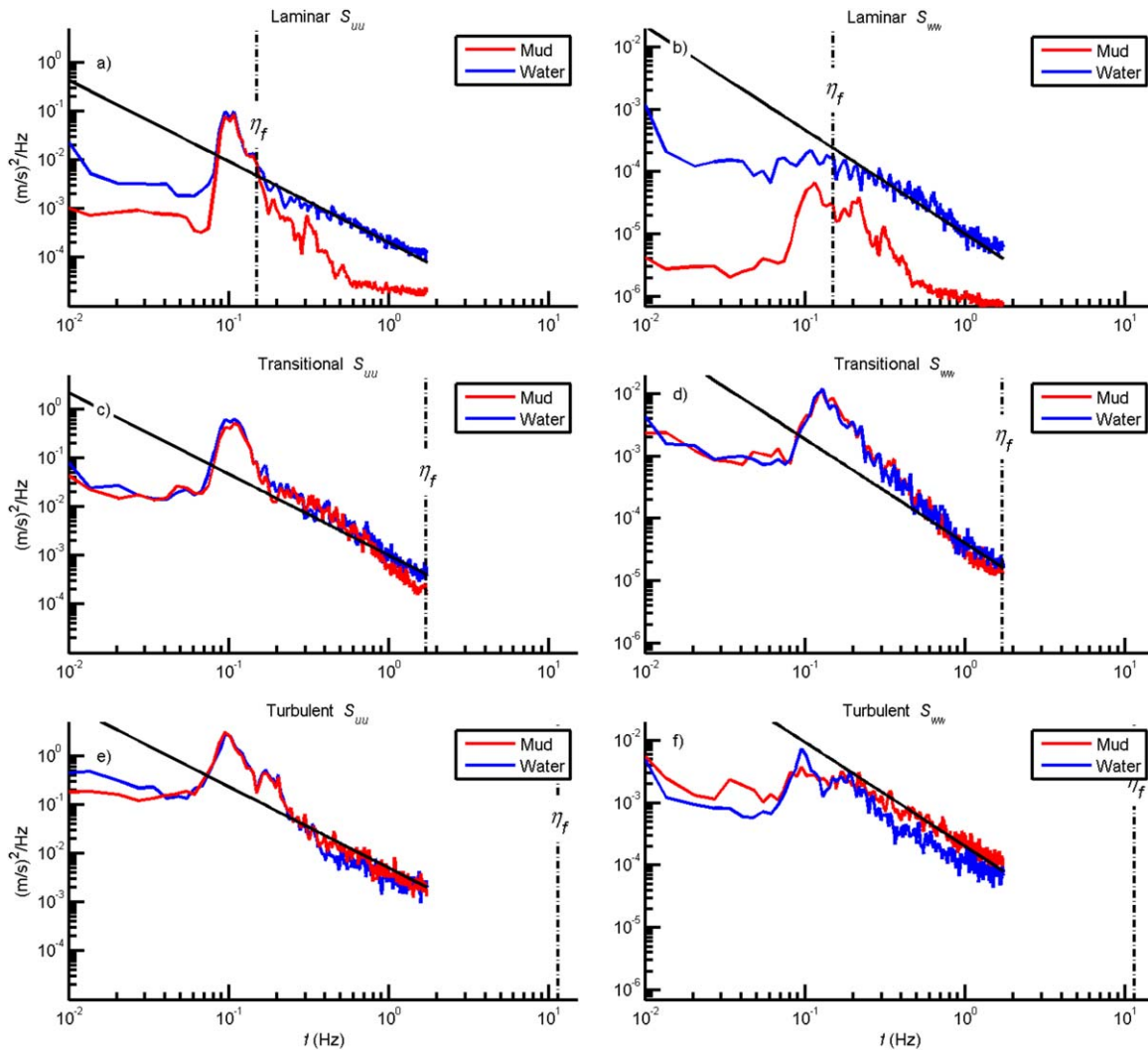
Figure 10. Laminar, Transitional, and turbulent period mud and water layer flow velocity spectra. (a) Horizontal velocity (S_{uu}) in the water (blue) and mud (red layers). (b) Vertical velocity spectra (S_{ww}).

replaced by interpolation of neighboring samples. During periods with a well-defined laminar fluid-mud layer, the correlations were generally above 40% except in the bottom 2–3 cm above the seafloor. At the lutocline, correlations decreased slightly to values around 40%. With correlations above 60%, the noise floor of the along-beam velocities was approximately 10^{-6} m^2/Hz, thus producing a noise standard deviation of 1.4 mm/s when integrated over the 2 Hz bandwidth (Figure 10). The signal in the upper 15–20 cm of the fluid-mud layer typically had high correlations, which allowed accurate measurement of wave boundary velocity profiles in the fluid-mud layer (Figures 11 and 12). As the correlations decrease, the velocity uncertainty increases as discussed by *Zedel* [2008].

The along-beam velocities from the angled ($\alpha_1 = 20°$ from vertical) beam velocities (b_1) and the adjacent vertical ($\alpha_2 \approx 0°$) beam velocities (b_2) can be written in terms of the horizontal (u_i) and vertical velocity (w_i) components in the respective sampling volume

$$b_i = u_i \sin \alpha_i + w_i \cos \alpha_i. \qquad (28)$$

Horizontal velocities (u) were calculated from v_2 and v_1

$$u(z_t) = \frac{b_1(r_t / \cos \alpha_1) - b_2(z_t)}{\sin \alpha_1}, \qquad (29)$$

where r_t is the range from the angled transducer, z_t is the vertical distance from the downward aimed
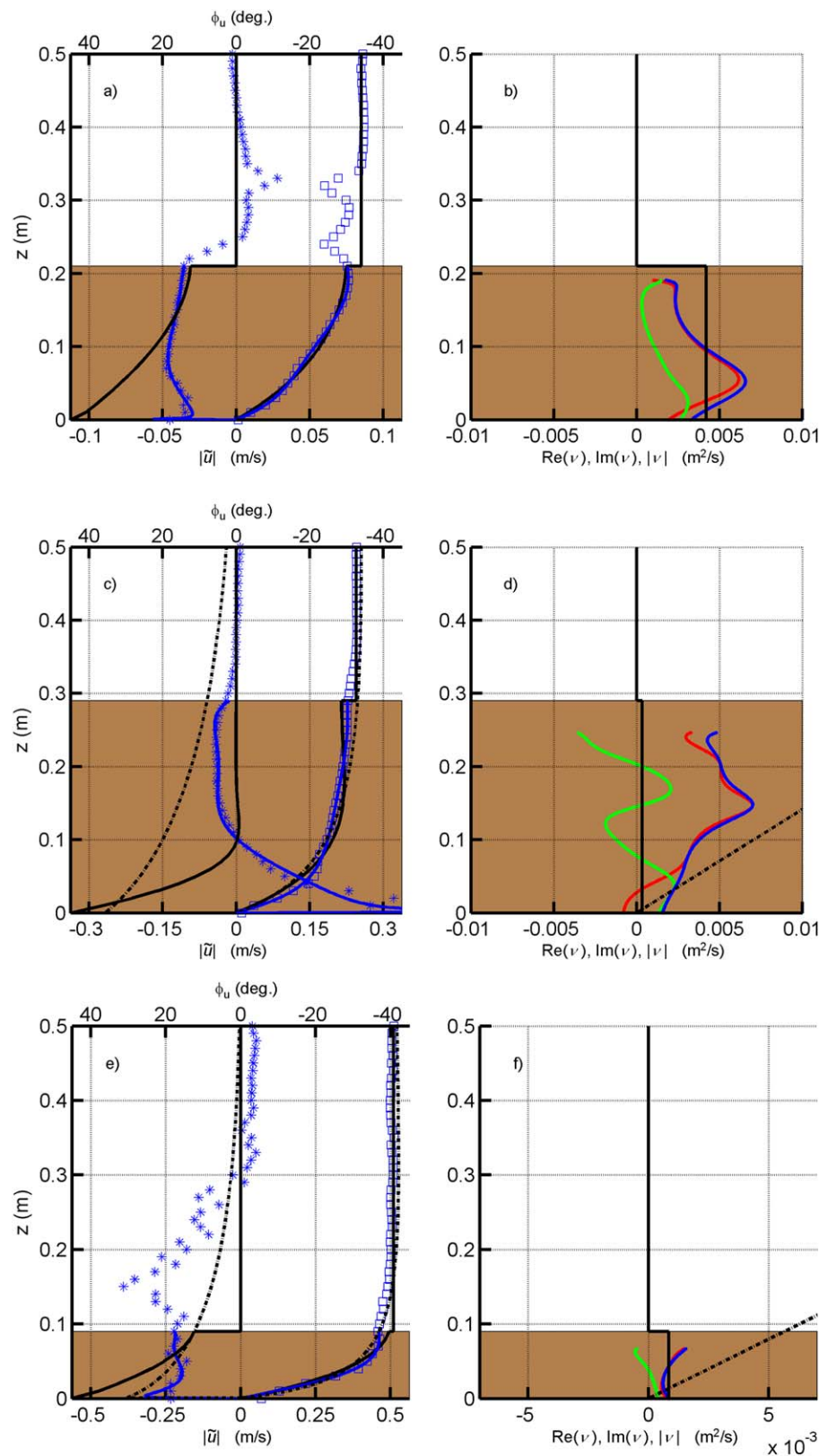
Figure 11. Vertical profiles of (a and b) laminar, (c and d) transitional, and (e and f) turbulent flow fluid-mud layer properties. Left plots (a, c, and e) show measurements of orbital velocity amplitude ($|\tilde{u}_m|$, squares, and lower x axis) and phase (ϕ_u, asterisks, and upper x axis). Solid blue lines are fifth-order polynomial fits to measurements, and solid black lines are two-layer model best fit solutions. Right plots (b, d, and f) show the magnitude (blue) real part (red) and imaginary part (green) of the ν calculated from equation (13).

Figure 12. Time-depth color plot of laminar flow fluid-mud layer properties from *yd* 80:14. (a) PCADP Backscattered Intensity from the 20° off vertical beam, the lutocline from the 20° beam (dash-dot), the lutocline from the vertical beam (solid) and the stationary seabed (dash). (b) Horizontal velocity with the same lutocline and stationary bed locations as Figure 12a and the range bins for spectra shown in Figure 10 in the fluid-mud layer (red) and water layer (blue). (c) Vertical velocity.
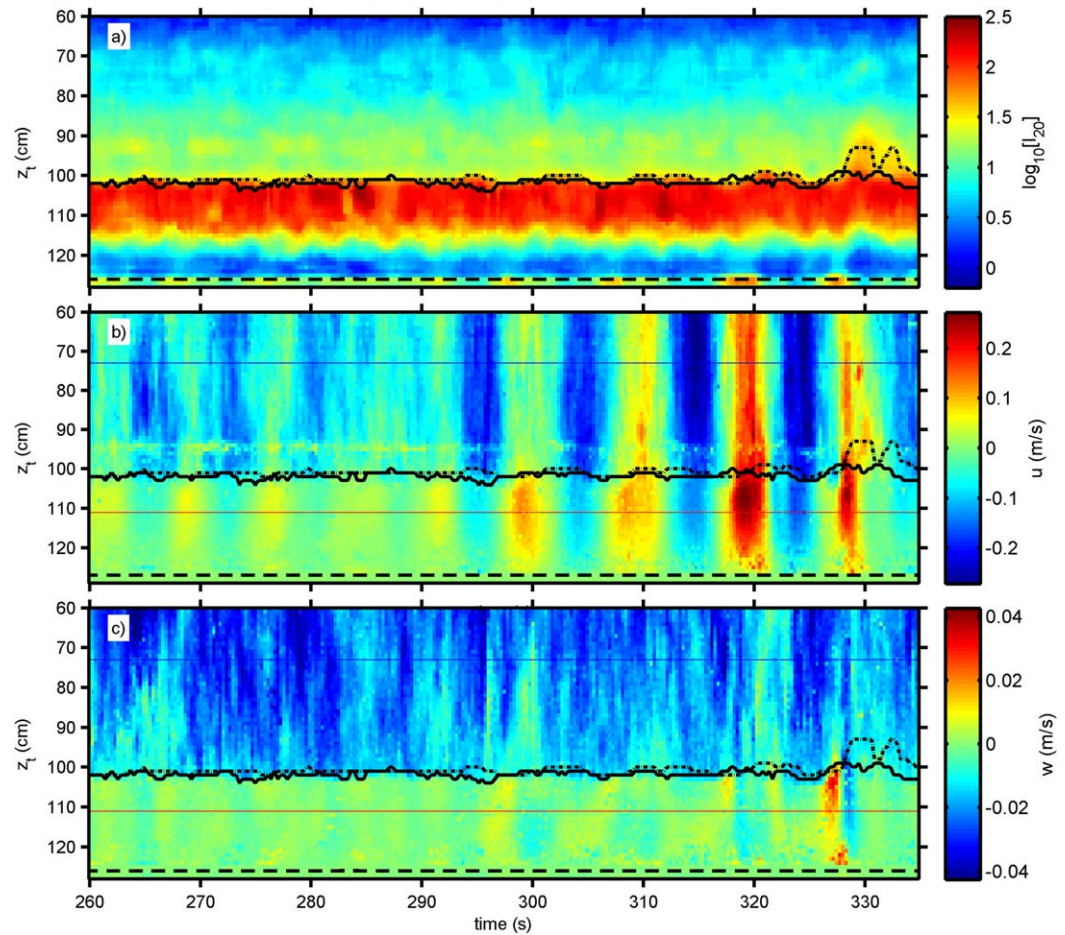
transducer, and α_2 is assumed to be zero. While the difference between α_1 and the other sensors angles was known to be 20° due to the rigid mounting of the transducers on the frame, the frame may have titled slightly as it settled into the seafloor, and seafloor slopes due to bedforms may vary across the array.

Because the horizontal velocities calculations combine measurements from two divergent beams, with sampling volume separations larger than typical turbulence scales in the wave boundary layer, and the vertical velocity is calculated from a single sampling volume, the vertical velocity is primarily used to characterize turbulent fluctuations. Estimates of anisotropy can performed by examining the variance of the along-beam turbulent velocities from the angled beam

$$\overline{b'^2_1}=\overline{u'^2_1}\sin^2(\alpha_1)+2\overline{u'_1w'_1}\sin(\alpha_1)\cos(\alpha_1)+\overline{w'^2_1}\cos^2(\alpha_1). \tag{30}$$

where w'_i is calculated by (19). Unlike sonars with multiple-angled beams (e.g., ADCPs), with the single-angled beam system here, there are not two independent measurements with contributions from $\overline{u'_iw'_i}$ with opposing sign that can be used to estimate $\overline{u'w'}$ by subtracting the along-beam variances. However, assuming horizontally homogenous turbulence, we can estimate the magnitude of the sum of the two terms $\overline{u'^2_1}\sin^2(\alpha_1)+2\overline{u'_1w'_1}\sin(\alpha_1)\cos(\alpha_1)$ as $\overline{b'^2_1}-\overline{w'^2_2}\cos^2(\alpha_1)$. Furthermore, using an approximate relation between $\overline{u'_1w'_1}$ and $\overline{w'^2_2}$ (e.g., $\overline{u'_1w'_1}=-2\overline{w'^2_2}$) allows estimation of $\overline{u'^2_1}$ and anisotropy defined as:

$$A_N=\left(\overline{u'^2_1}/\overline{w'^2_2}\right)^{1/2}. \tag{31}$$

Depth-dependent horizontal (S_{uu}) and vertical (S_{ww}) velocity spectra and variances from the PCADPs were calculated with 50% overlapping 147 s Hanning windows, resulting in averaging 12 spectra over the 16.9 min burst. Depth-dependent representative velocity profiles ($\tilde{u}$ and $\tilde{w}$) were calculated in a similar manner to equation (26). Depth-dependent cospectra between $u(z)$ and $u(z = 50$ cm$)$ were calculated to estimate the phase shift (ϕ_u) of the orbital velocities within the fluid-mud layer relative to the overlying water.

The fluid-mud layer thickness, wavelength, and height of the internal mode lutocline waves and characteristics of bedforms were measured from the PCADP data with a combination of backscatter and velocity data with a conceptually similar method to that described in *Jaramillo et al.* [2009]. The amplitude of the internal waves ($\tilde{a}_{0int}$) was calculated from the PCADP backscatter profiles in a similar manner to the ABS data analysis. The lutocline location was found from the first peak of the backscatter profiles. The location of the seafloor was found both from the second peak of the backscatter profiles ($\eta_{b,i}$ for the ith array element), and the level of no motion from the velocity profiles was also used to estimate bed location. For burst-averaged data, the level of no motion was calculated by finding the elevation ($\eta_{nm,i}$) defined by $\tilde{w} < 2$ mm/s, which is close to the noise floor of the sensor. To perform this analysis on a wave resolving time scale, the level of no motion was found under the maximum onshore and offshore velocity, and interpolated at times in between. This eliminated problems associated with the level of no motion becoming high above the bed at the wave velocity zero crossing. In addition to using the bed elevation and lutocline level to estimate the fluid-mud layer thickness, the bed elevation analysis technique was also used to examine bedform mobility.

In order to measure the wavelength of the internal waves, the spatial structure of the vertical velocity along the array was processed using well-established spatial array processing techniques [*Burdic*, 1991; *Capon*, 1969]. Since the maximum vertical velocities due to internal waves are expected to occur at the lutocline, a velocity measurement from the ith array transducer just below the lutocline ($w_{0m,i}$) was calculated by averaging three bins of vertical velocity centered on a range bin 5 cm below the trough level ($h_m - \tilde{a}_{1m}$). A data cross-covariance matrix (C_{ij}) with elements from the i and jth array elements is formed by

$$C_{ij}(\tau) = \frac{1}{N_b} \sum_{k=0}^{N_b} \frac{1}{T} \int_{kT/2}^{(k+2)T/2} \widehat{w}_{0m,i}(t)\widehat{w}_{0m,l}(t-\tau) \quad dt \ , \tag{32}$$

where $\widehat{w}_{0m,i}$ indicates a detrended, band-pass filtered ($f_l < f < f_u$) and Hanning windowed $w_{0m,i}$. Due to the rapid temporal sampling and coarse spatial sampling, a summation notation is used in the spatial domain, and integral notation is used in the temporal domain. The time window for estimating the covariance was $T = 72$ s and $N_b = 26$ half overlapping blocks were averaged in each 16.5 min PCADP data burst. A model vector based on internal waves traveling in either direction in the range $-2.5\pi < k < 2.5\pi$ is defined as $d_k = e^{-ikx_k}$. The range of wave numbers is limited by the Nyquist wave number for the array of 2.5 cyc/m based on a minimum sensor separation of 0.4 m. The power spectra of the vertical velocity as a function of horizontal wave number is then estimated from the zero temporal lag covariance matrix as:

$$P_{ww}(k) = \frac{\left[\mathbf{d}^H \mathbf{C}^{-1} \mathbf{d}\right]^{-1}}{N}, \tag{33}$$

where $\mathbf{d}^H$ is the complex conjugate transpose (Hermitian) of $\mathbf{d}$, and $N = 4$ is the number of array elements. The lagged cross correlation is defined as

$$R_{ij}(\tau) = \frac{C_{ij}(\tau)}{\sqrt{|C_{ii}(0)C_{jj}(0)|}}. \tag{34}$$

The correlation matrix at the lag which maximizes the correlation for each combination of i,j is referred to as $R_{ij}(\tau_{max})$.

4. Results and Discussion

4.1. Site and Sediment Input

The field observations were conducted in the spring of 2008 on the Louisiana shelf 125 km to the west of the mouth of the Atchafalaya River (Figure 4). During the spring runoff peak, which typically takes place in March and April, fine sediment is advected out of Atchafalaya Bay and deposits on the seafloor in the

vicinity of the study site [*Allison et al.*, 2000; *Draut et al.*, 2005]. In spring of 2008, Atchafalaya River discharge measured at Simmesport, LA [*USACE*, 2012] was approximately double the 1930–2007 average. During winter and early spring, energetic cold fronts pass this area creating waves of 2–3 m height on the outer shelf on a weekly to biweekly interval (Figure 6). *Kineke et al.* [2006] describe the details of the cross-shore suspended-sediment advection by mean currents in response to the cold fronts in this region. The study site was located 15 km west of Trinity Shoals so wave refraction and shadowing from the shoals would not cause substantial alongshore gradients of wave energy in the vicinity of the study area. The isobaths in the study area were approximately shore parallel. The study area is located on the western edge of a 20 km section of accreting mud flats [*Draut et al.*, 2005].

Instrumentation was deployed for a 57 day period between 13 February 2008 (*yd* 44) and 10 April 2008 (*yd* 101) with a recovery and redeployment operation on 15 and 16 March (*yd* 72 and 73) to retrieve refresh batteries and clean biofouling. The 30 day period starting 1 March (*yd* 61) is used for much of the analysis as the pulse of new sediment from the Atchafalaya River appeared at the study site on *yd* 63, and three energetic wave events occurred during this 30 day period.

4.2. Wind Forcing and Wave Response

Starting in early March, winds associated with three atmospheric cold fronts produced wave events with significant wave height over 1.5 m (Figure 6, labeled 1, 2, and 3). Prefrontal frontal winds are typically from the East to Southeast, with velocities around 10 m/s and veer through Southwest to Northwest as the front passes the study area (Figure 6d). Peak wind velocities associated with the frontal passage were typically 10–13 m/s. In response to the wind forcing associated with the fronts, waves built to a maximum height (H_{m0}) of 1.2–1.8 m at the 9 m isobath site (Figure 6a). The spectral energy of waves typically had a peak between 0.10 and 0.15 Hz (wave periods of $T_p = 7$ to 10 s), and 75% of the energy was usually contained within the swell band used for analysis ($f_u < f < f_l$), although during certain periods there was more high-frequency energy (Figure 6b). The high-frequency energy (sea band with $f > 0.25$ Hz) was locally forced and follows the wind direction, while the low-frequency energy was generated offshore and propagates perpendicular to the isobaths with directions near 180° (Figure 6c) due to offshore refraction.

4.3. Seafloor Response to Wave Forcing

In response to the elevated near-bed wave orbital motions caused by three wave events and higher velocity currents associated with the wind forcing, sediment was resuspended through the lower portion of the water column during each of the events. This can be seen in the ABS data as periods with vertically constant backscattered intensity above the lutocline (Figures 7 and 8). During resuspension events in which the OBS remained 10–20 cm above the lutocline or seafloor, suspended sediment concentrations ranged from 1 to 10 g/L (low concentration). During the high wave events (labeled 1, 2, and 3), a fluid-mud layer forms below the low-concentration suspension. During periods in which the OBS sensor was near or below the lutocline (e.g., *yd* 64, 68, and 80–84), the sediment concentrations approach the sensor calibration maxima of 60 g/L. Once the OBS sensor is below the lutocline, the signal on both detectors of the OBS is below the minimum threshold of detection due the strong optical attenuation of the high-concentration fluid mud of over 60 g/L. ABS data in the same range bin as the OBS show a similar temporal structure. Box cores taken at the 7 m site during the turn-around cruise on *yd* 73 revealed 2–8 cm thick recently deposited mud layers with bulk densities of approximately 1200–1300 kg/m^3. From visual examination of the box cores under nonforced conditions (e.g., no pressure gradients due to waves), this layer had gelled and did not flow freely as a fluid. The cores also indicate a consolidated layer below the recently deposited surface layer with a bulk density of around 1500 kg/m^3 consists of clay and silt layers, with some shell hash, but does not contain significant amounts of sand. A cross-shelf bathymetric survey using a dual-frequency echo sounder (50 and 200 kHz) was conducted during relatively calm conditions on 9 March 2008 (*yd* 69). The survey revealed a near-constant difference of 5 cm in depth-of-return from the two frequencies between the 9 and 7 m sites thinning to 0 cm at the 5 m site. The difference in depth of return indicates an unconsolidated mud layer.

After the peak of each wave event, during conditions with decreasing wave height, the suspension settled to produce fluid-mud layers with approximately 15–30 cm thickness at the 5 m (Figures 7d and 7f), and 7 m (Figure 9, PCADP data) sites. After formation, these fluid-mud layers typically decrease in thickness to 50% of their original thickness over a period of about 2 days with a lutocline settling rate of approximately
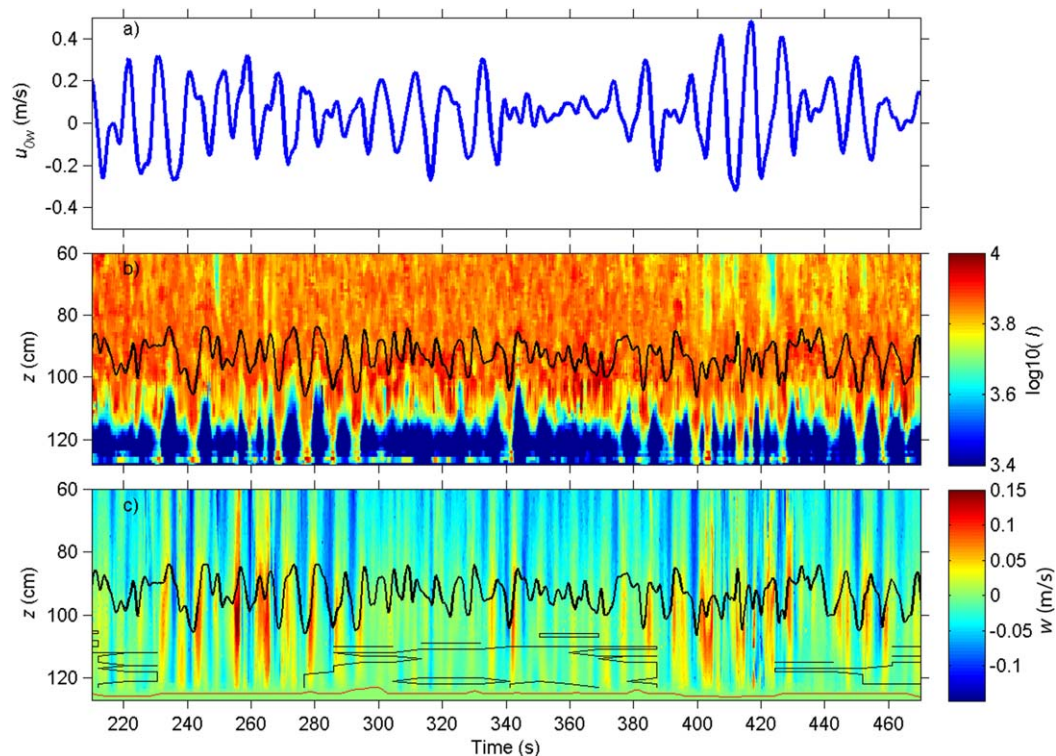
Figure 13. Transitional Fluid-Mud Layer from *yd* 80:00 h, (a) Wave orbital velocity showing wave groups. (b) Time series of vertical profiles of Backscattered Intensity showing large lutocline fluctuations with amplitude variations on the wave group time scale. The location of the stationary seafloor as defined by the level of no motion is shown as a red line. (c) Vertical velocity with the periods of low turbulent energy ($S_{ww} < 20$ %) enclosed in black contours. These generally occur between wave groups.

5 cm/d. This period of fluid-mud layer thickness reduction is referred to as the settling period. At the 9 m site, there is considerably less formation of fluid mud after wave events with elevation changes of 10 cm or less (Figure 7f). After the peak of the wave events, during the periods with settling fluid-mud layers, the suspended sediment concentration above the lutocline is very low (less than 1 g/L) and concentrations under the lutocline are greater than 60 g/L based on OBS data. This sequence of events is roughly consistent with that described by *Sahin et al.* [2012] for a location in Atchafalaya Bay. Based on the increase in acoustic attenuation as the stationary bed return becomes weaker, this decrease in thickness of the fluid-mud layer is interpreted as an increase in concentration. Analysis of PCADP data in section 4.4 shows that the fluid-mud layers at the 7 m site are mobile in response to wave forcing for a period of 36 h after the peak of the wave event 3, thus consist of *mobile* fluid mud during the settling period. Unfortunately, the PCADP had a setup error and only recorded data for the first 6 days of each deployment, thus only captured 2 days of data after wave event 3, and did not capture wave events 1 and 2. In events 1 and 2, after 2 days of settling, subsequent wave events eroded the recently deposited mud layer. In event 3, there were no waves larger than 1 m until 6 days after the event indicating a more persistent fluid-mud layer.

During the high wave events, when sediment was suspended throughout the lower portion of the water column, the lutocline showed large internal mode elevation fluctuations (Figure 13) with internal mode wave amplitudes ($\tilde{a}_{0int}$) of up to 8 cm at the 5 m site and 5 cm at the 9 m site, again suggesting mobile fluid mud. As the wave orbital and mean current velocities decrease toward the end of the wave events, the suspension settles out of the water column and the internal wave amplitude $\tilde{a}_{0int}$ decreases to 1–2 cm, indicating that the fluid mud is still mobile with small motions. In event 3, after the 2 day period of settling, fluctuations are visible on the lutocline with typical $\tilde{a}_{0int}$ of 1 cm at the 5 m site, consistent with the observation at the 7 m site of a mobile fluid-mud layer at during this period. At the 5 m site, after the 2 day period of settling, $\tilde{a}_{0int}$ decreases below the 0.5 cm resolution of the sensor indicating the fluid mud may have become stationary. At the 9 m site, the fluid-mud layers also have longer periods with small fluctuations ($\tilde{a}_{0int}$ less than the 0.5 cm resolution of the sensor) due to the weaker wave forcing in deeper water, and might consist of

greater periods of stationary fluid mud. The box cores were taken 5 days after event 2 during a period that is transitioning from a fluid-mud layer to a stationary mud layer. In event 2, the fluid-mud layer was mobile with $\tilde{a}_{0int} = 4$ cm, but during the smaller wave peak, $\tilde{a}_{0int}$ was only 0.5 cm indicating there was a period of several days between the time of the box core collection and mobility of the fluid-mud layer.

Although the details of large-scale transport processes that result in the formation of the fluid layers are beyond the scope of this paper, the fluid-mud layers must consist partially of new sediment from the Atchafalaya. Fluid-mud layers are not present in the ABS data from *yd* 45 to *yd* 63, before the increased spring runoff of the Atchafalaya River despite similar wave events with H_{m0} at the 9 m site of approximately 2 m during this early period. During the second and third fluid-mud events shown in Figure 7, some of the sediment in the fluid-mud layer probably consists of resuspension of sediment deposited from the first fluid-mud event, but the ratio of newly delivered Atchafalaya sediment to resuspended sediment is unknown. Mean currents just above the fluid-mud layer or just above seabed if no fluid-mud layers are present ($\bar{u}_{w0}$ in Figure 7c) are directed toward the west before the fluid-mud events, presumably advecting suspended sediment from Atchafalaya Bay to the study site. *Kineke et al.* [2006] provide a more thorough discussion of the large-scale transport processes in this area, though these transport observations were restricted to 20 cm and higher in the water column.

4.4. Wave Energy Flux Attenuation

In response to the temporally variable seafloor fluid-mud layer characteristics, wave energy flux attenuation ($\kappa = F_x/F$) and the flux divergence (F_x) also vary dramatically. Background values of κ when recently deposited fluid-mud layers were not present were 0.088 ± 0.022 km^{-1} (mean $\pm$ one standard deviation with averaging interval shown by black lines in Figure 8d), indicating the waves take 12 km to decrease to 37% ($\exp(1)^{-1}$) of their original energy flux.

The flux divergence is largest during the high wave events because the most energy is available during these periods. Maximum flux divergences between the 9 and 5 m sites ($F_{x9,5}$) in the three labeled high wave energy events are 1.0, 0.67, and 1.2 W/m^2. The flux divergences for the onshore portion of the array ($F_{x7,5}$) were approximately a factor of 2 greater than $F_{x9,5}$ during the first two events and almost equal to $F_{x9,5}$ during the third event. The flux divergences for the offshore portion of the array ($F_{x9,7}$) were approximately a factor of two less than $F_{x9,5}$ during the first event, slightly negative during the second event (indicating wind input was slightly larger than dissipation in this region) and slightly greater than $F_{x9,5}$ during the third event.

During the periods of high wave energy, maximum values of $\kappa_{9,5}$ are 0.19, 0.14, and 0.09 km^{-1}, which are 1.5 times the background values of $\kappa = 0.09$ km^{-1}, and one-third of the maximum κ values, which occur after the high energy periods. These values of κ result in decay scales of 7–10 km, which are still relatively large compared to the across-shelf length scale of 4 km (defined by the distance from the 7 m isobath to the shore). During the peak of the most energetic wave event (labeled 3), wave height decreased from 2.1 m at the 9 m isobath to 1.9 m at the 5 m isobath. During periods of high wave energy, the spatial variations in κ are similar to the spatial variations in flux divergence, with the values of $\kappa_{7,5}$ for the onshore segment of the array being larger than $\kappa_{9,5}$ during events 1 and 2 and about equal for event 3. In the offshore segment of the array, $\kappa_{9,7}$ is much smaller than $\kappa_{9,5}$ or even negative for event 2.

Immediately after resuspension and deposition events, during periods with settling mobile fluid-mud layers, $\kappa_{9,5}$ increases by a factor of 2–3 from the high energy values to a peak values of 0.32, 0.26, and 0.37 km^{-1}. This results in decay scales as short as 2.6 km, which is significantly less than background levels of 12 km. However, the waves during these periods are quite small with typical H_{m0} of 0.40 m at the 9 m isobath and 0.25 m at the 5 m isobath. Thus, the total energy flux divergence during the periods with maximum κ is also quite low with values of $F_{x9,5} = 0.13$, 0.06, and 0.07 W m^{-2}. During periods of high κ, the attenuation occurs predominantly in the onshore segment of the array. The values of $\kappa_{7,5}$ during these periods are consistently a factor of 2 greater than $\kappa_{9,5}$ with peak values of $\kappa_{7,5}$ around 0.7 km^{-1}. The attenuation in the offshore portion of the array is smaller with values of $\kappa_{9,7} = 0$ to 0.2 km^{-1}.

To compare these wave energy flux divergence measurements to values from sandy seabed environments, the wave energy-dissipation friction factor ($f_{e,Fx}$) calculated using flux divergences (3) was compared to local estimates of the wave friction factor $f_{w,N}$ based on the *Nielsen* [1992] formula

$$f_{w,N} = \exp\left[5.5(r/A)^{0.2} - 6.3\right]. \tag{35}$$

Here A is the near-bed wave orbital motion semiexcursion defined by $A = \tilde{u}_{w0}/2\pi f_{0w}$, and r is the hydraulic roughness. This formula has been shown to produce reasonable fits to laboratory data over a wide range of r/A ($0.001 < r/A < 1$) in the fully developed rough turbulent flow regime [*Nielsen*, 1992]. Using $r = 2.5$ cm (magenta line in Figures 8e and Figure 9g) allows $f_{w,N}$ to match the $f_{e,Fx}$ calculated from flux divergences between the 9 and 5 m sites during background conditions and during periods of high wave energy (i.e., $\kappa < 0.2$ km^{-1}). Most of the low-frequency variations (time scales greater than 1 day) in $f_{e,Fx}$ during these background and high-energy periods can be explained by variations in A and do not require invoking variations in mud-related dissipation processes. During the settling mobile fluid-mud periods (high κ) using a $r = 2.5$ cm produces estimates of $f_{w,N}$ that are less than the observed $f_{e,Fx}$ values by a factor of 3–5, consistent with the increase of κ during these periods. Thus, in order to fit $f_{w,N}$ to $f_{e,Fx}$ during the settling mobile fluid-mud periods, an r of 10 cm would be required for the entire cross-shelf array or an r of 15 cm for the onshore segment. In sandy environments with ripples, *Nielsen* [1981] suggests $r = C_N \eta_r^2/\lambda$, where λ is the ripple wavelength, η_r is the ripple height, and C_N is an empirical coefficient. *Hay* [2008] suggests that C_N varies from about 6 for equilibrium ripples to 1 for ripples that have degraded due to biological reworking processes. The steepness (η_r/λ) of equilibrium orbital ripples is typically around 0.15 [*Traykovski*, 2007]. *Hay* [2008] observed steepness of 0.10–0.05 for degraded ripples. In order to produce an r of 2.5 cm consistent with the background and high energy conditions observed in this study, a physical roughness height (η_r) would range from 50 cm ($\eta_r/\lambda = .05$, $C_N = 1$) to 5 cm ($\eta_r/\lambda = .1$, $C_N = 5$). The lower end of this range is consistent with a sandy bed with large ripples, but is rougher than physical roughness scales that are expected on a muddy seafloor as typical values of 0.005–1 cm are used in modeling studies[*Harris and Wiberg*, 2001; *Wiberg and Harris*, 1994]. In contrast to the low values of roughness of muddy beds that have been used in the literature, the measurements (section 4.7.2) suggest large bedforms may be present here. However, it is not clear that they are as steep or sharp crested as ripples found in sandy environments. For the cases with settling mobile fluid-mud layers and high κ (equivalent r of 10 cm), the physical roughness height would be at minimum 20 cm or greater depending the choice of C_N, which is higher than typical ripple heights observed on sandy seabeds and larger than the observed bedforms at the 7 m site.

In summary, during high-energy conditions, the measured wave energy flux divergence as parameterized by $f_{e,Fx}$ could be consistent with previous estimates of turbulent dissipation over a rippled bed as calculated using the *Nielsen* [1992] friction factor, although the required hydrodynamic roughness is slightly higher than would be anticipated on a muddy seafloor. During the settling mobile fluid-mud periods, the wave energy flux divergence with $f_{e,Fx}$ values of 1–2 is much greater than any reasonable estimates of turbulent dissipation over a rippled bed.

4.5. Fluid-Mud Layer Flow Characteristics and Energy-Dissipation Mechanisms

The profiles of horizontal and vertical velocity from the PCADP at the 7 m depth site provide a unique data set to examine the mechanisms in the fluid-mud layer that dissipate wave energy (Figure 9). The remainder of the analysis is focused on the storm and subsequent laminar fluid-mud layer formation event that occurred from *yd* 79 to *yd* 80:18, after which the PCADP stopped recording data. The data show two distinct sets of processes during the high F_x, low κ period and high κ, low F_x period.

Before 79:18, the flow within the fluid-mud layer is turbulent, with high turbulent dissipations rates ($10^{-3} > \varepsilon_t > 10^{-4}$ W/kg) within the fluid-mud layer (Figure 9f) as calculated by the inertial dissipation method (16). Estimates of turbulence such as $f_{w,w'}$ and $f_{w,N}$, calculated with a roughness of $r = 2.5$ cm agree well with $f_{w,N}$. However, the $f_{w,w'}$ turbulent dissipation estimate is over an order of magnitude less than either $f_{e,Fx}$, $f_{w,w'}$, or $f_{w,N}$ (Figure 9g). A well-defined lutocline is visible in acoustic backscatter data, but the concentrations are low enough for the 1.0 MHz acoustic energy to have low attenuation, so that high backscatter is measured both within the fluid-mud layer and the stationary seafloor. During this period, before 79:18, flux divergence (F_x) is high and the attenuation rate (κ) is low. Wave orbital velocities near the lutocline are above 0.2 m/s, with a maximum of 0.50 m/s, in both the fluid-mud layer ($\tilde{u}_{0m}$) and the overlying water ($\tilde{u}_{0w}$). There is a slight reduction of $\tilde{u}_0$ from the water to the mud with the mean over this period of $(\tilde{u}_{0w} - \tilde{u}_{0m})/\tilde{u}_{0w} = 0.18$. The phase shift ($\phi_u$) of $\tilde{u}_{0m}$ relative to $\tilde{u}_{0w}$ is small and variable, with a mean over the period close to $0°$. Internal mode oscillations on the lutocline are large ($\tilde{a}_0 \sim 6$ cm) during this period.

The vertical structure of the mean velocity ($\bar{u}$) during this period shows large shear at the lutocline, up to 30 cm/s over 20 cm, with the wind, tidal, or other large-scale pressure gradient forced currents visible in water decoupled from the mean velocity in the fluid mud. In fact, from yearday 79:04 to 80:03 an offshore mean flow of 0.05–0.08 m/s is present in the fluid-mud layer (Figure 9e). This near-bed downslope flow, decoupled from the flow above the lutocline, during a period of high suspended sediment concentration is consistent with a wave-supported sediment gravity flows (also referred to as wave-supported turbidity flows) as observed in other environments by *Traykovski et al.* [2000, 2007] and is discussed in further detail in section 4.6.

On yearday 80:00, as $\tilde{u}_{0w}$ and $\tilde{u}_{0m}$ decrease below 0.20 m/s, the flow enters a transitional stage from turbulent to laminar. The turbulent dissipation rate begins to decrease from $\varepsilon_t = 10^{-4}$ to 10^{-5} W/kg. The estimates of turbulence $f_{w,w'}$ and $f_{w,N}$ both begin to fall below $f_{e,Fx}$ during the transitional period as the dissipation begins to be dominated by laminar processes. The turbulent friction factor ($f_{e,IDM}$), calculated from the inertial dissipation method, begins to increase from *yd* 79:16 to 79:19 due the decreasing $\tilde{u}_{0w}$, but is still an order of magnitude less than either $f_{e,Fx}$, $f_{w,w'}$, or $f_{w,N}$ (Figure 9g). Internal mode oscillations on the lutocline remain large at $\tilde{a}_0 \sim 5$ cm during the beginning of the transitional period and then decrease toward the end of this period after *yd* 80:00. The region of decreased backscatter within 10 cm of the bed (Figure 9a) indicates that the acoustic attenuation is beginning to increase due to the increasing fluid-mud layer sediment concentration. A well-defined return from the stationary seafloor at 122 cm is still visible. During this transitional period, flux divergence (F_x) is decreasing and the attenuation rate (κ) is increasing (Figure 9b). The phase (ϕ_u) shows a complex vertical structure with a lead of 5 to 8° at the top of the fluid-mud layer and lags of 15 to 20° near the bed (Figure 9d). The mean velocity during the transitional period still shows a wave-supported downslope turbidity flow until day 80:03 (Figure 9e).

After yearday 80:03, the flow enters the laminar stage with low turbulent dissipation estimates ($\varepsilon_t < 10^{-6}$) in the interior of the fluid-mud layer, that are the minimum measurable due the noise floor of the sensor. Near the seafloor and the lutocline, turbulent dissipation is slightly larger ($10^{-5} > \varepsilon_t > 10^{-6}$ W/kg). During this period, the acoustic attenuation due to the increasing fluid-mud layer sediment concentration increases as indicated by the stationary bed return that is significantly reduced compared to the turbulent and transitional period. The wave-attenuation rate ($\kappa_{9,5}$) increases to its maximum of 0.38 km^{-1} on yearday 82:00 (Figure 8). The wave orbital velocities are low during this period with $\tilde{u}_{0w}$ and $\tilde{u}_{0m}$ less than 0.15 m/s. The shear in the wave velocity across the lutocline decreases slightly to $|(\tilde{u}_{0w} - \tilde{u}_{0m})/\tilde{u}_{0w}| = 0.13$. During the laminar flow period, ϕ begins to show a well-defined and consistent lead of 15°–20° in the fluid-mud layer. Although there are oscillatory orbital velocities of approximately 10 cm/s in the fluid-mud layer, the mean flow is very weak within the fluid-mud layer despite relatively strong mean flows of up to 20 cm/s in the overlying water. On yearday 80:10, the internal mode oscillations on the lutocline decrease from $\tilde{a}_0 \sim 3$ cm to less than 1 cm.

In the next sections, to further examine dissipation mechanisms within the laminar, transitional, and turbulent flow regimes, individual 15 min data bursts were selected from each regime on *yd* 79:06 (turbulent), 80:00 (transitional), and 80:16 (laminar). The classification of the periods into laminar, transitional, and turbulent flow is based on the characteristics of the velocity spectra within the fluid-mud layer. The wave-supported turbidity flows are also examined to determine if the dynamics of the mean flows are sustainably different from the oscillatory flows. Finally, the internal mode wave observations and energetics relative to the external mode waves are examined. Figure 10 shows spectra of vertical and horizontal velocity both in the fluid-mud layer and in the overlying water for all three periods. Figure 11 shows vertical profiles of wave orbital velocity amplitude ($|\tilde{u}|$) and phase (arg ($\tilde{u}$)) through the water and fluid-mud layer, along with two-layer model (equation (11)) fits to the profiles, and estimates of v for all three periods. Figures 12, 13, and 14 show time series of velocity and backscattered intensity profiles for the laminar, transitional, and turbulent period, respectively.

4.5.1. Laminar Flow Regime

As wave energy decreases toward the end of a wave event (Figure 9, vertical line C) and the fluid-mud layer viscosity increases, the flow in the fluid-mud layer becomes laminar. The primary evidence for this is the variation of the vertical structure of horizontal and vertical velocity fluctuations from the fluid-mud layer ($z_t = 111$ cm) to the overlying water ($z_t = 73$ cm), (Figure 12). S_{uu} (Figure 10a) and S_{ww} (Figure 10b) in the water show a peak associated with orbital velocities at $f = 0.1$ Hz and then a decay proportional to $f^{-5/3}$
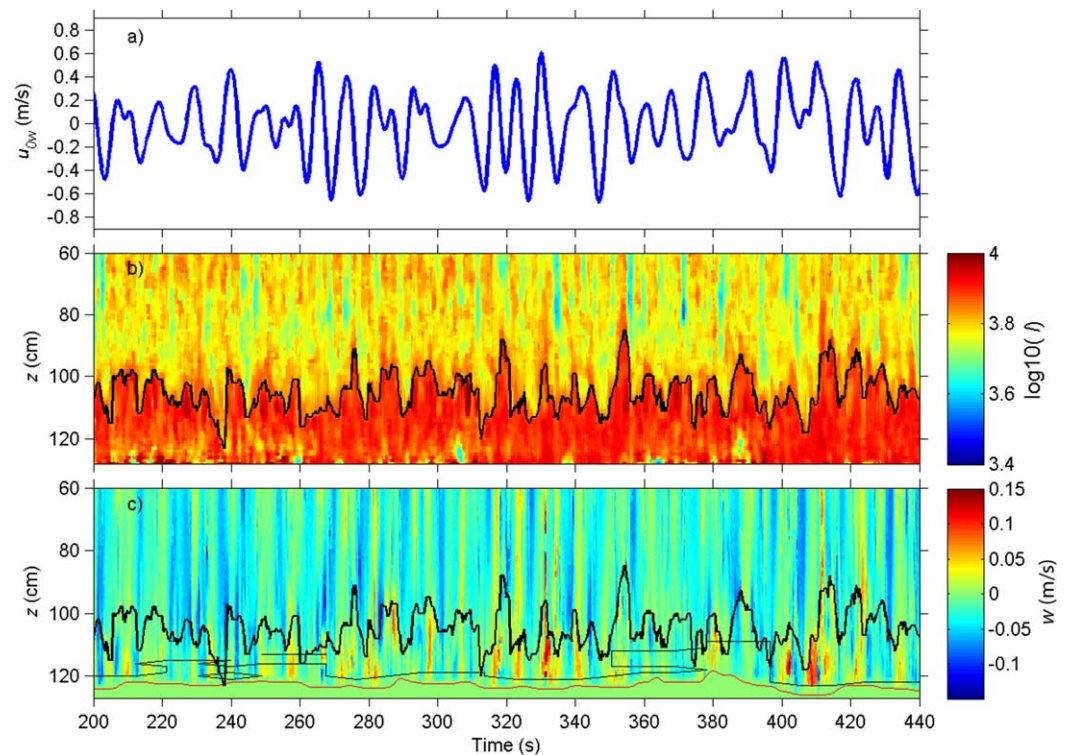
Figure 14. Turbulent Fluid-Mud Layer from *yd* 79:06, (a) wave orbital velocity showing wave groups. (b) Time series of vertical profiles of Backscattered Intensity showing large lutocline fluctuations with amplitude variations on the wave group time scale. The location of the stationary seafloor as defined by the level of no motion is shown as a red line. (c) Vertical velocity with the periods of low turbulent energy ($S_{ww} < 20\%$) enclosed in black contours. These generally occur between wave groups.

above 0.15 Hz until the Nyquist sampling frequency of 1.7 Hz, consistent with a well-defined inertial sub-range and turbulent flow. The spectra of horizontal velocity (S_{uu}) show nearly equal magnitudes in the wave band (0.05 Hz $> f >$ 0.20 Hz) in both the water and fluid mud. Within the fluid-mud layer, S_{ww} has three peaks in the frequency band from $0.07 < f < 0.6$ Hz, which are associated with the surface and internal mode waves. The two high-frequency peaks in this band are harmonics of the primary peak at 0.1 Hz due to the nonlinear shape of the internal mode oscillations. At frequencies above 0.3 Hz, the spectral levels of S_{ww} within the fluid-mud layer decay rapidly, and reaches the instrument noise floor of 10^{-6} m^2/s at $f = 0.6$ Hz. This rapid decay of high-frequency vertical velocity fluctuations indicates that turbulence in the fluid-mud layer is highly suppressed during this period. While accurate estimates of turbulent dissipation are not possible during this period, because the fluctuations are below the noise floor of the sensor, an upper bound on turbulent dissipation based on the inertial dissipation method is $D_{t,IDM} = 1.2 \times 10^{-4}$ W/m^2, based on a layer averaged $\varepsilon_{t,IDM} = 4.2 \times 10^{-7}$ W/kg. Either of the turbulent friction factor estimates calculated from vertical velocity fluctuations ($f_{w,w'}$ and $f_{e,IDM}$) are more than an order of magnitude less than $f_{e,F}$ calculated from surface wave energy flux divergences. Nielsen's formula produces a $f_{w,N}$ that is a factor five less than $f_{e,Fx}$, but an order of magnitude greater than $f_{w,w'}$ and $f_{e,IDM}$.

The time series of u_w and w_w profiles (Figures 12b and 12c) also shows the turbulent fluctuations in the water column and smoother velocity structure in the core of the fluid-mud layer. The time series of u_w and w_w show enhanced fluctuations near the lutocline due to internal mode waves, and enhanced fluctuations near the bed presumably due to flow over bedforms. Some of the increased velocity fluctuation variance near the bed may be due to decreased ping-to-ping correlations due to acoustic attenuation. This spatial structure is consistent with the increased interfacial and near-bed turbulent dissipation estimates shown in Figure 9f.

Vertical profiles of orbital velocity amplitude in the fluid mud ($\tilde{u}_{0m}$) and in the water ($\tilde{u}_{0w}$), calculated in the same wave band used for the flux calculations (0.05 Hz $> f >$ 0.25 Hz), show a wave boundary layer that fills

the entire fluid-mud layer (Figure 11a). The measurements of *Jaramillo et al.* [2009] also show a wave boundary layer that fills a 20 cm thick fluid-mud layer at a location closer to the Atchafalaya River mouth. The phase of $\tilde{u}_m$ leads $\tilde{u}_{0w}$ by 15° at the top of the fluid-mud layer and increases linearly to a 19° at 6 cm above the bed. The phase of the flow in the 4 cm above the bed does not continue to increase to 45° as predicted by viscous flow models, but decreases to 13°. The variability of the phase within 4 cm of the bed may be due to combination of decreased ping-to-ping correlations near the bed and actual increased flow variance due to flow over bedforms. The deficit in both the orbital velocity profile around $z = 25$ and 32 cm is due to a multiple reflection of the PCADP pings from the upper portion of the instrument mounting frame at that range. This deficit near the lutocline, combined with averaging over lutocline internal mode waves in calculating r.m.s profiles results in additional uncertainty in estimating ρ_m from velocity profile inverse calculations which are sensitive to the shear at the lutocline.

A nonlinear least squares fit was used to fit the model for a two-layer laminar flow (11) to the measured complex velocity profile using v, and ρ_m as fitting parameters, and $\rho_w = 1025$ kg/m^3, $\tilde{u}_{0w} = 9$ cm/s, $h_m = 22$ cm, and $f = 0.11$ s^{-1} as fixed parameters based on measurements. This results in $v_{fit} = 0.0042$ m^2/s ($\tilde{h}_m = 2.1$, Figure 3) with 95% confidence limits of 0.0038 and 0.0047 m^2/s, and $\rho_m = 1300$ kg/m^3 with 95% confidence limits of 1260 and 1340 kg/m^3. The actual error in the density could be larger due to errors in the velocity profile near the lutocline. The narrow confidence limit in v_{fit} relative to the possible range from 10^{-6} m^2/s for clear water to 0.01 m^2/s for highly viscous fluid mud is due to the sensitivity of the vertical structure of the velocity profile to v. In contrast, the wide confidence limits on ρ_m relative to the possible range of 1025 kg/m^3 (clear water) to 1500 kg/m^3 (fully consolidated stationary mud) is due to the approximately linear relation between the shear across the lutocline and the density ratio ρ_w/ρ_m. Based on the sharp lutocline and laminar flow in the fluid-mud layer, the two-layer approximation is valid for this case. These densities are similar to values observed by *Rogers and Holland* [2009], but higher than gel density of 1100 kg/m^3 suggested by *Sheremet et al.* [2011]. *Li et al.* [2004] report a gelling density of about 1200 kg/m^3, consistent with a proposed formula for gel concentration by *van Rijn* [2007]. The model fits the magnitude of the boundary velocity profile very well (Figure 11a), but there is a significant discrepancy between in the model predicted phase, which increases to 45° at the bed, and the observed phase which does not increase as rapidly toward the middle of the fluid-mud layer and decreases near the bed. To test the sensitivity of the fit to this anomaly in phase, the magnitude of the velocity profile was also fit to the magnitude of velocity profile from the model resulting in a similar $v = 0.0046$ m^2/s and $\rho_m = 1180$ kg/m^3.

As an alternative to these techniques which involve a model fit to estimate v, the boundary layer momentum balance (13) can be used to estimate a profile of v. While the calculated profile of v is not very sensitive to the value of the fluid-mud layer density, a value of $\rho_m = 1300$ kg/m^3 was chosen based on the two parameter model fits. In order to calculate the vertical gradients in equation (13), fifth-order polynomials were fit to the real and imaginary parts of $\tilde{u}_m(z)$. The resultant profile of v (Figure 11b) is complex valued to match both the magnitude and phase of the velocity profile, with depth averages values of $v = 0.0036 + 0.0015i$ m^2/s, similar in magnitude to the model fit of $v_{fit} = 0.0042$ m^2/s. The nonzero imaginary part of the complex viscosity profile is required to fit the phase of the observations. Nonlinear fitting of a depth-dependent density and real positive valued viscosity profiles were also explored, but did not result in significantly improved ability to match the observed phase. As suggested by *Nielsen* [1992], a complex valued profile in turbulent eddy viscosity profiles suggests the presence of more complex behavior than simple laminar flow, potentially due to either momentum advection terms, a time-dependent viscosity, or elastic mud behavior. The positive imaginary part of the viscosity near the bed indicates that the stress has a phase lead relative to the free stream velocity of less than the 45° predicted by laminar flow theory. This indicates the maximum stress occurs closer to the maximum in free stream velocity and center of the orbital displacement relative to predictions from laminar flow.

If the complex viscosity is due to elastic behavior, the decreased phase lead suggests a negative elastic modulus. Since a negative elastic modulus is generally not physically realistic, we infer that the decreased phase lead is not due to elasticity. Momentum advection on wave period time scales is likely due to presence of bedforms as discussed in section 4.7.2. The real part and magnitude of the depth-dependent viscosity profile increases from the top of the fluid-mud layer toward the core of the fluid-mud layer, perhaps suggesting a positive dependence of viscosity to increasing density within the core of the mobile fluid-mud layer. The inferred viscosity decreases near the bed, perhaps suggesting shear

thinning behavior, due to the high shear near the seafloor, which would be enhanced by the presence of bedforms.

While the choice of technique allows some freedom in the exact determination of v, either model fits or the combined momentum deficit viscous dissipation method results in a fluid-mud viscosity that is 3.5–4 orders of magnitude greater than the clear water value of 10^{-6} m²/s. Based on an assumption of constant dissipation of $v_{fit} = 0.0042$ m²/s over the fluid-mud layer, the local viscous dissipation is $\varepsilon_{fit} = 3.9 \times 10^{-4}$ W/kg. This value of the fluid mud enhanced viscosity results in a Reynolds number of $Re_A = 2.4$ or $Re_\delta = 2.2$. Using clear water viscosity results in $Re_{A,cw} = 1 \times 10^4$ or $Re_{\delta,cw} = 143$, all consistent with the suppressed turbulent fluctuations and laminar flow in the mobile fluid-mud layer. This estimate of viscosity also results in a Kolmogorov scale η_k of 0.62 m or $\eta_f = 0.14$ Hz. The location of the Kolmogorov frequency near the region of rapid spectral decay (Figure 10) is consistent with suppressed turbulence at higher frequencies and laminar flow in the fluid-mud layer. The dissipation of wave energy during the laminar flow period measured from the boundary layer data via the momentum deficit equation of $D_{md} = 0.09$ W/m² can be normalized by the flux at the 7 m site of 266 W/m² resulting in a $\kappa_{md} = 0.34$ km⁻¹. The estimate of κ from the model fit to the velocity profile has a slightly larger value of $\kappa_{fit} = 0.42$ km⁻¹. The dissipation and attenuation during this period based on the energy flux difference measured by the AWACS instruments at the 9 m site and 5 m sites are $F_{x9,5} = 0.073$ W/m² and $\kappa_{9,5} = 0.28$ km⁻¹. The estimates of D from the boundary layer measurements are consistent the flux divergence measurements from the 9 to 5 m sites (Figure 2a) within an error of 30%.

The agreement between the boundary layer measurements of dissipation with the across-shelf flux divergence estimates during the period of laminar flow in the fluid-mud layer indicates that the viscous dissipation mechanism observed in the boundary layer measurements at the 7 m site can explain the attenuation of wave energy flux from the 9 m site to the 5 m site. This agreement combined with the boundary layer observations of low turbulent dissipation indicates laminar flow viscous dissipation is the dominant attenuation mechanism during this period. Slightly larger local boundary layer estimates of κ and D at the 7 m site, compared to the flux divergence measurement that integrates over 3 km from the 9 to 5 m sites, is consistent with both the increase in κ and D by factor of 2 in the onshore segment of the array (7–5 m depths), combined with the thicker fluid-mud layers of 20–30 cm at the 5 and 7 m sites compared to the 10–15 cm at the 9 m site.

4.5.2. Transitional-Laminar Flow Regime

In between the laminar flow state observed during low energy wave conditions and the more turbulent state observed during energetic forcing there is a transitional state (Figure 9, vertical line B). During this period, the wave orbital velocities are $\tilde{u}_{0w} = 23$ cm/s with $f_{0w} = 0.12$ Hz. The internal mode waves have an amplitude of $\tilde{a}_0 = 5.2$ cm and the fluid-mud layer thickness is $h_m = 31$ cm (Figure 13a). Spectra of horizontal velocities (S_{uu}) and the velocity profile show that orbital velocities are only slightly reduced in the upper part fluid-mud layer relative to the overlying water (Figure 10c). Spectra of vertical velocity (S_{ww}) averaged over the entire fluid-mud layer show a spectral slope of slightly steeper than $f^{-5/3}$ in the region from 0.4 to 1 Hz and spectral slope close to $f^{-5/3}$ above 1 Hz (Figure 10c), suggesting the flow is turbulent during this period. The turbulent dissipation ($\varepsilon_{t,IDM}$) integrated over the fluid-mud layer for this period is $D_{t,IDM} = 0.014$ W/m² (equivalent to $\kappa = 0.005$ km⁻¹) and the flux divergence F_x from the 9 m isobath to the 5 m isobath is much larger than $D_{t,IDM}$ with values of 0.33 W/m² ($\kappa = 0.13$ km⁻¹).

Normalizing the inertial dissipation method estimate of turbulent dissipation by $\tilde{u}^3_{0w}$ results in $f_{e,IDM} = 0.00029$. The factor of 40 discrepancy between the inertial dissipation-based dissipation estimates and the flux divergence-based estimate suggests that turbulent dissipation as calculated from the inertial dissipation method is unable to account for the wave attenuation during this transitional period. The friction factors calculated from Nielsen's formula ($f_{w,N} = 0.05$), or vertical velocity variance ($f_{w,w'} = 0.0026$) are considerably larger and of the same order of magnitude as $f_{e,Fx} = 0.076$, calculated from flux divergence. These estimates of $f_{w,N}$ or $f_{w,w'}$ only become less than $f_{e,Fx}$ as the flow becomes laminar at the end of the transitional period (Figure 9f). The similar magnitudes of $f_{w,N}$ or $f_{w,w'}$ to $f_{e,Fx}$ suggests that turbulent processes may have a significant contribution to the dissipation, but that the inertial dissipation method is underestimating dissipation relative to $f_{w,N}$ or $f_{w,w'}$ based estimates. To further examine the low values of $f_{e,IDM}$, turbulent kinetic energy anisotropy (A_N) was calculated using the variances from the angled and vertical Doppler beams via equation (31). Using an assumption of turbulent stress of $\overline{u'_2 w'_2} = -2\overline{w'_2}^2$, the

resulting A_N near the top of the fluid-mud layer has a value of 4 increasing to 6 near the stationary seafloor. Using a lower assumed stress of $\overline{u'_2 w'_2} = -\overline{w'_2^2}$ results in an A_N of approximately 2.5–3 near the top of the fluid-mud layer and also increasing to 6 near the seafloor. This indicates that the turbulent fluctuations of horizontal velocity are significantly larger than the vertical fluctuations. This combined with the inertial dissipation method's cubic dependence on the velocity fluctuations could lead an order of magnitude or greater underestimates of turbulent dissipation. High anisotropy and breakdown of the inertial dissipation method is expected near a boundary and in the presence of strong density stratification [*Bluteau et al.*, 2011].

Despite the low values from the inertial dissipation method, the agreement of the other friction factors ($f_{w,N}$, $f_{w,w'}$) with the flux divergence estimates ($f_{e,Fx}$) at the beginning of transitional period and the disagreement at the end, suggests further examination of the processes that account for the wave energy dissipation during this period is warranted. Short time-window spectra (18 s versus 147 s used previously) of velocities within the fluid-mud layer were calculated and conditionally averaged. Spectra in the $f > 0.4$ Hz band with energy less than 20% of the total energy in this band were averaged separately from an average that contained spectra with all energy levels. The low energy spectral average excluded periods with turbulent bursts (Figure 13) that are typically associated with high-amplitude internal mode waves on the lutocline. The averaged spectra from the low energy periods have a shape that is similar to the shape of the spectra during the laminar flow period, with a rapid fall off of variance at 0.4 Hz and a flatter than $f^{-5/3}$ slope above 0.4 Hz (Figure 15a). This suggests that during the transitional period, the flow within the fluid-mud layer alternates between laminar flow and turbulent flow on the wave group time scale (100–150 s), with the bursts of turbulence forced by the increase of wave energy in the wave groups.

The relatively thick boundary layer measured in the velocity profiles compared to that predicted by turbulent boundary models also suggests turbulence alone cannot account for the observed dissipation, especially toward the end of the transitional period. The turbulent dissipation rate ($\varepsilon_{t,IDM}$) estimated by the inertial dissipation method or the vertical variance friction factor suggests a very thin velocity boundary layer of $\delta_{t,IDM} = 1.42 f_{e,IDM} A/2 = 0.5$ mm. Using the $\sigma_{w'}$ estimate of turbulence results in $\delta_{t,w'} = 0.67$ cm. The factor of 1.42 is used to relate the displacement thickness defined by *Kajiura* [1968] to the Stokes boundary layer thickness.

These estimates of boundary thickness are much thinner than the Stokes boundary layer thickness (δ_ν) of 8.4 cm as estimated by fitting the velocity profile with a model profile based on $\nu_{fit} = 0.0012$ m^2/s (Figure 11c). Upper and lower confidence intervals (95%) for ν_{fit} are 0.0007 and 0.0017 m^2/s. The fluid-mud layer density from the fit ($\rho_m = 1250$ kg/m^3) with confidence intervals of 1170–1340 kg/m^3 is similar to the laminar case. However, because the flow is becoming transitional and there are large fluctuations on the lutocline, the two-layer assumption is approximate and there is considerable uncertainty in density estimates in
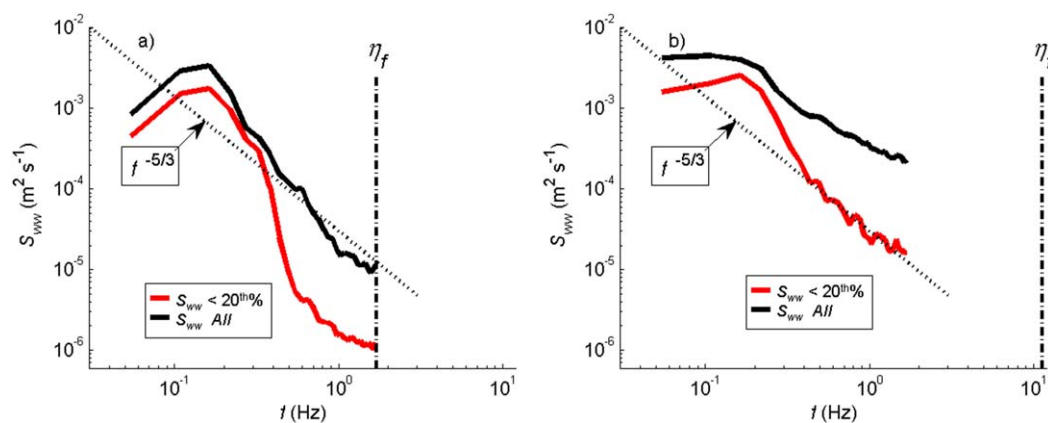
Figure 15. (a) Vertical velocity spectra (S_{ww}) averaged over the entire fluid-mud layer (black) and $S_{ww} < 20\%$ only (red) during the transitional flow period. (b) Same as Figure 15a with data from the turbulent flow period. Both plots show the Kolmogorov frequency (η_f) which is far to the right of the wave peak in Figure 15b, allowing the development of an $f^{-5/3}$ inertial subrange. In Figure 15a, the Kolmogorov frequency (η_f) is shifted to the right due to the increased mud viscosity, much closer to the wave peak, reducing the potential for fully developed turbulence.

addition to the mathematical confidence intervals calculated in the fitting procedure. Based on the optical backscatter data presented in Figure 7, the concentrations are over 60 kg/m^3. The turbulent boundary layer thickness is also considerably thinner than a boundary layer thickness based on the flux divergence of $\delta = 1.42\, f_{e}, A/2 = 1.9$ cm. The thin calculated turbulent boundary layer thickness, relative to the observed boundary layer thickness, further reinforces the conclusion that turbulent dissipation alone is insufficient to account for the observed flux divergences during this transitional period.

Dissipation of $D_{v} = 0.43$ W/m^2 ($\kappa_{fit} = 0.26$ km^{-1}) for this period was calculated using equation (14) and viscosity estimates of 0.0012 m^2/s based on fits to the velocity profile (Figure 11c). While the two-layer model is intended to model a laminar flow with constant viscosity it can also represent a turbulent flow with a vertically uniform eddy viscosity. This estimate of total viscosity should produce a reasonable upper bound for the dissipation with the caveat that the turbulent flow phase leads are generally less than those predicted by this model which increases to 45° at the seafloor.

The momentum deficit approach does not produce reliable dissipation estimates in this case due to the phase lag in the lower portion of the velocity profile balancing the phase lead in the upper portion (Figure 11c) resulting in an almost zero net dissipation in the fluid-mud layer. This complex phase behavior and the associated complex viscosity calculated from equation (13) is most likely due to the advective processes associated with the turbulent flow over bedforms, and is probably spatially variable on the bedform scale. The spatially integrated flow field would have positive dissipation. As an alternative to the constant eddy viscosity model, a linearly increasing eddy viscosity $v = \kappa u_{*} z$ with $u_{*} = 0.12$m/s was also used to fit a model velocity profile to the measurements. This shows some consistency with directly calculated viscosity profile from equation (13), which increases away from the bed in the lower portion of the fluid-mud layer, but then decreases in the upper portion. The velocity profile with the linearly increasing eddy viscosity model fits the magnitude of the measured velocity profile slightly better than the constant viscosity model, but neither captures the complex phase behavior.

While the viscosity estimate is slightly lower than that found in the fully laminar conditions, the dissipation of $D_{v} = 0.43$ W/m^2 is considerably larger due to the more energetic conditions. This boundary layer estimate of dissipation is also roughly consistent with the flux divergence estimate of $F_{x9,5} = 0.33$ W/m^2. The estimate of $v_{fit} = 0.0012$ results in $Re_{A} = 59$ or $Re_{\delta} = 10.9$ for this flow indicating that laminar effects may still be important. However, this estimate of Re_{A} assumes all of the v_{T} is due to the enhanced fluid-mud viscosity v_{m}, and thus represents and lower bound for the Reynolds number. The clear water Reynolds number for this case is $Re_{\delta,cw} = 337$, which would suggest transitional flow [*Ozdemir et al.*, 2011].

Unlike the fully laminar case where η_{f} is near the peak of the forcing, the Kolmogorov frequency, in this transitional case of $\eta_{f} = 4$ Hz is an order of magnitude greater than the upper limit of the steep fall off region of the conditionally averaged S_{ww} around 0.4 Hz. However, the viscosity and Kolmogorov spatial scale η_{k} is estimated from all periods during the data bursts, and not just the conditionally averaged low energy sections that may be more viscous. Thus, the estimates of η_{k} could be biased toward lower values, leading to a Kolmogorov frequency ($\eta_{f} = \tilde{u}_{0m} /\eta_{k}$) that is biased high. The shift of η_{f} from 0.15 Hz during the laminar period to 4 Hz during the transitional period is consistent with the shift from a spectral shape characterized by a steep fall-off above η_{f} directly to the noise floor, to a spectral shape characterized by an slope of $f^{-5/3}$ within inertial subrange region of $f_{u} < f < \eta_{f}$.

4.5.3. Turbulent Flow Regime

At the peak of the wave event, conditions appear fully turbulent in the fluid-mud layer, and wave attenuation is consistent with wave-generated turbulence estimates calculated from Nielsen's formula and the vertical velocity fluctuations. However, the inertial dissipation method estimates are still significantly lower than the other turbulence estimates. During this period, the wave orbital velocities are $\tilde{u}_{0w} = 51$ cm/s with $f_{0w} = 0.11$ Hz. The horizontal orbital velocities at the top of the fluid-mud layer are similar to the velocities in the overlying water, with weak shear in the orbital velocity profile at the lutocline (Figures 10 and 11). Similar to the transitional period, the internal waves on the lutocline are large with $\tilde{a}_{0} = 5$ cm on a fluid-mud layer of thickness $h_{m} = 10$ cm. Also similar to the transitional period, spectra of vertical velocities within the fluid-mud layer show a $f^{-5/3}$ slope above 0.4 Hz indicating turbulent flow. The presence of a region with a $f^{-5/3}$ slope is consistent with the Kolmogorov frequency of 24 Hz, which is much larger than the Nyquist sampling rate of 1.7 Hz. This indicates that the Kolmogorov microscale has become small enough to allow

full development of turbulence within the fluid-mud layer. When the same conditional sampling analysis as used in the transitional regime (section 4.4.2) is performed during this period, a rapid fall off at 0.4 Hz with a flatter than $f^{-5/3}$ spectra at higher frequencies is less pronounced than the transitional case (Figure 15b). Rather, the slope at high frequencies continues to show a $f^{-5/3}$ slope, indicating there are not periods longer than the spectral analysis window length of 18 s that have reduced turbulent fluctuations, again suggesting fully turbulent flow.

Similar to the transitional period, the dissipation due to turbulence as calculated by the inertial dissipation method ($f_{e,IDM} = 6.5 \times 10^{-4}$) is approximately a factor of 40 smaller than the flux divergences based of $f_{e,Fx} = 0.024$. Calculations of anisotropy based on assumed levels of turbulent stress of $\overline{u'_2 w'_2} = -\overline{w'_2}^2$ or $\overline{u'_2 w'_2} = -2\overline{w'_2}^2$ results in A_N values of approximately 2–3, respectively. Similar to the transitional period, this suggests that the inertial dissipation estimates of dissipation based on vertical velocity fluctuations cubed are potentially biased low by an order of magnitude. Nielsen's formula results in wave friction factor of $f_{w,N} = 0.03$ (Figure 9f) and the vertical variance method wave friction factor ($f_{w,w'} = 0.023$) are comparable to $f_{e,Fx} = 0.022$ as calculated from the flux divergence from the 9 to 5 m sites. Consistent with the mismatch in *IDM* and variance-based friction factors, the boundary layer thickness estimated from $f_{e,IDM}$ is much smaller than the observed boundary layer thickness, while the estimates from $f_{w,w'}$ or $f_{w,N}$ are more consistent with observations. The small value of $f_{e,IDM}$ results in a boundary layer thickness of $\delta_t = 1.42\, f_{e,IDM,}\, A/2 = 0.3$ mm, while the measured boundary layer thickness is 4 cm closer to $\delta_t = 1.42\, f_{e,N},\, A/2 = 1.7$ cm.

Fitting the velocity profile with the two-layer model results in a combined viscosity of $v_{fit} = 0.0009$ m^2/s (confidence intervals of 0.0007–0.001), one-third the value of the transitional period. Due to the increased turbulence at the interface, the density estimate of $\rho_m = 1170$ kg/m^3 from the inversion is not considered reliable; however, the optical backscatter data constrains the concentration estimates to be larger than 60 kg/m^3. Similar to the laminar case, the two-layer model fit using v_{fit} describes the magnitude of the velocity profile well, and reproduces the depth-averaged phase, but predicts a larger phase lead near the seafloor than observed. A linearly increasing eddy viscosity model $v = \kappa u_* z$ with $u_* = 0.11$ m/s produces a more accurate fit to the depth dependence of the phase. The complex viscosity profile calculated from equation (13) falls between the linearly increasing solution and the depth-independent solution.

Using the value of v_{fit} from the two-layer model fit and the modeled velocity profile to estimate dissipation results in dissipation of $D_v = 2.4$ W/m^2. Since the depth-averaged phase of the velocity profile is reasonably well predicted by the two-layer model, the momentum deficit approach also predicts a similar value of 2.0 W/m^2. Both of these estimates are about a factor of 2 higher than the flux divergence estimate of dissipation of 0.9 W/m^2. Because the flow is turbulent, the clear water viscosity is probably the most representative quantity for estimating a Reynolds Number of $Re_{\delta,cw} = 897$ suggesting turbulent flow.

4.6. Wave-Supported Turbidity Flows

The burst-averaged offshore flows present within the fluid-mud layer from days 79:03 to 80:06 were examined during laminar (*L*), transitional (*Tr*), and turbulent (*Tu*) flow regimes (Figure 16) to determine if the dynamical balances for the wave-supported turbidity flows in this environment are consistent with the Chezy balance that has been used in previous studies to describe the flows on the Eel River Shelf, Northern California, and on the Po River pro-delta, Italy [*Traykovski et al.*, 2000, 2007; *Wright and Friedrichs*, 2006]. The force balance equates the downslope buoyancy force with a linearized quadratic drag term)

$$h_m g' \sin(\beta) = C_d\, u_{grav}\, |u_{max}|, \tag{36}$$

where $g' = g\,(\rho_m - \rho_w)/\rho_w$, β is the slope of the seabed, and $u_{max} = \sqrt{\tilde{u}_{0w}^2 + u_{grav}^2 + v_{curr}^2}$. The offshore directed gravitation flow speed is u_{grav} and speed of the overlying flows in the water column are v_{curr} [*Wright et al.*, 2001]. Using suspension densities of $\rho_m = 1170$, 1280, and 1300 for periods *Tu*, *Tr*, and *L*, with $\rho_w = 1025$ kg/m^3, the resulting drag coefficients (C_d) are 0.0012, 0.024, and 0.46. Thus, only the value for the turbulent flow conditions is comparable to the values of C_d between 0.0012 and 0.0016 from the previous studies. While the previous studies did not contain measurements of turbulence within the fluid-mud layers, the flow the conditions in those data sets were likely to be turbulent due to either energetic wave forcing conditions or lower suspension densities. Lower suspension densities are less likely to undergo rheological changes that damp turbulence.
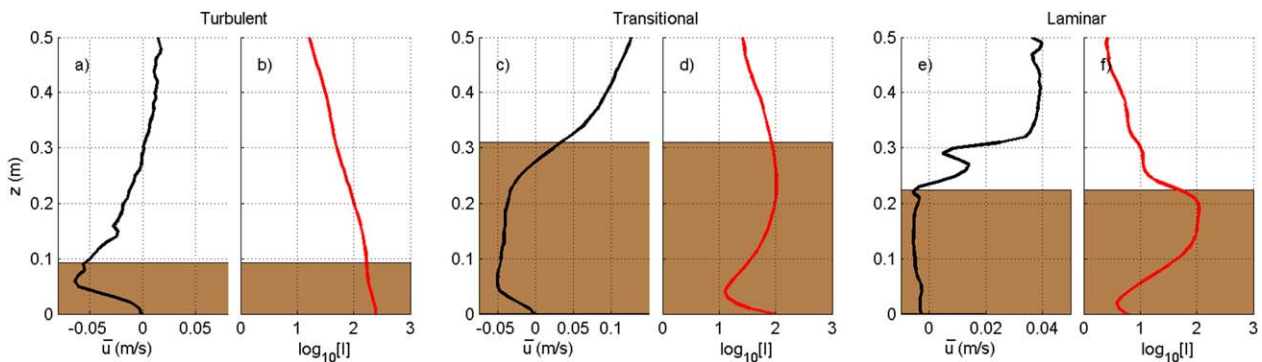
Figure 16. Burst-averaged acrossshore velocity ($\bar{u}_{0w}$) and backscattered intensity profiles showing wave-supported turbidity flows during (a and b) turbulent, (c and d) transitional, and (e and f) laminar periods.

As an alternative to the turbulent drag-based Chezy equation, the balance between the downslope buoyancy force and viscous laminar flow drag can be examined

$$h_m g' \sin(\beta) = \int_0^{h_m} v_m \frac{d^2 u_{grav}}{dz^2} dz. \tag{37}$$

From this balance, a viscosity for the gravitational flow was calculated. To perform the integral on the right-hand side, the measure burst-averaged flow profiles were fit with fifth-order polynomials. The resulting viscosities for periods Tu, Tr, and L are 0.042, 2.4×10^{-4}, and 6.5×10^{-3} m^2/s, which can be compared to the viscosities calculated from the oscillatory flows for the same periods of 0.9×10^{-3}, 1.2×10^{-3}, and 4.2×10^{-3} m^2/s (section 4.5). For these mean flow viscous drag calculations, the viscosities calculated during the fully laminar period are comparable to the viscosity estimated from the oscillatory flow. During the turbulent and transitional periods, there is a factor of 5 discrepancy between the oscillatory viscosity and the mean viscosity. This combined with the consistency of the turbulent drag coefficient with previous studies suggests that turbulence plays an important role in decreasing the apparent viscosity experienced by the mean downslope flow and thus leads to faster downslope flows than would be expected with high-viscosity ($v \sim 5 \times 10^{-3}$ m^2/s) fluid mud. *Jaramillo et al.* [2009] also describe wave-supported turbidity flows with a downslope velocity of 2 cm/s in a fluid-mud layer at a location closer to the Atchafalaya River mouth.

4.7. Internal Waves on the Lutocline and Spatial Variability of Near-Bed Flow

One of the interesting features of the high-concentration mobile fluid-mud layers shown in Figures 7, 13, 14, and 17 is the presence of internal mode waves on the lutocline. As discussed in section 2.1 (Figure 2), the dispersion relation for a two-layer system with a high-viscosity and density lower layer supports internal waves with wavelengths of 2–5 m (as ρ_m varies from 1050 to 1300 kg/m^3) in the $\hat{h}_m > 1$ regime. The observations show lutocline oscillation amplitudes that decrease from $\tilde{a}_{0int} \sim 6$ cm when the flow has higher turbulence levels (before day 79:18) to less than 1 cm during laminar flow conditions. The expected height of the vertical oscillations of the surface mode wave with $\lambda = 60$ m ranges from $\tilde{a}_{0sur} = 0.1$ to 1 cm at the lutocline elevation of 20–30 cm above the stationary bed. An analysis based on continuity also suggests that the internal waves must have wavelength considerably shorter than the surface gravity waves. Assuming that the waves have long wavelengths relative to the layer thickness ($kh_m < 1$), the wavelength of the interfacial waves can be calculated from the continuity equation

$$\frac{da_{0int}}{dt} = h_m \frac{du_{0int}}{dx}. \tag{38}$$

With periodic solutions of the form $(a_{0int}, u_{0int}) = (\tilde{a}_{0int}, \tilde{u}_{0int})e^{i(kx-\omega t)}$, all the parameters except k and $\tilde{u}_{0int}$ are known. Using values from the laminar period of $\tilde{a}_{0int} = 1.4$ cm, $h_m = 22$ cm, $\omega = 0.7$, and an
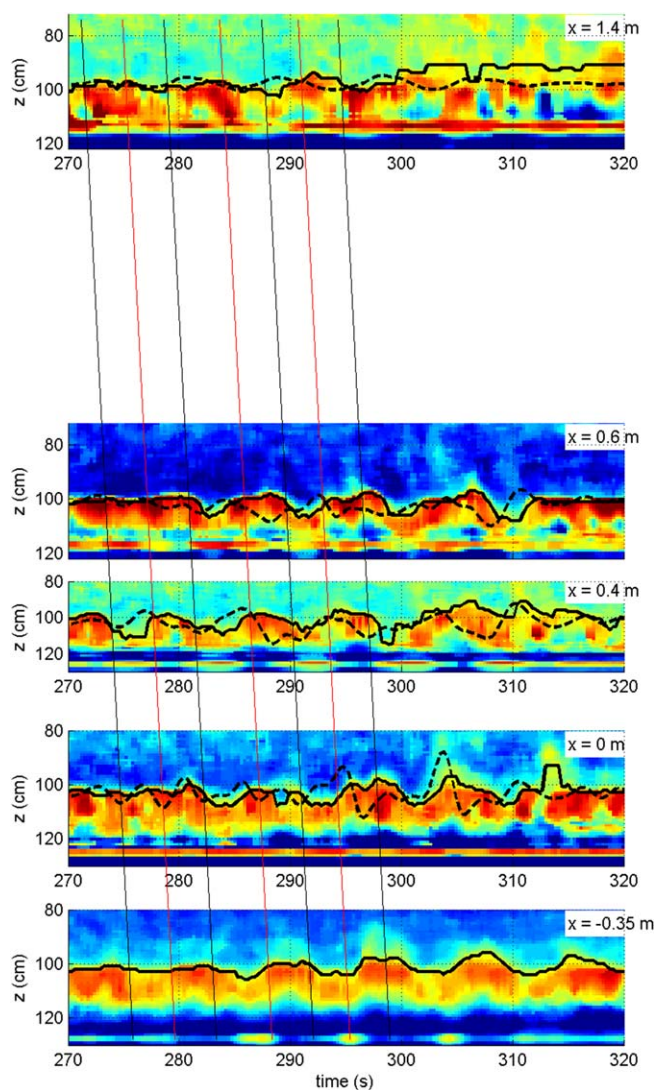
Figure 17. Internal mode lutocline fluctuations measured by the PCADP array backscattered intensity with elements at $x = 1.4, 0.6, 0.4, 0$, and -0.35 m on day 80:15 h. The thick black line indicates the location of the lutocline, and the dashed black line indicates the vertical velocity 4 cm below the lutocline (in cm/s multiplied by 10 so that it is clearly visible on the 45 cm y axis limits). The vertical velocity is not shown for the 20° off vertical sensor at $x = -0.35$. The diagonal lines track crests (black lines) and troughs (red lines) across the array elements. The fluctuations are fairly coherent across the array from t = 275 to 295s, but then become less with a turbulent bursts on some array elements after t = 295 s.

assumption that $\tilde{u}_{0int}$ are less than the surface mode horizontal velocities ($\tilde{u}_{0sur}$) results in a maximum internal mode wavelength of 16 m. The ratio of the energy under first harmonic peak of the S_{uu} spectra (Figure 10e) and the second harmonic peak is 4. If all the energy in the second harmonic was due to the internal mode this would suggest a wavelength of 8 m. Pressure spectra (not shown in Figure 10e) measured at 90 cm above the seafloor suggest that 2/3 of the energy under the second harmonic is due to the surface mode, resulting in a wavelength of 5 m. In order to match the wavelength predicted by the dispersion relation, the orbital velocities of the internal waves would have to be a factor of 4–8 lower than the horizontal velocities of the surface waves, which is consistent with the ratio of the energy in the first and second harmonics, including the correction from the pressure spectra.

The array of downward pointed Doppler profilers can be used to directly measure the wavelength of the lutocline instabilities. Figure 17 shows backscattered intensity from the four vertically aimed downward beams and the 20° off vertical beam. During the period from 275 to 300 s, the fluctuations have some coherence across the array, with a double peaked feature visible before 300 s on the x = −0.35 sensor also being fairly easy to identify in sensors at x = 0 and 0.6 m. During the period after 300 s, there is much less coherence as the lutocline develops a turbulent burst. For the waves between 280 and 300 s, the temporal delay of 4 seconds over 1.4 m with a 9 s period suggests a 3 m wavelength, consistent with the dispersion relation.

To examine the wavelength of the instabilities averaged over longer periods, the covariance of vertical velocities between sensors near the lutocline was used to produce a wave number spectra (34) (Figure 18). The cross correlations at the temporal lag that maximizes the correlation coefficient $R_{j,k}(\tau_{max})$ were calculated for every possible sensor separation (Δx) and fit with a model of $R_{j,k}(\tau_{max}) = \exp(x/L_r) + R_b$, where L_r is a correlation length scale. During the laminar flow period, sensors separated by less than 0.6 m are highly correlated, but at separations over $L_r = 0.6$ m, the correlation drops to a background level of $R_b = 0.6$. During the more energetic periods, L_r decreases from 0.4 during transitional conditions to 0.3 in turbulent conditions, and the background correlation level at large Δx also decreases to 0.53 and 0.48. Wave number spectra
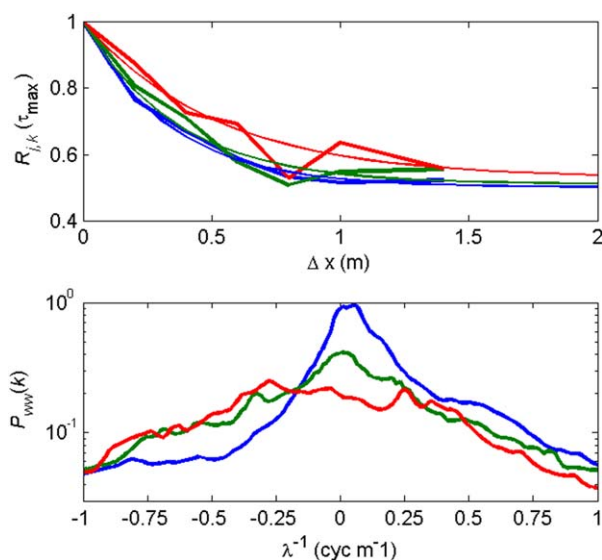
Figure 18. (a) Maximum Coherence $R_{k,l}(\tau_{max})$ as a function of array element location for turbulent (blue), transitional (green), and laminar (red) periods. (b) Spatial wave number for the same periods.

averaged over the bursts during the laminar period show a broad peak in the onshore direction with wavelengths ranging from 15 to 3 m (.06 to 0.3 cyc/m), roughly consistent with the other estimates. An additional peak at $\lambda^{-1} = 0.25$ cyc/m in the offshore propagation direction is also evident. Because the vertical velocities near the lutocline have significant contributions from surface mode oscillatory flows that have vertical flow components induced from flow over bedforms, the spatial spectrum is dominated by low wave numbers ($\lambda^{-1} < 0.1$ cyc/m) associated with the surface mode. There are large internal mode motions during the turbulent period but they are not spatially coherent enough to produce a spectral peak. During the turbulent period, the motions may be less wave like, as indicated by the low coherence across the array, and better described as a turbulent bursting phenomena. Evidently during the laminar flow period, the vertical component of flow induced by topography is restricted to a near-bed region so the internal mode motions are well resolved in the spatial spectral analysis. In the transitional period, the spectra shows an combination of both effects with a spectral peak from $\lambda^{-1} = 0$ to -0.23 cyc/m.

4.7.1. Generation Mechanisms

Two of the more commonly discussed mechanisms for the generation of internal waves in the ocean in general are shear-induced Kelvin-Helmholtz instabilities and lee waves generated by flow over topography. The theoretical solutions and the observations of a phase difference of $15°$ across the lutocline indicate there is potential for shear in the horizontal velocities; however, the velocity difference across the interface is relatively small with values of Δu typically less than 5 cm/s. Instability theory for a finite thickness lower layer with an infinite upper layer with no viscosity defines a parameter space for growing Kelvin Helmholtz solutions

$$k > \frac{g'(1+(\rho_w/\rho_m)tanh(kh_m))}{\rho_w/\rho_m \Delta u^2},$$ (39)

where Δu is the shear across the interface. This indicates only very short waves, with wavelengths less than 1 cm based on reasonable choices of the parameters ($g' = 1.5$ m/s^2, $\rho_w/\rho_m = 0.85$) are unstable. Assuming a maximum steepness of ~ 0.4, Kelvin-Helmholtz instabilities would have heights of less than 0.4 cm and are thus inconsistent with the observations of heights of 3–10 cm and wavelengths greater than 1 m. Examination of the critical Richardson number, $Ri_c = g'h_i/\Delta u^2 = 0.25$, suggests that the available kinetic energy from the shear could only mix a very limited region ($h_i = 5$ mm) given the large density contrast and weak shear. However, as discussed by J. H. Trowbridge and P. Traykovski (manuscript in preparation, 2015), with oscillatory forcing, unstable solutions are possible at wave numbers associated with dispersion relation (8) for this two-layer system. This "resonant parametric instability" is forced by shear at the interface and allows for the possibility of unstable waves in a parameter space that is consistent with the observations.

An alternative mechanism to shear generation is flow over topography. The burst-averaged measurements on yearday 80:15 from the spatial array of downward pointed Doppler profilers show that there are 15 cm monotonic variations in bed elevation over the 2.0 m length of the array (Figure 19). The location of the bed was defined by two different techniques (see section 3.3). In Figure 19a, the second
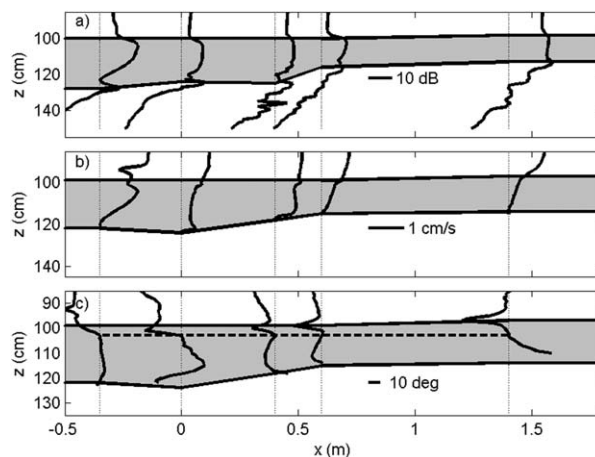
Figure 19. Vertical profiles of (a) backscatter, (b) vertical orbital velocity amplitude $\tilde{w}$, and (c) phase of along-beam velocity relative to a range bin near the lutocline (shown as a dashed line) from each element of the PCADP array indicating the presence of stationary bedforms on day 80:15. Each profile is referenced to zero, shown as a thin dashed vertical line. The bottom location as measured by the backscatter (η_{ba}, Figure 19a) and level of no motion (η_{nm}, Figures 19b and 19c), and lutocline location as measured by backscatter gradient, and the phase gradient are shown as solid black lines below and above the gray shaded region.

peak in backscattered amplitude is used (η_b), and in Figure 19b, the level of no motion ($\eta_{nm,i}$), defined by the first point with $\tilde{w} < 2$ mm/s, is used. While these methods do not produce the exact same results, both show significant slopes in bed elevation. The burst-averaged location of the lutocline is approximately horizontal over the length of the array indicting that the variation in bed return was most likely not due to a tilt of the array with respect to vertical. Due to the 35 cm minimum sensor separation, this array does not resolve small-scale bedforms; however, the 15 cm bed elevation differences indicate that the bedforms would probably have wavelengths over 100 cm as bedform steepness over 0.15 is rare. Since the bedforms have spatial scales that are roughly consistent with the observed instabilities on the lutocline, some combination of the parametric instability with additional forcing from flow over topography is possible.

4.7.2. Bedforms

Bed elevation profiles over the length of the array conducted for all the data bursts from yearday 78 to 81 show that the bed was stable from yearday 78 to 78:15 and again from 79:19 to 81 (Figure 20). During the peak of the storm from yearday 78:15 to 79:19, the bedforms are mobile with temporal elevation changes averaged over all the sensors in the array ($\langle|d\eta_b/dt|\rangle$, where the $\langle\rangle$ indicates a spatial average over all 5 array elements) of up to 1.3 cm/h. Continued mobility at a lower rates is observed until yearday 80:12. The level of no motion analysis (red lines in Figures 13c and 14c) applied to the PCADP velocity data during the transitional (yd 80:00) and turbulent periods (yd 79:06) show stationary bed elevation variability of several centimeters on the wave group time scale. Plotting the rate of bed elevation change against wave velocity in the fluid-mud layer shows the threshold for bedform mobility to be 40 cm/s, similar to the 30–40 cm/s (shields numbers of 0.1–0.2, based on *Nielsen* [1992] friction factor) required for a medium to coarse grained sand bed to have similar thresholds for mobility [*Traykovski*, 2007]. The presence of bedforms suggests that the generation mechanism for the internal waves on the lutocline could be a combination of flow over topography and oscillatory flow-forced instabilities.

The presence of bedforms and the spatial array measurements of phase may also explain the discrepancies between the laminar two-layer model solutions for phase, which always approach 45° near the bed, and the observed phase, which has more complex vertical structure and spatial variability [*Hurther and Thorne*, 2011; *Nielsen*, 1992; *van der Werf et al.*, 2007]. The along-beam velocity phase measurements shown in Figure 19c are referenced to a range bin near the lutocline for each sensor independently, thus the quantity shown in Figure 19c describes the vertical variation of phase of along-beam velocity through the fluid-mud layer. While the phase of the 20° off vertical beam ($x = -0.35$ m) is relatively uniform, the vertical beams located at $x = 0$ and $x = 1.4$ m show a large variation in phase in the lower 10 cm of the fluid-mud layer. The phase profiles of the downward aimed beams at $x = 0.4$ and 0.6 m on the slope of the bedforms are similar to each other. These results were temporally stable over the period from day 79:19 to 81 when the bedforms were stationary. During periods with mobile bedforms, the phase structure has temporal coherence scales of several hours (e.g., Figure 9d), similar to bedforms shown in Figure 20a. Due to the temporal coherence of the variations in phase with temporal evolution of the bedforms, the most likely explanation for the vertical variations in phase is spatially variable flows over the bedforms. This result offers an explanation for the disagreement of the observed phase during the laminar period and the model results (Figure
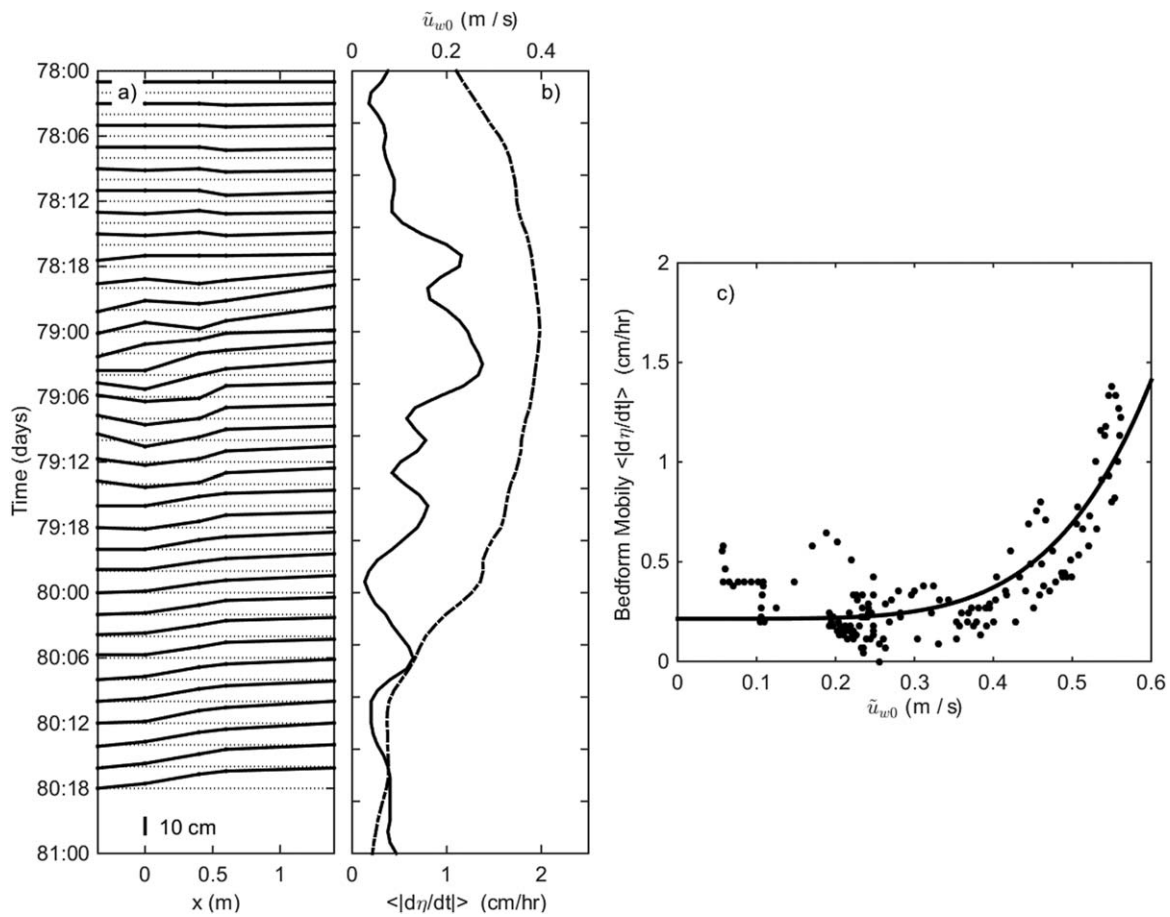
Figure 20. (a) Time series of bed elevation profiles indicating evolving bedforms from day 78:00 to 80:18. The scale bar indicates 10 cm elevation above the dashed referenced lines for each temporal sample. (b) Time series of bedform mobility ($\langle|d\eta_b/dt|\rangle$ lower x axis, solid line), and wave orbital velocity amplitude ($\tilde{u}_{0w}$, upper x axis (dash-dot)). (c) Bedform mobility versus $\tilde{u}_{0w}$ and a least squares fits of the form $a+b\tilde{u}^5_{0w}$.

11a). While the flow does not become turbulent during this period due to the stabilization provided by the high viscosity, the presence of bedforms may introduce oscillatory flow patterns that cause the phase to differ from the laminar flow flat-bed solutions with 45° near-bed phase.

4.7.3. Wave Attenuation Due to the Internal Mode Oscillations

While the measurements show that internal waves are present, the modeling results (section 2.1) suggest they do not dominate the wave attenuation. The wave attenuation of the surface waves from the internal waves energy dissipation is calculated by D_{int}/F_{ext} which is dependent on the ratio $\tilde{a}_{0int}/\tilde{a}_{1sur}$. The observations in the turbulent and laminar periods show values of $\tilde{a}_{0int}/\tilde{a}_{1sur} \sim 0.1$. During the transitional period, the amplitude of the internal mode oscillations increases while the surface wave heights decrease resulting in $\tilde{a}_{0int}/\tilde{a}_{1sur} \sim 0.2$. The Gaussian-shaped bump in the normalized internal mode dissipation curves shown in Figure 2a show the increased dissipation due to an increase in $\tilde{a}_{0int}/\tilde{a}_{1sur}$ from 0.075 to 0.2 in the vicinity of $\hat{h}_m = 4$. This empirically based increase near $\hat{h}_m \sim 4$ suggests that the maximum dissipation due to the internal mode oscillations of the fluid-mud layer is 10–50% of that due to the external mode oscillations. At higher viscosities relative to layer thickness ($\hat{h}_m < 0.5$), the model solutions show potential for increased attenuation due to internal waves, but these high viscosities were not observed in the data, and it is expected that motion of the fluid-mud layer would be minimal with such high viscosities (Figure 3), thus limiting the formation of internal waves.

While this analysis indicates that the internal mode fluctuations probably do not dominate the attenuation, it is likely that they do play an important role is modulating the mixing across the lutocline and within the

fluid-mud layer and thus have potential to control the layer density and viscosity. During the later stages of the turbulent period and during the transitional period, the turbulent dissipation is often greatest near the lutocline (Figure 9e, 79:20–80:08), suggesting turbulence at generating at the interface could be equally important to bed generated turbulence. It is likely that the system undergoes positive feedback whereby during low energy conditions the internal waves are small thus leading to low mixing, high fluid-mud layer viscosities and high densities resulting in high wave attenuation. Conversely, during energetic periods, the internal mode fluctuations are large leading to more mixing and thus lower densities, viscosities, and reduced wave attenuation.

5. Conclusions

The observations described here reveal mechanisms of wave attenuation over a thin high sediment concentration boundary layer in 9–5 m water depths. During energetic wave conditions, the total energy dissipation (D) in the fluid-mud layer is high, but the flux normalized attenuation rate (κ) is small with values around 0.1 km^{-1}. The total energy dissipation decreases as wave energy decreases toward the end of the wave events, while κ increases to values around 0.4–0.8 km^{-1}. This transition from high D-low κ to low D-high κ is associated with the transition from turbulent to laminar flow in the fluid-mud layer. As the oscillatory forcing on the fluid-mud layer decreases, the acoustic attenuation through the layer dramatically increases, indicating an increase in sediment concentration. This increase in attenuation rate after the wave event, as fluid-mud layers settle, is consistent with results of other recent studies [*Jaramillo et al.*, 2009; *Sheremet et al.*, 2011; *Winterwerp et al.*, 2012]. While the temporal variability of sediment concentration in the mobile fluid-mud layer was not directly measured in this study, a two parameter inverse using the measured oscillatory velocity profiles within the fluid-mud layer to calculate parameters ρ_m and v indicates a fluid-mud layer density increasing from 1170 kg/m^3 in turbulent conditions to 1300 kg/m^3 in laminar flow fluid-mud layer conditions. There is large uncertainty in the estimate of the density for the turbulent case due to the breakdown of the two-layer assumption and smoothing of shear across the lutocline. In the laminar case, measurement errors near the lutocline also lead to uncertainty in the fluid-mud density estimates. These values from the inverse are roughly consistent with box cores indicating 2–8 cm thick recently deposited mud layers with bulk densities of approximately 1200–1300 kg/m^3, suggesting that the fluid-mud concentrations during the laminar flow periods were very close to the gel point. This increase in concentration is associated with a transition from turbulent flow to laminar flow as indicated by a dramatic reduction of turbulent velocity fluctuations and absence of the inertial subrange as the flow becomes laminar, whereas during the turbulent phase, a broad $f^{-5/3}$ inertial subrange with energetic turbulent velocity fluctuations is present. The transition from turbulent to laminar flow is also associated with an order of magnitude increase in effective viscosity to a level 3 orders of magnitude greater than clear water. During the laminar fluid-mud flow periods, the high viscosity inferred from the two parameter inverse of $v = .4$ m^2/s is not due to turbulence, because the observations indicate turbulent fluctuations are highly suppressed. During the turbulent fluid-mud layer flow period, the measurements do not allow robust separation of the eddy viscosity component of the mixture viscosity from the total effective viscosity, due to a lack of high-quality Reynolds stress measurements in the fluid-mud layer. The Reynolds numbers (Re_A) calculated from viscosity estimates based on measured velocity profiles decreased by 2 orders of magnitude from the turbulent flow to laminar flow. Estimates of the low-frequency limits for the inertial subrange change from 11 Hz (above the Nyquist limit of sampling) during turbulent flow to 0.15 Hz (just above the wave forcing peak) during laminar flow. This is consistent with the observations of the presence of an inertial subrange during turbulent flow and absence during laminar flow.

During the laminar flow phase, both the boundary layer and across-shelf energy flux divergence observations of wave energy dissipation are consistent with two-layer theory with a laminar viscous lower layer as described by *Dalrymple and Liu* [1978]. Based on the high viscosity inferred from the velocity profile, the estimates of the attenuation rate from the fluid-mud layer measurement of $\kappa = 0.5$ km^{-1} is consistent within a factor of 2 with the across-shelf wave-attenuation measurement from the 9 m isobath to the 5 m isobath of $\kappa = 0.3$ km^{-1} based on wave energy flux divergence measurements. The factor of 2 might be explained by spatial variations in the dissipation, as the attenuation was larger in between the 7 and 5 m isobaths with values of $\kappa = 0.45$ km^{-1}. The attenuation during the periods of laminar fluid-mud layer flow ($\kappa = 0.5$ km^{-1}, located at $\hat{h}_m = 2.0$) is close to the maximum predicted by

two-layer laminar flow theory of $\kappa = 0.7$ km^{-1}, located at $\hat{h}_m = 1.12$. The physical mechanism causing maximal viscous dissipation is curvature of the velocity profile encompassing the entire fluid-mud layer, which was directly measured by the acoustic Doppler velocity and backscatter profiles.

During the turbulent flow period, the reduced normalized dissipation compared to the laminar period is qualitatively consistent with predictions from two-layer theory if the viscosity is considered as an eddy viscosity. However, the physical mechanism of turbulent dissipation is different from the laminar viscous dissipation in the theory resulting in important consequences for inverses for mud layer properties based on wave-attenuation measurements, as the eddy viscosity is related to the turbulence and not the direct properties of the fluid mud. Comparing estimates of turbulent dissipation in the boundary layer to across-shelf energy flux divergence estimates is sensitive to the method chosen. Despite the presence of turbulent fluctuations, and a well-developed $f^{-5/3}$ inertial subrange during the turbulent period, calculation of the turbulent energy dissipation using the inertial dissipation method based on vertical velocity fluctuations results in values a factor of 80 less than the measured flux divergence. Examination of the anisotropy of the turbulent flow, based on several different assumed levels of Reynolds Stress, suggests the inertial dissipation method may not be appropriate for this highly stratified flow near the seafloor boundary. During the turbulent flow period, estimates of bed friction velocity (u_*) based on vertical velocity fluctuations results in friction factors ($f_{w,w'}$) consistent with energy-dissipation factors calculated from flux divergence ($f_{e,Fx}$) and Nielsen's wave friction factor ($f_{w,N}$ based on a roughness of $r = 2.5$ and wave forcing parameters). As the flow becomes laminar, the turbulent fluctuations decrease dramatically, with an order of magnitude decrease in vertical turbulent velocity variance ($\sigma_{w'}$) and friction factor ($f_{w,w'}$).

The role of internal waves on the lutocline may have a significant impact on the dynamics of these turbulent flows. Internal waves were measured with a 2–5 m wavelength consistent with the two-layer model dispersion relation and up to 10 cm height. Estimates of dissipation due to the internal waves alone based on a modeled internal mode velocity profiles with measured amplitudes, and a viscosity based on the fitting the surface mode velocity profiles, revealed that the internal wave motions alone are not responsible for the observed attenuation rates. The internal wave dissipation is at least 50% less than that due to the directly forced surface wave motions in the fluid-mud layer. However, the internal waves may play an important role in modulating the turbulence, as elevated vertical velocity fluctuations were observed both near the bed due to boundary layer generated turbulence, and near the lutocline due to internal wave breaking or turbulent bursting. While the observations and analysis do not directly confirm the mechanism for the generation of the internal waves on the lutocline, shear from the surface wave mode velocity profile at the lutocline and flow over bedforms were both identified as possible mechanisms. The relatively weak shear and high-density contrast indicate Kelvin-Helmholtz instabilities can only occur at very small scales and are not consistent with the observations of larger-scale instabilities. Flow over large-scale bedforms combined with a "parametric instability" at the resonant condition described by the two-layer dispersion equation is the most likely forcing mechanism for the instabilities. The bedforms have spatial scales of one to several meters wavelength, and 5–15 cm height, similar to the instabilities of the lutocline. Based on the lack of sand in any of the bed samples, these bedforms probably consist of fine sediment with similar grain size properties to the fluid mud in suspension. The bedforms are mobile during energetic conditions and become stationary under laminar flow. The presence of bedform also offers an explanation for the phase lead of the near-bed flow deviating from the theoretical solutions of the 45° lead, as bedforms can induce complicated flow patterns with phase leads and lags depending on the location of the measurement position relative to the bedform crest [*Hurther and Thorne*, 2011; *van der Werf et al.*, 2007].

The transition from turbulent flow with high total dissipation (*D*) and low normalized attenuation (κ) to laminar flow with to low *D* and high κ, either as a function of time, as the storm wanes, or space, as waves propagate and attenuate toward the shore, has potential to set up a positive feedback mechanism. The feedback would allow rapid increases in attenuation as the flow in the high-concentration layer becomes laminar during the settling phase of the fluid-mud layer. This would also be accompanied by reduced transport rates during laminar flow thus further increasing the positive feedback.

These observations also reveal new insight into the dynamics of wave-supported turbidity flows during the transition from turbulent to laminar flows. Wave-supported turbidity flows have been documented to be an important transport mechanism in locations with these high-concentration

layers [*Wright and Friedrichs*, 2006]. Previous field [*Traykovski et al.*, 2007] and modeling [*Hsu et al.*, 2009] studies focused on the turbulent regime due to the highly energetic forcing conditions and found that a Chezy balance with a $C_d \sim 0.0015$ could describe most of the flows. During the turbulent flow phase of the new observations from Louisiana, a similar C_d was found. As the flow transitions to the laminar regime, the effective drag coefficient increases dramatically by several orders of magnitude. The laminar flow wave-supported gravity flows are better described by a balance of gravitational downslope buoyancy forcing against viscous drag. During the laminar phase, the viscosity used to model this balance is similar to the viscosity of 0.005 m/s^2 used to model the velocity profiles of the oscillatory flow, while during the transitional flow cases the estimates of viscosity for the mean flow are smaller than the viscosities calculated from the oscillatory flow. The potential for wave-supported gravity flows to alter the across-shelf distribution of the near-bed fluid-mud layers could have a significant effect on the temporal and spatial variability of wave attenuation. Wave-supported gravity flows can transport mobile fluid layers offshore and control the thickness of fluid-mud layers via convergence and divergence of the offshore flow [*Harris et al.*, 2005; *Scully et al.*, 2003]. Due to the vertical decay of wave orbital velocities, waves will interact mostly strongly with the seafloor in shallow water. However, large orbital velocities at the seafloor have potential to cause a transition to a turbulent fluid-mud layer which is less effective in dissipating wave energy than a high-viscosity laminar flow. Thus, in order to understand the temporal evolution of waves at the shoreline, a careful consideration of the feedbacks between fluid-mud layer properties (location, thickness, and concentration) and flow regime with respect to the laminar-turbulent is required. From an inverse perspective, the transition from turbulent to laminar flow in the fluid-mud layer can dramatically increase the wave-attenuation rate during the waning stages of a storm, thus allowing the detection of fluid mud or inference of the flow regime from the surface wave attenuation.

Appendix A

This appendix contains a table of observed and model fit parameters from turbulent, transitional, and laminar periods (Table A1). The dispersion relation derived by *Kranenburg et al*. [2011, equation 25] is:

$$A_1 \; \omega^4 + \; B_1\omega^3 + B_2\omega^2 + \; B_3\omega + A_2 = 0 \tag{A1}$$

$$A_1 = \frac{\cosh(kh_w)\cosh(mh_m)}{k} - \frac{\rho_w}{\rho_m}\frac{\sinh(kh_w)\sinh(mh_m)}{m} + h_m\frac{\rho_w}{\rho_m}\sinh(kh_w)\cosh(mh_m) \tag{A2}$$

$$B_1 = 2ik\nu\left[\cosh(kh_w)(\cosh(mh_m)-1)\right]$$

$$B_2 = \; g\left[\frac{k}{m}\cosh(kh_w)\sinh(mh_m) - kh_m\cosh(kh_w)\cosh(mh_m) - \sinh(kh_w)\cosh(mh_m)\right]. \tag{A3}$$

$$B_3 = \; 2igk^2\rho_m\nu\left[\;\sinh(kh_w)(1-\cosh(mh_m))\right]$$

$$A_2 = \; g^2k^2\left[h_m\frac{\rho_m-\rho_w}{\rho_m}\;\sinh(kh_w)\cosh(mh_m) - \frac{\rho_m-\rho_w}{\rho_m}\frac{\sinh(kh_w)\sinh(mh_m)}{m}\;\right] \tag{A4}$$

where $m = (1-i)/\delta_\nu$.

Profiles of the complex horizontal and vertical velocity amplitudes in the water layer are given by *Kranenburg et al*. [2011, equation (16)]:

$$\tilde{u}_w = C_1\sinh(kz) + i\; C_4\cosh(kz). \tag{A5}$$

$$w_w = iu_w. \tag{A6}$$

Profiles of the complex horizontal [*Kranenburg et al.*, 2011, equation 18] and vertical velocity amplitudes in the fluid-mud layer are given by

Table A1. Observed and Model Fit Parameters From Turbulent, Transitional, and Laminar Periods

	Turbulent	Transitional	Laminar
Forcing Conditions			
$H_{m0,9}$ (m)	1.71	0.84	0.28
$H_{m0,7}$ (m)	1.66	0.78	0.25
$H_{m0,5}$ (m)	1.60	0.75	0.20
f (Hz)	0.11	0.12	0.11
Flux, Flux Divergences, and Friction Factors			
F_9 (W/m)	11,200	3040	373
F_7 (W/m)	11,500	2580	266
F_5 (W/m)	9280	2070	156
$F_{x9,5}$ (W/m^2)	0.64	0.33	0.073
$\kappa_{9,5}$ (1/km)	0.067	0.13	0.28
$F_{x7,5}$ (W/m^2)	1.93	0.440	0.094
$\kappa_{7,5}$ (1/km)	0.186	0.19	0.45
$f_{e,Fx}$	0.022	0.076	0.56
$f_{w,N}$	0.029	0.047	0.10
Lutocline and Boundary Layer Model Forcing Parameters			
h_m (cm)	10	31	22
$\bar{a}_0$ (cm)	5.6	5.2	0.8
$\bar{u}_{0w}$ (m/s) PCADP	0.51	0.23	0.085
A (m)	0.79	0.31	0.12
Viscous Two-Layer Model Fit Parameters			
v_{fit} (m^2/s)	9.2×10^{-4}	1.2×10^{-3}	4.2×10^{-3}
ρ_m (kg/m^3)	1170	1280	1300
δ_v (cm)	5.1	5.7	11.0
D_v (W/m^2)	2.4	0.43	0.11
κ_{fit} (1/km)	0.26	0.26	0.50
$\hat{h}_m$	2.0	5.5	2.0
ε_{fit} (W/kg)	2.03×10^{-2}	1.09×10^{-3}	3.9×10^{-4}
Momentum Deficit Estimate Parameters			
D_{md} (W/m^2)	1.97	n/a	0.09
κ_{md} (1/km)	0.22	n/a	0.40
v_{md} (m^2/s)	8.9×10^{-4}	n/a	3.6×10^{-3}
Turbidity Flow Parameters			
v_m (m^2/s)	0.042	2.4×10^{-4}	6.5×10^{-3}
C_d	0.0012	0.024	0.46
Turbulence Parameters			
$\sigma_{w'}$ (m^2/s^2)	3.0×10^{-2}	1.6×10^{-2}	2.5×10^{-3}
$\varepsilon_{t,IDM}$ (W/kg)	2.3×10^{-4}	3.6×10^{-5}	4.2×10^{-7}
$D_{t,IDM}$ (W/m^2)	2.5×10^{-2}	1.4×10^{-2}	1.2×10^{-4}
$f_{e,IDM}$	6.5×10^{-4}	2.9×10^{-3}	9.7×10^{-4}
$f_{w,w'}$	2.3×10^{-2}	26×10^{-2}	7.2×10^{-3}
$\delta_{t,IDM}$ (cm)	2.0×10^{-2}	5.0×10^{-2}	1.0×10^{-2}
$\delta_{t,w'}$ (cm)	1.3	0.67	6.0×10^{-2}
Laminar-Turbulent Transition Parameters			
Re_A	437	59.4	2.43
Re_δ	29.6	10.9	2.2
$Re_{A,cw}$	4.03×10^5	7.13×10^4	1.02×10^4
$Re_{\delta,cw}$	897	377	143
η_k (m)	4.2×10^{-2}	8.0×10^{-2}	0.62
η_f (Hz)	9.1	2.0	0.14

$$\tilde{u}_m = C_3 \cosh(mz) + i\, C_4\, \sinh(mz) + E\frac{k}{\omega \rho_m}. \tag{A7}$$

$$\tilde{w}_2 = C_3\,\frac{ik}{m}\,\sinh(mz) + C_4\,\frac{k}{m}(\cosh(mz)-1) + E\frac{ik^2 z}{\omega \rho_m}. \tag{A8}$$

With coefficients given by *Kranenburg* [2008, equations 148–151]:

$$C_1 = \left[-\frac{gk}{\omega}\sinh(kh_w) + \omega\cosh(kh_w)\right]a_1 \; . \tag{A9}$$

$$C_2 = \left[\frac{gk}{\omega}\cosh(kh_w) - \omega\sinh(kh_w)\right]a_1 \ . \tag{A10}$$

$$C_3 = \frac{\omega\tilde{a}_0 m\cosh(mh_m)}{k(-\sinh(mh_m) + \cosh(mh_m)mh_m)} . \tag{A11}$$

$$C_4 = \frac{i\omega\tilde{a}_0 m\sinh(mh_m)}{k(-\sinh(mh_m) + \cosh(mh_m)mh_m)} . \tag{A12}$$

$$E = -C_3 \ \omega\rho_m/k. \tag{A13}$$

These equations are valid for both surface and internal modes with the appropriate choice of wave number from the dispersion relation.

The complex amplitude of elevation oscillations of the mud-water interface are given by

$$\tilde{a}_0 = \left[\cosh(kh_w) - \frac{gk}{\omega^2}\sinh(kh_w)\right]\tilde{a}_1 \ . \tag{A14}$$

1. Notation

1.1. Variable Definitions

a_0	displacement and amplitude of mud-water interface oscillations, m.
a_1	displacement of the water-air interface oscillations, m.
A	wave orbital motion semidisplacement, m.
A_N	turbulent velocity fluctuation anisotropy.
B_w	constant used in inertial dissipation method calculations of ε_t.
b_i	PCADP along-beam velocity from the ith sensor, m/s.
C_a	sound speed, m/s.
Cg	wave group velocity, m/s.
$C_{ij}(\tau)$	cross covariance of the i and jth PCADP array elements as a function of lag τ, m^2/s^2.
c	wave phase velocity, m/s.
D	wave energy dissipation, W/m^2.
$D_{v''}$	wave energy dissipation due laminar viscous flow, W/m^2.
D_{md}	wave energy dissipation calculated by the momentum deficit approach, W/m^2.
E	wave energy density, J/m^2.
F	wave energy flux, W/m.
F_x	wave energy flux divergence, W/m^2.
f	frequency of wave oscillations, 1/s.
f_{0w}	representative frequency, 1/s.
f_u, f_l	upper and lower frequency bounds used in swell band integrals, 1/s.
f_c	acoustic transmission carrier frequency for PCADP, 1/s.
f_e	wave energy dissipation factor.
$f_{e,Fx}$	wave energy dissipation factor based on flux divergence.
$f_{e,IDM}$	wave energy dissipation factor based on inertial dissipation method.
$f_{w,N}$	wave friction factor based on the Nielsen formula.
$f_{w,w'}$	wave friction factor based on turbulent vertical velocity fluctuations.
g	gravitational acceleration, m/s^2.
g'	reduced gravity in the two-layer system, m/s^2.
H_{m0}	wave height estimated from zeroth moment. $H_{m0,5}$ indicates the 5 m isobath site, m.
h_w	water layer thickness, m.
h_m	fluid-mud layer thickness, m.
$\hat{h}_m$	normalized fluid-mud layer thickness.
k	complex wave number, rad/m.
k_{sur}	complex wave number for the surface wave (long wavelength) mode, rad/m.
k_{int}	complex wave number for the internal wave (short wavelength) mode, rad/m.

I	backscattered acoustic Intensity (uncalibrated).
$P_{ww}(k)$	spectra of the vertical velocity as a function of horizontal wave number, m^3/s^2.
$R_{ij}(\tau)$	cross correlation of the i and jth PCADP array elements as a function of lag τ.
Re	Reynolds Number. subscript cw refers to values based on clear water viscosity.
Re_A	Reynolds Number based on orbital amplitude.
Re_δ	Reynolds Number based on Stokes layer thickness.
$S_{a_1 a_1}$	wave surface elevation spectra, m^2 s.
S_{uu}, S_{ww}	spectra of horizontal and vertical velocity fluctuations, m^2/s.
S_{up}, S_{vp}	cospectra of along and across array velocity and pressure fluctuations, m^2/s.
T_p	peak period of wave surface elevation spectra, s.
T_{prf}	PCADP pulse repetition frequency, s.
$\tilde{u}_{0w}$	complex horizontal wave orbital velocity amplitude at bottom of water, m/s.
$\tilde{u}_{0m}$	complex horizontal wave orbital velocity amplitude at top of fluid-mud layer, m/s.
$\tilde{u}_w$	Ecomplex horizontal wave orbital velocity amplitude in the water layer, m/s.
$\tilde{u}_m$	complex horizontal wave orbital velocity amplitude in the fluid-mud layer, m/s.
$\bar{u}_{0w}, \bar{v}_{0w}$	across and alongshore burst-averaged currents at bottom of water layer, m/s.
u, u_w, u_m	time-dependent horizontal wave orbital velocities, m/s.
u', v', w'	turbulent velocity fluctuation components, m/s.
$u*$	friction velocity, m/s.
V_{max}	PCADP ambiguity velocity, m/s.
w, w_w, w_m	time-dependent vertical wave orbital velocities, m/s.
$\tilde{w}, \tilde{w}_w, \tilde{w}_m, \tilde{w}_0$	complex wave orbital vertical velocity amplitudes, m/s.
$yd{:}hrs$	yearday, e.g., 1:12 at 12 am, Jan 1, 2008 gmt, days:hours.
Z	vertical distance from the seafloor, positive upward, m.
z_t	vertical distance from the acoustic transducer, positive downward, m.
z_r	along-beam distance from the acoustic transducer, positive away from transducer, m.
α_i	angle with respect to vertical of ith PCADP beam, °.
δ_v, δ_t	laminar (v) and turbulent (t) oscillatory boundary layer thickness, m.
$\varepsilon, \varepsilon_t, \varepsilon_v$	local dissipation, turbulent dissipation, and laminar dissipation rate, m.
ϕ_u, ϕ_w	phase of $\tilde{u}_m$ relative to $\tilde{u}_{0w}$, and $\tilde{w}_m$ relative to $\tilde{w}_0$, °.
$\kappa, \kappa_{sur}, \kappa_{int}$	spatial attenuation rates, 1/m.
v	kinematic viscosity of mud layer, m^2/s.
v_t	turbulent eddy viscosity.
v_m	fluid-mud viscosity.
ρ_w, ρ_m	water layer density, fluid-mud layer density, kg/m^3.
$\eta_{b,i}$	bed elevation at ith PCADP array transducer from the peak in backscatter, m.
$\eta_{nm,i}$	bed elevation from the level of no motion, m.
η_k	Kolmogorov microscale, m.
η_f	Kolmogorov frequency, 1/s.
σ_{a_0}	root mean square of lutocline elevation fluctuations, m/s.
τ_0	bed stress, Pa.
θ	wave directional spectra, °.
θ_a	wave directional spectra relative to array direction, °.
ω	radian frequency of wave oscillations, rad/s.
r	hydraulic roughness, m.
r_t	PCADP along-beam range, m.

Tilde overbar indicates an amplitude of an oscillatory quantity. Subscript 0 indicates pertaining the mud-water interface, 1 indicates pertaining the water air interface, w to within the water layer, m to within the fluid-mud layer, int to internal mode oscillations and sur to surface mode oscillations. Combinations such as $\tilde{u}_{0m}$ indicate the oscillatory velocity amplitude just above the mud-water interface in the water layer. Subscripts 5, 7, 9 refer to measurements on 5, 7, and 9 m isobaths, e.g., spatial derivatives of flux divergence: $F_{x9,5}$ or $\kappa_{9,5}$ refer to differences between the measurements on the 5 and 9 m isobaths and F_9 refers to wave energy flux at the 9 m site. There are some exceptions based on conventional usage such as H_{m0}.

References

Allison, M. A., G. C. Kineke, E. S. Gordon, and M. A. Goni (2000), Development and reworking of a seasonal flood deposit on the inner continental shelf off the Atchafalaya River, *Cont. Shelf Res.*, *20*(16), 2267–2294, doi:10.1016/S0278-4343(00)00070-4.

Bluteau, C. E., N. L. Jones, and G. N. Ivey (2011), Estimating turbulent kinetic energy dissipation using the inertial subrange method in environmental flows, *Limnol. Oceanogr. Methods*, *9*, 302–321, doi:10.4319/lom.2011.9.302.

Burdic, W. S. (1991), *Underwater Acoustic System Analysis*, Prentice Hall, Englewood Cliffs, N. J.

Campbell Scientific, I. (2011), *OBS-5+ System Operators Manual*, Rev 2/11, Logan, Utah. [Available at https://s.campbellsci.com/documents/us/manuals/obs-5+.pdf.]

Capon, J. (1969), High-resolution frequency-wavenumber spectrum analysis, *Proc. IEEE*, *57*(8), 1408–1418.

Dalrymple, R. A., and P. L. F. Liu (1978), Waves over soft muds: A two-layer fluid model, *J. Phys. Oceanogr.*, *8*, 1121–1131, doi:10.1175/1520-0485(1978)008<1121:WOSMAT>2.0.CO;2.

Dean, R. G., and R. A. Dalrymple (1984), *Water Wave Mechanics for Engineers and Scientists*, 368 pp., Prentice Hall, Englewood Cliffs, N. J. [Reprinted, World Sci., Singapore, 1991.]

Draut, A. E., G. C. Kineke, D. W. Velasco, M. A. Allison, and R. J. Prime (2005), Influence of the Atchafalaya River on recent evolution of the chenier-plain inner continental shelf, northern Gulf of Mexico, *Cont. Shelf Res.*, *25*(1), 91–112, doi:10.1016/j.csr.2004.09.002.

Elgar, S., and B. Raubenheimer (2008), Wave dissipation by muddy seafloors, *Geophys. Res. Lett.*, *35*, L07611, doi:10.1029/2008GL033245.

Foda, M. A. (1989), Sideband damping of water-waves over a Soft Bed, *J. Fluid Mech.*, *201*(189-201), 189–201, doi:10.1017/S0022112089000893.

Gade, H. G. (1958), Effects of a nonrigid, impermeable bottom on plane surface waves in shallow water, *J. Mar. Res.*, *16*(2), 61–82.

Harris, C. K., and P. L. Wiberg (2001), A two-dimensional, time-dependent model of suspended sediment transport and bed reworking for continental shelves, *Comput. Geosci.*, *27*(6), 675–690, doi:10.1016/S0098-3004(00)00122-9.

Harris, C. K., P. A. Traykovski, and W. R. Geyer (2005), Flood dispersal and deposition by near-bed gravitational sediment flows and oceanographic transport: A numerical modeling study of the Eel River shelf, northern California, *J. Geophys. Res.*, *110*, C09025, doi:10.1029/2004JC002727.

Hay, A. E. (2008), Near-bed turbulence and relict waveformed sand ripples: Observations from the inner shelf, *J. Geophys. Res.*, *113*, C04040, doi:10.1029/2006JC004013.

Higgins, E. E. (2002), *Effects of a Muddy Coast on Wave Attenuation: Gulf of Mexico, Louisiana*, 49 pp., Boston Coll., Chestnut Hill, Mass.

Hill, D. F., and M. A. Foda (1998), Subharmonic resonance of oblique interfacial waves by a progressive surface wave, *Proc. Math. Phys. Eng. Sci.*, *454*(1972), 1129–1144.

Hill, D. F., and M. A. Foda (1999), Effects of viscosity and elasticity on the nonlinear resonance of internal waves, *J. Geophys. Res.*, *104*(C5), 10,951–10,957, doi:10.1029/1998JC900114.

Hsu, T.-J., C. E. Ozdemir, and P. A. Traykovski (2009), High-resolution numerical modeling of wave-supported gravity-driven mudflows, *J. Geophys. Res.*, *114*, C05014, doi:10.1029/2008JC005006.

Hurther, D., and P. D. Thorne (2011), Suspension and near-bed load sediment transport processes above a migrating, sand-rippled bed under shoaling waves, *J. Geophys. Res.*, *116*, C07001, doi:10.1029/2010JC006774.

Jaffré, F. M., T. C. Austin, and G. Terray (2010), Miniature, low power, generic Doppler Sonar, in *OCEANS 2010*, pp. 1–4, IEEE, Seattle, Wash.

Jaramillo, S., A. Sheremet, M. A. Allison, A. H. Reed, and K. T. Holland (2009), Wave-mud interactions over the muddy Atchafalaya subaqueous clinoform, Louisiana, United States: Wave-supported sediment transport, *J. Geophys. Res.*, *114*, C04002, doi:10.1029/2008JC004821.

Jiang, F., and A. J. Mehta (1993), Some observations on fluid mud response to water waves, in *Dynamics and Exchanges in Estuaries and the Coastal Zone*, edited by D. Prandle, pp. 351–376, AGU, Washington, D. C., doi:10.1029/CE040p0351.

Jiang, F., and A. J. Mehta (1995), Mudbanks of the Southwest Coast of India IV: Mud viscoelastic properties, *J. Coastal Res.*, *11*(3), 918–926, doi:10.2307/4298392.

Kaihatu, J. M., A. Sheremet, and K. T. Holland (2007), A model for the propagation of nonlinear surface waves over viscous muds, *Coastal Eng.*, *54*(10), 752–764, doi:10.1016/j.coastaleng.2007.05.003.

Kajiura, K. (1968), A model of the bottom boundary layer in water waves, *Bull. Earthquake Res. Inst. Univ. Tokyo*, *46*, 75–123.

Kemp, G. P., and J. T. Wells (1987), Observations of shallow-water waves over a fluid mud bottom: implications to sediment transport, *Coastal Sediments (1987)*, edited by N. C. Kraus, pp. 363–378, ASCE, New Orleans, La.

Kineke, G. C., R. W. Sternberg, J. H. Trowbridge, and W. R. Geyer (1996), Fluid-mud processes on the Amazon continental shelf, *Cont. Shelf Res.*, *16*(5–6), 667–696, doi:10.1016/0278-4343(95)00050-X.

Kineke, G. C., E. E. Higgins, K. Hart, and D. Velasco (2006), Fine-sediment transport associated with cold-front passages on the shallow shelf, Gulf of Mexico, *Cont. Shelf Res.*, *26*(17–18), 2073–2091, doi:10.1016/j.csr.2006.07.023.

Kranenburg, W. (2008), Modelling wave damping by fluid mud: Derivation of a dispersion equation and an energy dissipation term and implementation into SWAN, Master thesis, 156 pp., TU Delft, Civ. Eng. and Geosci., Hydraul. Eng., Delft, Netherlands.

Kranenburg, W., J. Winterwerp, G. de Boer, J. Cornelisse, and M. Zijlema (2011), SWAN-Mud: Engineering model for mud-induced wave damping, *J. Hydraul. Eng.*, *137*(9), 959–975, doi:10.1061/(ASCE)HY.1943-7900.0000370.

Lee, T., J. Tsai, and D. Jeng (2002), Ocean waves propagating over a Columb-damped poro-elastic seabed of finite thickness, *Comput. Geotech.*, *29*, 119–149, doi:10.1016/S0266-352X(01)00024-6.

Li, J., X.-N. Wan, Q. He, M. Ying, L.-Q. Shi, and S. M. Hutchinson (2004), In-situ observation of fluid mud in the North Passage of Yangtze Estuary, China, *China Ocean Eng.*, *18*(1), 149–156.

Liu, P. (1973), Damping of water waves over porous bed, *ASCE J. Hydraul. Div.*, *92*(12), 2263–2271.

Macpherson, H. (1980), The attenuation of water waves over a non-rigid bed, *J. Fluid Mech.*, *97*, 721–742, doi:10.1017/S0022112080002777.

Madsen, O. S. (1994), Spectral wave-current bottom boundary layer flows, *Coastal Eng. Proc.*, *1*(24), 384–398, doi:10.1029/JC092iC13p14581.

Mathew, J., and M. Baba (1995), Mudbanks of the Southwest Coast of India. 2. Wave-Mud Interactions, *J. Coastal Res.*, *11*(1), 179–187.

Mei, C., and P. Liu (1987), A Bingham-plastic model for a muddy seabed under long waves, *J. Geophys. Res.*, *92*(C13), 14,581–14,594.

Ng, C.-O. (2000), Water waves over a muddy bed: a two-layer Stokes' boundary layer model, *Coastal Eng.*, *40*(3), 221–242, doi:10.1016/S0378-3839(00)00012-0.

Nielsen, P. (1981), Dynamics and geometry of wave-generated ripples, *J. Geophys. Res.*, *86*(C7), 6467–6472, doi:10.1029/JC086iC07p06467.

Nielsen, P. (1992), *Coastal Bottom Boundary Layers and Sediment Transport*, World Sci., Singapore.

Ozdemir, C. E., T.-J. Hsu, and S. Balachandar (2011), A numerical investigation of lutocline dynamics and saturation of fine sediment in the oscillatory boundary layer, *J. Geophys. Res.*, *116*, C09012, doi:10.1029/2011JC007185.

Rogers, W. E., and K. T. Holland (2009), A study of dissipation of wind-waves by mud at Cassino Beach, Brazil: Prediction and inversion, *Cont. Shelf Res.*, *29*(3), 676–690, doi:10.1016/j.csr.2008.09.013.

Ross, M. A., and A. J. Mehta (1989), On the mechanics of lutoclines and fluid mud, *J. Coastal Res.*, *5*, 51–62, doi:10.2307/25735365.

Safak, I., A. Sheremet, M. A. Allison, and T.-J. Hsu (2010), Bottom turbulence on the muddy Atchafalaya Shelf, Louisiana, USA, *J. Geophys. Res.*, *115*, C12019, doi:10.1029/2010JC006157.

Sahin, C., I. Safak, A. Sheremet, and A. J. Mehta (2012), Observations on cohesive bed reworking by waves: Atchafalaya Shelf, Louisiana, *J. Geophys. Res.*, *117*, C09025, doi:10.1029/2011JC007821.

Scully, M. E., C. T. Friedrichs, and L. D. Wright (2003), Numerical modeling of gravity-driven sediment transport and deposition on an energetic continental shelf: Eel River, northern California, *J. Geophys. Res.*, *108*(C4), 3120, doi:10.1029/2002JC001467.

Sheremet, A., and G. W. Stone (2003), Observations of nearshore wave dissipation over muddy sea beds, *J. Geophys. Res.*, *108*(C11), 3357, doi:10.1029/2003JC001885.

Sheremet, A., S. Jaramillo, S. F. Su, M. A. Allison, and K. T. Holland (2011), Wave-mud interaction over the muddy Atchafalaya subaqueous clinoform, Louisiana, United States: Wave processes, *J. Geophys. Res.*, *116*, C06005, doi:10.1029/2010JC006644.

Siadatmousavi, S. M., M. N. Allahdadi, Q. Chen, F. Jose, and H. H. Roberts (2012), Simulation of wave damping during a cold front over the muddy Atchafalaya shelf, *Cont. Shelf Res.*, *47*, 165–177, doi:10.1016/j.csr.2012.07.012.

Smyth, C., and A. E. Hay (2002), Wave friction factors in nearshore sands, *J. Phys. Oceanogr.*, *32*(12), 3490–3498.

Tennekes, H., and J. L. Lumley (1972), *A First Course in Turbulence*, MIT Press, Cambridge, Mass.

Traykovski, P. (2007), Observations of wave orbital scale ripples and a nonequilibrium time-dependent model, *J. Geophys. Res.*, *112*, C06026, doi:10.1029/2006JC003811.

Traykovski, P., W. R. Geyer, J. D. Irish, and J. F. Lynch (2000), The role of wave-induced density-driven fluid mud flows for cross-shelf transport on the Eel River continental shelf, *Cont. Shelf Res.*, *20*(16), 2113–2140, doi:10.1016/S0278-4343(00)00071-6.

Traykovski, P., P. L. Wiberg, and W. R. Geyer (2007), Observations and modeling of wave-supported sediment gravity flows on the Po prodelta and comparison to prior observations from the Eel shelf, *Cont. Shelf Res.*, *27*(3), 375–399.

Trowbridge, J. H., and S. Elgar (2001), Turbulence measurements in the surf zone, *J. Phys. Oceanogr.*, *31*(8), 2403–2417, doi:10.1175/1520-0485(2001)031<2403:TMITSZ>2.0.CO;2.

Trowbridge, J. H., and G. C. Kineke (1994), Structure and dynamics of fluid muds on the Amazon Continental Shelf, *J. Geophys. Res.*, *99*(C1), 865–874, doi:10.1029/93JC02860.

Tubman, M. W., and J. N. Suhayda (1976), Wave action and bottom movements in fine sediments, paper presented at Coastal Engineering Proceedings, ASCE, Honolulu, Hawaii.

USACE (2012), Stage & Discharge Data, Atchafalaya River at Simmesport, La. [Available at http://waterdata.usgs.gov/nwis/uv/?site_no=07381490.]

van der Werf, J. J., J. S. Doucette, T. O'Donoghue, and J. S. Ribberink (2007), Detailed measurements of velocities and suspended sand concentrations over full-scale ripples in regular oscillatory flow, *J. Geophys. Res.*, *112*, F02012, doi:10.1029/2006JF000614.

van Rijn, L. (2007), Unified view of sediment transport by currents and waves. I: Initiation of motion, bed roughness, and bed-load transport, *J. Hydraul. Eng.*, *133*(6), 649–667, doi:10.1061/(ASCE)0733-9429(2007)133:6(649).

Vinzon, S. B., and A. J. Mehta (2000), Boundary layer effects due to suspended sediment in the Amazon River estuary, in *Proceedings in Marine Science*, vol. 3, edited by H. M. William and J. M. Ashish, pp. 359–372, Elsevier, Amsterdam, doi:10.1016/S1568-2692(00)80131-X.

Wells, J. T. (1983), Dynamics of coastal fluid muds in low-, moderate, and high-tide-range environments, *Can. J. Fish. Aquat. Sci.*, *40*, suppl. 1, 130–142.

Wells, J. T., and G. P. Kemp (1986), Interaction of surface waves and cohesive sediments: field observations and geologic significance, in *Estuarine cohesive sediment dynamics*, edited by A. J. Mehta, pp. 43–65, Springer, N. Y.

Wiberg, P. L., and C. K. Harris (1994), Ripple geometry in wave-dominated environments, *J. Geophys. Res.*, *99*(C1), 775–789, doi:10.1029/93JC02726.

Winterwerp, J. C., R. F. D. Graaff, J. Groeneweg, and A. P. Luijendijk (2007), Modelling of wave damping at Guyana mud coast, *Coastal Eng.*, *54*(3), 249–261, doi:10.1016/j.coastaleng.2006.08.012.

Winterwerp, J. C., G. J. de Boer, G. Greeuw, and D. S. van Maren (2012), Mud-induced wave damping and wave-induced liquefaction, *Coastal Eng.*, *64*, 102–112, doi:10.1016/j.coastaleng.2012.01.005.

Wright, L. D., and C. T. Friedrichs (2006), Gravity-driven sediment transport on continental shelves: A status report, *Cont. Shelf Res.*, *26*(17–18), 2092–2107, doi:10.1016/j.csr.2006.07.008.

Wright, L. D., C. T. Friedrichs, S. C. Kim, and M. E. Scully (2001), Effects of ambient currents and waves on gravity-driven sediment transport on continental shelves, *Mar. Geol.*, *175*(1–4), 25–45, doi:10.1016/S0025-3227(01)00140-2.

Yang, R.-Y., and H. H. Hwung (2012), Combination mode of internal waves generated by surface wave propagating over two muddy sea beds, *Adv. Math. Phys.*, *0122*, 9, doi:10.1155/2012/183503.

Zedel, L. (2008), Modeling pulse-to-pulse coherent Doppler Sonar, *J. Atmos. Oceanic Technol.*, *25*(10), 1834–1844, doi:10.1175/2008JTECHO585.1.

Zedel, L., A. E. Hay, R. Cabrera, and A. Lohrmann (1996), Performance of a single-beam pulse-to-pulse coherent Doppler profiler, *IEEE J. Oceanic Eng.*, *21*(3), 290–297, doi:10.1109/48.508159.